Chemo-mechanical Simulation of the Influence of Dislocations in Lithium-ion Battery Materials

Zur Erlangung des Grades eines Doktors der Naturwissenschaften (Dr. rer. nat.)
Genehmigte Dissertation von Christoph Reimuth aus Seeheim-Jugenheim
Tag der Einreichung: 21.11.2022, Tag der Prüfung: 6.3.2023

1. Gutachten: Prof. Dr. Bai-Xiang Xu
2. Gutachten: Prof. Dr. Yuri Genenko
Darmstadt, Technische Universität Darmstadt

TECHNISCHE UNIVERSITÄT DARMSTADT

Materials and Earth Sciences Department
Fachgebiet
Mechanik funktionaler Materialien

Chemo-mechanical Simulation of the Influence of Dislocations in Lithium-ion Battery Materials

Accepted doctoral thesis by Christoph Reimuth

Date of submission: 21.11.2022
Date of thesis defense: 6.3.2023

Darmstadt, Technische Universität Darmstadt

Acknowledgements

I would like to express my deepest gratitude to Professor Dr. Bai-Xiang Xu for her valuable advice during the planning and development of this research work. This endeavor would not have been possible without my supervisors Dr. Peter Stein and Dr. Xiandong Zhou who generously provided knowledge and expertise.

I cannot begin to express my thanks to Professor Yuri Genenko, who agreed to take the role of the second reviewer despite the troubling times in Ukraine. My thoughts are with him and his family. I would like to extend my sincere thanks to the the remaining members of my defense committee Professor Dr. Ralf Müller and Professor Dr. Karsten Albe. I would also like to express my deep gratitude to the generous support from the German Research Foundation DFG, who financed my research and the Lichtenberg high-performance computer of TU Darmstadt who provided invaluable computation resources.

I would like to show my gratitude to Yangyiwei Yang for teaching the Moose way and Yang Bai for his support in the model developement and understanding chemo-mechanics. I would like to extend my sincere thanks to Dr. Yao Liu, Binbin Lin and Dr. Shahed Rezaei for their valuable feedback and fruitful discussions. Thanks should also go to Somnath Bharech and Nick Finger for their valuable technical support. I'd also like to extend my gratitude to Maren Arnold for all kinds of administrative support.

I had great pleasure of working in the group Mechanics of Functional materials with the members Dr. Wang Shuai, Dr. Ziqi Zhou, Dr. Yangbin Ma, Mamun Al Siraj, Wei Liu, Dr. Qihua Gong, Prof. Dr. Min Yi, Dr. Habib Pouriayevali, Sebastian Wissel, Patrick Kühn, Mozhdeh Fatidost, Hamid Nouri, Ruan Hui, Abdullah Shafqat, Dr. Dominik Ohmer, Armin Asheri and others.

I would like to express my deepest gratitude to Xiaowen, Marlis and Wolfgang for their encouragement, patience and moral support throughout the duration of this project. to

Abstract

Lithium-ion batteries (LIBs) represent the subject of rapidly growing research efforts due to their outstanding physical properties, such as high energy density, superior rate capability, and excellent cycling performance. These performance parameters of LIBs are governed by the ion diffusion process in the host electrode materials. The role of material heterogeneity and structural defects is one of the major research topics regarding the performance optimization of LIBs. In this work, a mechanically coupled diffusion model combined with finite element formulation is developed, where the dislocation is modeled by the regularized eigenstrain based on a non-singular continuum dislocation theory. The free energy density for the diffusion model was formulated as a function of the ion concentration, including the strain energy density. The ions were attributed with an eigenstrain representing the volume change upon ion intercalation. The model was applied to study the interaction between dislocations and diffusive ions. On the one hand, depending on the state of charge, the results show a redistribution of the ions respective to the dislocation stress field. On the other hand, the diffusing ions introduce a stress field, reducing the dislocation stress field. The simulation of potentiostatic and galvanostatic charging shows a substantial heterogeneity of ion concentration around the dislocation core but no overall alteration of the charging speed.

Furthermore, the mechanically coupled diffusion model is extended to a phase separation model. The configurational mechanics is generalized for dislocations in the mechanically coupled diffusion model to compute driving forces on misfit dislocations. The driving forces on a dislocation are due to the strain originating from the lattice misfit and from the dislocation interaction with free surfaces, which can be described with the model of an image dislocation. An energy-based criterion for the stability of misfit dislocations in two-phase electrode particles is formulated. This allows computing the energy required to introduce a misfit dislocation into a particle and analyze the results to find a critical particle size for stable dislocations. The results show that the critical particle size is the smallest when the dislocation and interface are positioned in the center. The critical

particle size also strongly depends on the dislocation core width implemented in the dislocation model.

Zusammenfassung

Das Interesse an Lithium Ionen Batterien wurde aufgrund ihrer herausragenden physikalischen Eigenschaften, wie hohe Energiedichte, ausgezeichnete Lade und Entladegeschwindigkeit und ihrer exzellenten Leistungserhalt über die Lade-Entlade-Zyklen. Die Grundlage dieser Eigenschaften bildet der Diffusionsprozess der Ionen in den Elektrodenmaterialien. Ein besonderer Fokus im Hinblick auf die Leistungsoptimierung von Lithium Ionen Batterien liegt in der Untersuchung von Material Heterogenität und Strukturdefekten. In der vorliegenden Arbeit wird ein mechanisch gekoppeltes Diffusionsmodell mit Finite Elemente Formulierung entwickelt, in der Versetzungen als regularisierte Eigendehnung auf der Grundlage einer nicht-singulären Kontinuumsversetzungstheorie modelliert werden. Die freie Energiedichte für das Diffusionmodell wurde als Funktion der Ionenkonzentration aufgestellt, wobei wie spezifische Verzerrungsenergie enthalten ist. Die Ionenkonzentration ist mit einer Eigendehnung verknüpft, die die Volumenänderung durch die Einlagerung von Ionen in das Kathodenmaterial repräsentiert. Das Modell wurde zur Untersuchung der Interaktion von Stufenversetzungen und diffundierenden Ionen eingesetzt. Als Ergebnisse wurde dem Spannungsfeld der Versetzung folgend eine Umverteilung der Ionen um den Versetzungskern beobachtet, die vom Ladezustand abhängt. Auf der anderen Seite verursachen die Ionen selbst ein Spannungsfeld, dass durch die Umverteilung das Spannungsfeld der Versetzung reduziert. Die Simulation von potentiostatischer und galvanostatischer Ladevorgängen zeigte eine substantielle Heterogenität der Ionenkonzentration um den Versetzungskern aber keine generelle Änderung der Ladegeschwindigkeit.

Darüber hinaus wurde das mechanisch gekoppelte Diffusionsmodell zu einen Phasenseparationsmodell erweitert. Die Konfigurationsmechanik wurde für Versetzungen in mechanisch gekoppelten Diffusionsmodellen generalisiert um treibende Kräfte auf Versetzungen durch die Differenz der Gitterparameter an Grenzflächen zu berechnen. Die Ursache der treibenden Kräfte auf die Versetzung sind die Dehnung durch die Gitterfehlanpassung und die Interaktion der Versetzung mit freien Oberflächen, die mit dem Modell einer Spiegelversetzung beschrieben werden kann. Ein energiebasiertes Kriterium für die Stabilität von Grenzflächenversetzungen in zweiphasigen Elektrodenpartikeln wurde

aufgestellt. Damit kann die erforderliche Energie berechnet werden, um eine Grenzflächenversetzungen in ein Partikel einzubringen und auf eine kritische Partikelgröße für stabile Grenzflächenversetzungen zu untersuchen. Die Ergebnisse zeigten eine kleinste kritische Partikelgröße wenn die Versetzung mit der Grenzfläche genau in der Mitte des Partikels positioniert sind. Die kritische Partikelgröße hängt auch stark von der im Versetzungsmodell implementierten Kernweite der Versetzung ab.

Contents

List of Figures

List of Tables

Abbreviations

Abbreviation	Full name
DIS	Diffusion induced stress
FEM	Finite element method
FP	$FePO_4$
GGA	Generalized gradient approximation
IP	Integration point
LIBs	Lithium ion batteries
LFP	$LiFePO_4$
MOOSE	Multiphysics Object-Oriented Simulation Environment
NMC	$LiNi_{1-x-y}Mn_xCo_yO_2$
PDE	Partial differential equation
SEI	Secondary electrolyte interface
SOC	State of charge

Conventions

Mathematical formulations follow the conventions introduced here. Index notation is used, where lowercase indices range from 1 to 3 and the Einstein summation convention is used when indices appear in pairs in a term. Alternatively tensors are written in bold letters, for example $\mathbf{C}$. Partial derivatives with respect to spatial coordinates x_i are written as $(\square)_{,i}$ and time derivatives are written as $\dot{\square}$. Symbols marked with the $\widetilde{\square}$ have the corresponding physical units while plain symbols are dimensionless. The Kronecker delta is defined as

$$\delta_{ij} = \begin{cases} 1 & \text{for } i = j, \\ 0 & \text{for } i \neq j. \end{cases}$$

The permutation tensor is defined as

$$\epsilon_{ijk} = \begin{cases} 1 & \text{for even permutation of } i,\ j,\ k, \\ -1 & \text{for uneven permutation of } i,\ j,\ k, \\ 0 & \text{for other cases.} \end{cases}$$

1 Introduction

Lithium-Ion Batteries

Nowadays, technology and humanity are growing new levels of interconnection, where mobility and the independence of stationary power supplies become more and more critical. Modern technology takes advantage of and is dependent on the energy availability at any time in sufficient amounts. Example applications are mobile phones and computers and, in the mobility sector, electric rollers, electric supported bikes electric cars. For those applications, the primary challenge for energy storage systems is to supply enough energy at a high enough rate while using as little space and weight as possible. In this area, lithium-ion batteries (LIBs) became unmatched for their high energy density, superior rate capability, excellent cycling performance, and not to the least for the simplicity of recharging at the omnipresent public electric network. In a lithium-ion battery, energy can be stored and released by moving lithium ions between a high-potential material and a low-potential material. When the ions are concentrated in the negative electrode (anode), the state is considered as charged. When the ions are concentrated in the positive electrode (cathode), the state is discharged. When transferring the ions between the states, an electric current will be released or has to be applied over a metal contact connecting the electrodes. Ion exchange between the electrodes happens via an electrolyte, which needs to be electrically insulating but allows for diffusion of ions to ensure the above described working principle.

The critical properties of a battery, the capacity for energy storage and the time required during charging and discharging, are sensitive to defects in the battery material emerging during continuous usage of the battery and have a negative effect on the properties. The preservation of the battery performance under continuous use is called cyclability and is described as the preservation of the capacity over the number of cycles between the charged and discharged state. Various mechanisms causing battery degradation and performance are described in [135]. Intercalation or deintercalation often is accompanied

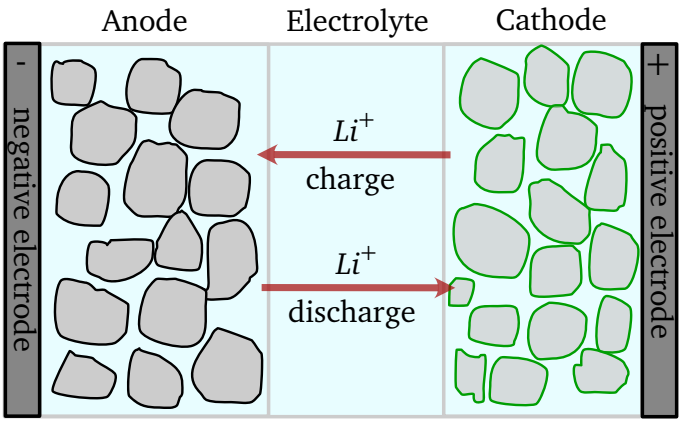

Figure 1.1: Principle of a lithium-ion battery.

by large deformation and significant stress development. Consequential crack formation can lead to a higher ion resistance and can even separate material from the electrolyte reducing the capacity. Chemical reaction of the electrode materials with the electrolyte can lead to formation of the secondary electrolyte interface (SEI). It is assumed that the SEI causes surface passivation. However, due to the lattice mismatch to the electrode material, cracks can expose the electrode during cycling and cause a capacity loss over the battery lifetime. Careful design of the battery cell is necessary to cope with these challenges.

By far, the mostly utilized anode material is graphite. Alternative anode materials such as Si and Sn have a higher capacity but are not stable due to large volume changes [9]. The most widely spread cathode materials are $LiCoO_2$, $LiMn_2O_4$, $LiFePO_4$, and $LiNi_{1-x-y}Mn_xCo_yO_2$ (NMC), which have large differences in performance and prices. The biggest part of the cost of a battery is the cathode material, which is related to rare and expensive elements such as cobalt [72]. NMC is an example of how the chemical composition can change the properties of the cathode material while scaling down the cost [72]. Replacing cobalt with nickel increases the energy output, but on the downside, Li/Ni mixing increases instability. The mixing can be suppressed by donating manganese or aluminum and thus increasing the stability. Another factor in tuning the battery properties is the particle shape, as surface stresses of ellipsoidal particles increase (dis)charge rates but decrease the capacity compared to spherical particles [111]. Further surface stresses can stabilize smaller particles but reduce the usable capacity [112]. The deformation of the particles causes

damage at the grain boundaries, which can result in cracks and surface delamination [7, 115]. Li/cation antisite defects are common, especially in layered lithium metal oxides containing Ni [56, 86]. Such defects can improve the Li diffusion anisotropy in layered materials and ease the phase transition between the Li-rich and Li-poor phases [46]. Impurity atoms can have different effects. It could be shown that Fe impurities in NMC electrodes can increase capacity and capacity retention [98].

Dislocations in Lithium-Ion Batteries

Dislocations are common defects observed in LIBs [130, 120, 92, 114, 70, 110, 132]. Specifically, dislocation nucleation was observed during the lithiation of SnO_2 nanowires [93]. Dislocation clouds were observed during the phase transformation process from ordered to amorphous state at the diffusion front upon lithiation [50, 137, 19, 80]. An active role of dislocations in diffusion processes can be assumed, as nucleation of a Li-rich phase near a dislocation was observed in $LiNi_{0.5}Mn_{1.5}O_4$ [120]. Solute segregation has been widely observed for non-battery materials, such as nickel-based superalloys [57, 73]. Misfit dislocations observed in Li_2MnO_3 between the Li-rich and Li-poor phases can support the delithiation process by dislocation climb [92]. Furthermore, dislocations can influence the distribution of different phases [97, 44], enable alternative pathways for the diffusion [66], increase plastic deformability by massive dislocation nucleation [127], and increase the diffusion along the dislocation core, often referred as "pipe diffusion" [118, 30, 65]. Considering the large stressfields introduced locally by dislocations and their fundamental role in the development of cracks, it seems to be necessary to understand how dislocations influence mechanisms in LIBs. Material heterogeneity can influence the ion diffusion process [31], which can be related to dislocations [130]. Material heterogeneity can cause a concentration heterogeneity resulting in an insufficient utilization of active material, internal stresses, local overcharge/ over-discharge, and thus degradation of the battery performance[130]. Heterogeneous particle activity due to heterogeneous properties was identified as the predecessor of heterogeneous particle damage in the early cycles of LIBs, with consecutive damage homogenization in later cycles [69]. What's more, the interaction between the self-stress of the dislocation and the diffusion-induced stress (DIS) should also be considered. In Li- and Mn-rich cathode materials the tensile strain during delithiation at high voltages causes oxygen release and transition metal migration, and the material degeneration strain affects the structural stability [74]. However, dislocations are a promising candidate for "defect engineering", where defects are manipulated to design material properties specifically [45].

The demand to understand and describe the properties of dislocations fuels an ongoing debate in the literature. Classical analytical solutions for the dislocation derived from an eigenstrain along the gliding plane have been known for a long time. However, the description of the core is not physical due to its singularity [91, 13]. This motivated advanced dislocation models eliminating the singularity [63, 12]. Chemo-mechanically coupled models already try to grasp the influence of dislocations on the DIS utilizing a concentration dependent dislocation density. The influence of dislocations on diffusion-induced stress is studied in a few models based on a concentration dependent dislocation density [128, 68, 14, 141]. Those models associate the dislocation density with shear stress that directly contributes to the DIS, utilizing the Taylor hardening model [28]. It was shown that tensile stresses are reduced by the dislocation or even converted to compressive stresses, thereby reducing the tendency of crack nucleation and propagation. However, as the dislocation density is implemented as a homogeneous field variable, heterogeneous contributions of individual dislocations, including local enrichment or depletion of solute distribution, could not be described by these models. The interaction of phase transformations and dislocations in metals was investigated within an atomistic study in [85], and a phase field model was proposed in [67]. Discrete dislocation models have been developed for solute hardening in metals [17, 40, 48, 87], but theoretical and numerical models for analyzing dislocations in LIBs are still needed. Chemo-mechanical finite element models describing diffusion in LIBs are developed in [112, 113, 136, 6], where the incorporation of the coupling between the stress field and the concentration can influence the ion mobility [112, 113]. Considering the hydrostatic stress contribution of dislocations to the free energy density of diffusive ions, an influence on the mobility around dislocations is expected, but to the best of the author's knowledge not thoroughly studied in the literature.

Modeling the interaction of dislocations with other dislocations and defects is a computational challenge due to the extended range of the dislocation stress field. An established method to capture the driving forces on dislocations and their interaction is the calculation with the Peach-Koehler equation [99], which is utilized in discrete dislocation dynamics [123, 121, 32, 52]. In the above examples, the Peach-Koehler force includes purely mechanical contributions, so that interactions based on chemistry or electrostatics are not covered. However, the driving force on the dislocation can be based on the dislocation density tensor to derive the Eshelby stress tensor [61], which was extended to dislocations in piezoelectric materials [2]. The concept of configurational or material forces, which has its origin in the early work done by Eshelby [25], is an effective tool to evaluate driving forces on defects in materials, where the Eshelby stress tensor is formulated as the variation of the system potential with respect to the position of the defect. The

divergence of the Eshelby stress tensor can then be read as configurational forces [24]. By linear extension of the free energy functional, the theory can be easily extended to cover multi-physic problems. On this basis, Müller and Gross developed a scheme for the finite element method to compute configurational forces on defects such as point defects, inclusions, phase boundaries, and cracks [90, 34]. The configurational force theory was refined to include interaction between domain walls and point defects in ferroelectric materials [89], coupled electro-elastic problems [131, 143], and defects in problems involving complex external loads and boundary conditions [8]. Driving forces on dislocations within the configurational mechanics were described in [3]. A numerical model to compute configurational forces on dislocations in a non-singular continuum dislocation model was developed in [139] and applied with an extension to cover the interaction between domain walls and dislocations in ferroelectric materials [45, 138]. In this work, the configurational force theory is adopted to analyze misfit dislocations in phase separation electrode materials within a mechanical coupled Cahn-Hilliard phase transformation model.

In a range of intercalation cathode materials such as $LiNi_{0.5}Mn_{1.5}O_4$ [75], LiV_2O_5 [136, 20], and $LiFePO_4$ (LFP) [51], the formation of co-existing phases can be observed during the charging and discharging process. The phase transformation between those phases is often accompanied by a volume change, and will result in a lattice mismatch and misfit strain at the phase boundary. These properties are heavily size-dependent. Competing mechanical and chemical mechanisms in monodispersed LFP particles with a size around $10\,\mathrm{nm}$ raise size dependent-properties where a complete single-phase reaction without any plateau voltage is developed, and the cracking behavior of the particles is influenced [51]. Especially for small particles, the lattice mismatch between the LFP phase and $FePO_4$ (FP) phase close to the surface is relaxed to attenuate elastic effects and stimulate phase separation. However, phase separation takes place with a preferred wavelength that requires a larger particle size. A critical particle size can be found for a range of materials. In platelike and equiaxed LFP particles the crack formation related to the misfit strain is suppressed below a critical size [49]. Crack formation during the first lithiation of Si nanoparticles can only occur in particles larger than $150\,\mathrm{nm}$ [76]. In metals, an increase of the dislocation density with a decreased particle size was found for grains above $10\,\mu\mathrm{m}$, where a relation to an increased grain boundary length as a dislocation source is assumed [53]. An underlying reason for crack development can be the formation of misfit dislocations at the phase boundary. Misfit dislocations are an example of a multiphysics scenario. On the one hand, the misfit strain interacts with the dislocation stress field. On the other hand, the stress field can influence the chemical composition at the interface. Misfit dislocations can reduce interface mobility, cause irreversible

degradation of the electrochemical performance and cause fatigue crack formation [83, 94]. Consequently, the prevention of misfit dislocations in electrode particles can increase the performance of LIBs. In LFP particles, misfit dislocations have been observed by transmission electron microscopy [142]. Misfit dislocations are well-studied in epitaxial films on substrates [13]. The formation of those misfit dislocations can be related to an energy-based stability criterion for the formation which states the elastic strain energy reduction of the strained film due to the misfit dislocation must be equal or larger than the dislocation self energy. The model proposed by Esmizadeh and Haftbaradaran [26, 27] adopts this idea for two-phase particles. Here the condition for the critical particle size is that the work of the misfit strain-induced stress field (background stress field) during the formation of misfit dislocations is equal to the self-energy of misfit dislocations. The Peach-Koehler formula [99] was utilized to calculate the driving forces on the misfit dislocation due to both the background stress field and the image stress field that arises from the free surfaces of the particle. Esmizadeh and Haftbaradaran's work regards the work done on the dislocation by the image stress resulting from the dislocation self stress and the misfit stress due to the phase boundary, but neglects the coupling between the misfit stress and the dislocation self stress that results in ion redistribution and in the change of the DIS. The extension to the chemically coupled cases considering dilute diffusion and phase transformation is still open. The existence of misfit dislocations can significantly change the concentration distribution near the phase boundary, which leads to the change of the stress field in the phase boundary. Such a chemo-mechanical calculation of the driving force on the misfit dislocation is crucial for predicting the critical size of dislocation-containing particles and goes beyond pure elastic models.

Goal and Outline

A numerical model is a powerful theoretical framework to shed light on the role of the dislocation in battery materials and deal with the complex geometry of electrodes, complex boundary conditions, or inhomogeneous and anisotropic materials. The dislocation model is developed specifically to study the impact of dislocations on the diffusion and mobility of lithium ions and the resulting driving forces on the dislocation. By computing the work required to move a dislocation into a particle allows an estimation of a particle size dependent stability for dislocations. For that, a non-singular chemo-mechanical continuum dislocation model and respective configurational mechanics are introduced. A schematic outline of the coupled model and the physics applied in the results chapters in this work is depicted in figure 1.2.

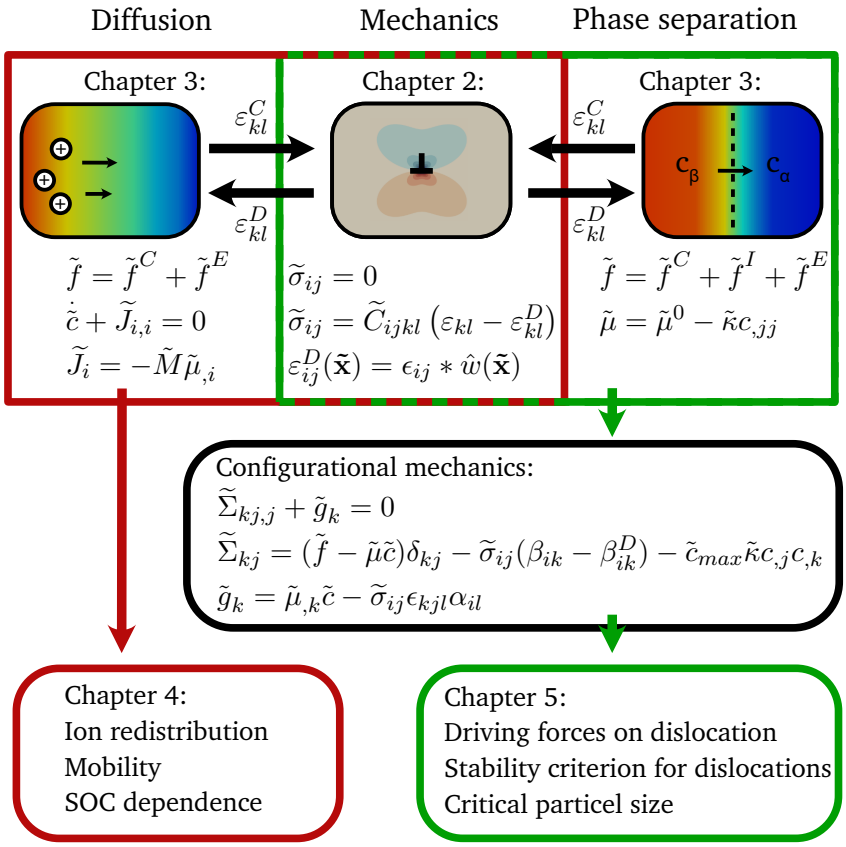

Figure 1.2: Schematic introduction of the model in this work.

First, a linear elastic continuum model for small strains is formulated to cover the mechanical part. The model is extended to include dislocations by introducing an eigenstrain on the gliding plane describing the dislocation self-distortion. To remove the singularity of the classic solutions based on the delta function, the dislocation eigenstrain is described by a non-singular dislocation theory so that the singularity is removed. Driving forces on the dislocation are computed in a postprocessing step within the theory of configurational forces. For that, the Eshelby stress tensor is derived from the gradient of the free energy density.

Further, a phase field model for the mechanically coupled diffusion is derived extending the linear elastic continuum model for dislocations. The free energy density is formulated in terms of the chemical and mixing energy density, the interface energy density and the strain energy density. The original 4th order differential equation of the chemical model is split into two equations to reduce the integration order. By that the chemical potential and the concentration are introduced as separate but dependent degrees of freedom. Driving forces on the dislocation are computed in a postprocessing step within the theory of configurational forces. For that, the Eshelby stress tensor is derived from the gradient of the free energy density with contributions from both mechanics and diffusion.

The model is numerically implemented with the finite element method and applied to simulate the influence of dislocation in the cathode material $LiMn_2O_4$ on diffusion and state-of-charge (SOC) heterogeneity in LIBs. By this, the influence of the dislocation on ion redistribution and mobility is analyzed. Further, the influence of the dislocation on the phase distributions in two-phase materials is studied. Then the diffusion along a dislocation core is analyzed by combining the chemo-mechanical model with a pipe diffusion model. The configurational force theory is utilized to formulate an energy-based criterion for stable dislocations in stable LFP two-phase particles. For that, the work done on the dislocation by the image forces from the free surfaces and the misfit strain is integrated along the path for the dislocation gliding outside the particle. A negative change in the system energy is then an indicator for stable dislocations. This stability criterion is then utilized to evaluate a critical particle size for stable misfit dislocations square shaped $LiPO_4$ particles. The study is supplemented by analyzing the effect of the core parameter and the non-homogeneous phase-dependent elasticity of the LFP material. Finally, the critical particle sizes for particles of different shape and for particles with different positions of the interface is evaluated.

The remaining work is organized as described in the following. In chapter 2, the non-singular continuum dislocation model is introduced. First, the continuum mechanics for

small deformation is summarized. Then continuum discrete dislocation models are described, in particular the classical singular dislocation theory and non-singular dislocation theory. The mechanical section is completed with a description of driving forces on dislocations in the form of the Peach-Koehler equation and configurational force mechanics for dislocations. The non-singular dislocation theory is then formulated within small strain continuum mechanics. In particular, a Burgers vector convolution is integrated along the dislocation gliding plane and results in a dislocation eigenstrain. The model is implemented into the finite element method (FEM) by reformulation of the partial differential equations into the weak form, elementwise discretization, formulation of the stiffness matrix, and normalization to a dimensionless scale. Then the definition of the material properties follows. The implementation is concluded by an excursion on the integration order of the dislocation eigenstrain, which can be an easy source of error and cause spurious stresses. The model is benchmarked by comparison of the numerical solutions of the stress field of edge and screw dislocations to the analytic solutions. The influence of the mesh resolution and the dislocation core radius is demonstrated. The evaluation of the driving forces is benchmarked by comparing the configurational force on a dislocation in a sheared volume and close to a traction-free interface (concept of an image dislocation) to the Peach-Koehler force.

In chapter 3, the chemo-mechanical non-singular dislocation continuum model is formulated and implemented into the FEM. First, the theory of diffusion is summarized by defining Fick's laws and the Cahn-Hilliard phase field model. Second, the numerical dislocation model is extended to a chemo-mechanical model where the strain energy density contributes to the free energy functional. Finally, the model is implemented into FEM by reformulation of the partial differential equations into the weak form, elementwise discretization, formulation of the stiffness matrix, and normalization to a dimensionless scale. The chemo-mechanical model is benchmarked by comparative analysis of the numerically computed phase separation for a non-coupled model and fully mechanical coupled model and comparing the respective interphase thicknesses to the theoretical interface thickness. Further, the concentration field in the vicinity of an edge dislocation is compared to the respective analytical solutions in the equilibrium state. The benchmarks are concluded with an extension of the evaluation of the driving forces on a dislocation close to a traction free interface for the chemo-mechanical model.

In chapter 4, the heterogeneity induced by a dislocation in $LiMn_2O_4$ is analyzed, including the influence of the ion redistribution and diffusion-induced stress depending on the state of charge. Then the dislocation-induced mobility heterogeneity with the dependence on the state of charge is analyzed. The chapter is concluded with an excursion to the ion

diffusion along the dislocation core for a combined mechanical coupled diffusion and pipe diffusion model.

In chapter 5, the configurational mechanics of dislocations in phase transformation materials is utilized to study the size dependency of the formation of misfit dislocations. The phase separation is analyzed for particles with and without a dislocation considering the relaxation of the misfit strain due to ion redistribution and the interaction with the dislocation. On this basis, an energy-based criterion for the critical particle size for the formation of misfit dislocations is formulated and utilized to predict the critical particle size for square-shaped particles. Subsequently, the influence of the orthotropic and non-homogeneous phase-dependent elasticity and the core parameter on the predicted critical particle size is discussed, and the influence of different particle shapes and positions of the interface on the predicted critical particle size is analyzed. The chapter is concluded with a discussion of the model parameters.

In chapter 6 the results and discussions within this thesis are summarized and an outlook on future continuation of this work is given.

2 Finite Element Implementation of the Non-Singular Dislocation Model

In this chapter the non-singular continuum mechanics dislocation model is presented. In the first part the basics of linear elastic continuum mechanics are introduced. In the second part the fundamentals of dislocations are described with a focus on the analytical solutions of the elastic fields of dislocations. Here it is distinguished between the singular solutions, where the displacement caused by the dislocation is represented by the delta function, which introduces a singularity at the position of the dislocation core, and the non-singular solutions, that avoid this issue. Then the driving forces on dislocations are presented featuring the Peach-Koehler forces and configurational mechanics and their relation. On the basis of the continuum mechanics the numerical model for non-singular dislocations in linear elasticity is formulated. The dislocation model is derived based on the dislocation slip mathematically described by the delta function and consecutively developed into the non-singular dislocation theory following Cai et al. [12]. Then the implementation into FEM is described where the residuals and the Jacobian matrix are derived and normalized to natural units. The model is completed by defining the material properties. Benchmarks are done where the stress field of dislocations and the concentration field in the vicinity of an edge dislocation are compared to the respective analytical solutions. The configurational force on an edge dislocation is compared to the Peach-Koehler force for the examples of a sheared volume and a dislocation close to a free surface.

The non-singular continuum dislocation model and the derivation of the Eshelby tensor for the formulation of the configuration mechanics of dislocations has been published as part of the previous works [139, 138, 103, 140].

2.1 Continuum Mechanics

The linear elastic continuum mechanics describes the deformation of solids as a response to forces and constraints, see e.g. [35, 71]. According to [35], a body of volume V is in equilibrium, when the resulting forces from the body forces $\tilde{q}_i$ and the traction forces $\tilde{t}_i$ on the surface A vanish

$$\int_{\partial V} \tilde{t}_i dA + \int_V \tilde{q}_i dV = 0, \tag{2.1}$$

where the traction on the surface with normal vector n_j is $\tilde{t}_i = \widetilde{\sigma}_{ij} n_j$. This is equivalent to the equilibrium condition

$$\widetilde{\sigma}_{ij,j} + \tilde{q}_i = 0, \tag{2.2}$$

where the stress state in a body is described by the stress tensor $\widetilde{\sigma}_{ij}$. In this work the body forces are neglected towards a simplified equilibrium condition

$$\widetilde{\sigma}_{ij,j} = 0. \tag{2.3}$$

The displacement vector $\tilde{u}_i$ is defined as

$$\tilde{u}_i = \tilde{x}_i - \widetilde{X}_i, \tag{2.4}$$

with the spacial coordinates $\tilde{x}_i$ and the material coordinates $\tilde{X}_i$. Within this work the assumptions for linear elasticity and small strain hold, which means that the relation between $\tilde{x}_i$ and $\tilde{X}_i$ is linear and that the derivatives with respect to $\widetilde{X}_j$ can be replaced by derivatives with respect to $\tilde{x}_j$ as $\partial \tilde{u}_i / \partial \widetilde{X}_j \rightarrow \partial \tilde{u}_i / \partial \tilde{x}_j = \tilde{u}_{i,j}$. Then the infinitesimal strain tensor can be obtained as

$$\varepsilon_{kl} = \frac{1}{2} \left(\tilde{u}_{k,l} + \tilde{u}_{l,k} \right). \tag{2.5}$$

The total strain ε_{kl} is the sum of the elastic strain ε_{ij}^E and the inelastic contribution. In particular the strain caused by intercalation of ions ε_{kl}^C and due to dislocations ε_{kl}^D are considered in this work. Consequently the elastic strain reads as

$$\varepsilon_{kl}^E = \varepsilon_{kl} - \varepsilon_{kl}^C - \varepsilon_{kl}^D. \tag{2.6}$$

The lattice strain due to the presence of diffusive ions and the dislocation is discussed in detail in chapter 3. Hooke's law relates the elastic strain to the stress $\widetilde{\sigma}_{ij}$ in the constitutive equation

$$\widetilde{\sigma}_{ij} = \widetilde{C}_{ijkl} \varepsilon_{kl}^E = \widetilde{C}_{ijkl} (\varepsilon_{kl} - \varepsilon_{kl}^C - \varepsilon_{kl}^D), \tag{2.7}$$

with the fourth order elasticity tensor $\widetilde{C}_{ijkl}$. Hydrostatic stresses are defined as the mean of the normal stresses $\widetilde{\sigma}_h = (\widetilde{\sigma}_{11} + \widetilde{\sigma}_{22} + \widetilde{\sigma}_{33})/3$. The kinematic rates are on a much larger timescale than diffusion of ions in the solid, which allows the assumption that the mechanical state is always in equilibrium [39]. The energy stored in an elastic deformed unit volume can be found by integration of the forces required to induce this volume change, thus the elastic strain energy density is

$$\widetilde{\mathcal{F}}^E = \frac{1}{2} \int_{\widetilde{V}} \widetilde{\sigma}_{ij} \varepsilon_{ij}^E \mathrm{d}\widetilde{V}. \tag{2.8}$$

By solving the integral the strain energy density is found as $\tilde{f}^E = \frac{1}{2} \widetilde{\sigma}_{ij} \varepsilon_{ij}^E$. Complementary the stress tensor is describes as the derivative of the strain energy density with respect to the strain

$$\widetilde{\sigma}_{ij} = \frac{\partial \tilde{f}^E}{\partial \varepsilon_{ij}^E}. \tag{2.9}$$

2.2 Fundamentals of Dislocations

The theory for dislocation mechanics is covered in many textbooks such as the references for this chapter [13, 91]. Dislocations are a disturbance in the periodic crystal lattice caused by a partial displacement of atoms relative to the original lattice by the so called Burgers vector $\tilde{\mathbf{b}}$ relative to the original lattice. There are three types of dislocations, the edge dislocation, the screw dislocation and the mixed dislocation, which is a combined edge and screw dislocation. A dislocation is described by the sense vector ξ parallel to the dislocation core and the Burgers vector.

The edge dislocation has the form of an additional half plane pressed into the crystal lattice, where the edge of the half plane is the dislocation core. The Burgers vector is perpendicular to the sense vector $\tilde{\mathbf{b}} \perp \xi$. The gliding plane is defined for the edge dislocation by the normal vector $\mathbf{n} = \xi \times \tilde{\mathbf{b}}/(|\xi \times \tilde{\mathbf{b}}|)$. In the case of the screw dislocation lattice planes are distorted in a spiral around the dislocation core. The Burgers vector is perpendicular to the sense vector $\tilde{\mathbf{b}} \parallel \xi$. A pure screw dislocation has no defined gliding plane but a gliding plane can be defined for a mixed dislocation with an edge component. A dislocation can split up into partial dislocations with the partial Burgers vectors $\tilde{\mathbf{b}}_a$ and $\tilde{\mathbf{b}}_b$, where $\tilde{\mathbf{b}}_a + \tilde{\mathbf{b}}_b = \tilde{\mathbf{b}}$. Then the atoms between the dislocations are displaced by the partial Burgers vector $\tilde{\mathbf{b}}_a$ creating a stacking fault. Partial dislocations occur when the energy creating a single dislocation with Burgers vector $\tilde{\mathbf{b}}$ is larger than that of creating the

two partial dislocations and the stacking fault. In a crystal, active gliding planes are within the atomic planes with the highest density. Slip directions are along the shortest lattice translation vectors within the gliding plane. As an example, an fcc lattice is discussed for its slip systems and directions. In the fcc lattice, the slip planes are in the (111) planes with three independent slip directions along the [110] directions. The slip system then contains 12 slip directions in 4 gliding planes. A Burgers vector of this slip system is $\tilde{b} = \tilde{a}/2[110]$. The glide planes form a triangular lattice and are comparable to the hcp structure. The hcp structure is conveniently described using the Miller-Bravais notation with 3 basis vectors in the basal plane a_1, a_2, a_3 and a perpendicular vector a_4. The vectors in the basal plane are triangular orientated such that $a_1 + a_2 + a_3 = 0$. A vector is defined as $R_{hkil} = ha_1 + ka_2 + ia_3 + la_4 = [hkil]$. With the convention $h + k + i = 0$ each vector can be described uniquely. The primary slip system is within the basal plane (0001) with slip directions of type $1/3[11\bar{2}0]$. For deformation that cannot be covered by slip within the basal plane, secondary slip systems can be activated in glide planes of type $(11\bar{2}2)$ in directions $1/3[11\bar{2}3]$.

2.2.1 Singular dislocation models

Various dislocation models are described in the literature. Of those two singular models following Volterra and Mura are selected and schematically depicted in figure 2.1 with a comparison to a non-singular dislocation model. The Voltera model is a classic model for dislocations. First a tube around the dislocation line (dislocation core) is cut out of the volume. Then the volume is cut in a half plane along the dislocation gliding plane and displaced by the Burgers vector b. The Mura model defines a shear on the dislocation gliding plane in the form of a delta function, which is the dislocation eigenstrain [91]. Both models lead to identical solutions for the displacement and stress fields, and contain a singularity at the dislocation core. The delta function is replaced by a distribution function following Cai et al. [12]. This removes the singularity in the dislocation core while keeping the mathematics simple. In the following, the singular dislocation model following Volterra is introduced and the elastic fields are described. For that a three dimensional depiction of a straight edge and a straight screw dislocation is depicted in figure2.2

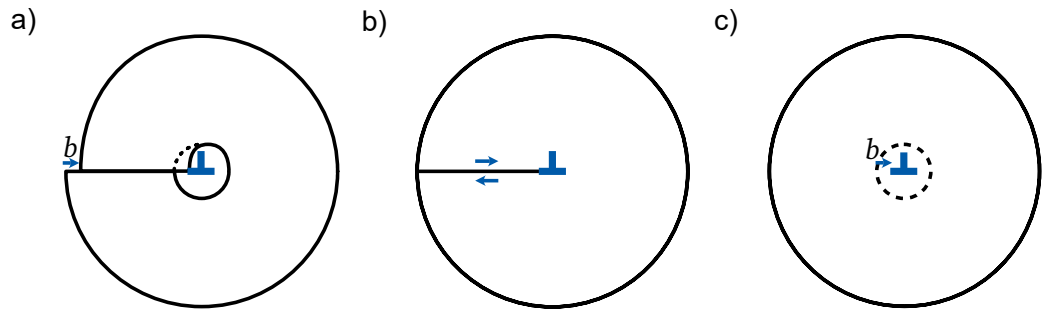

Figure 2.1: Schematic depictions for models of an edge dislocation in a cylinder. a) Volterra model [13]. b) Singular dislocation model with a defined eigenstrain on the gliding plane (Mura model) [91]. c) Non-singular dislocation model with distributed dislocation core from Cai et al. [12].

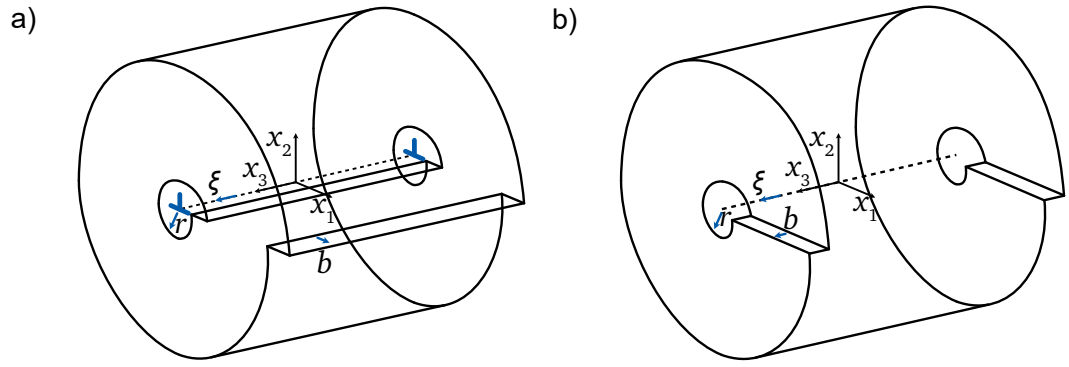

Figure 2.2: Volterra model for a) an edge dislocaton and b) a screw dislocation in a cylinder along the x_3 axis. A radius r is defined for the dislocation core.

Screw dislocation in an infinitely long cylinder

The analytical solution for the stress fields of a screw dislocation in an infinitely long cylinder with infinite radius R is shown following [13]. The solutions follow the Volterra model with a singularity within the dislocation core. The dislocation line and its Burgers vector are in positive x_2 direction, as indicated in figure 2.2b. The screw dislocation is characterized by a displacement which is only in the x_3 direction with no displacement in the perpendicular x_1 and x_2 directions. The screw dislocation can be described as an anti-plane strain problem in 2 dimensions. The displacement field of the screw dislocation has to satisfy both Laplace's equation

$$\nabla^2 \tilde{u}_3 = \left(\frac{\partial^2}{\partial \tilde{x}_1^2} + \frac{\partial^2}{\partial \tilde{x}_2^2} \right) \tilde{u}_3(\tilde{x}_1, \tilde{x}_2) = 0, \tag{2.10}$$

and the Burgers condition

$$\oint_{\widetilde{\mathbf{C}}} = \left(\frac{\partial \tilde{u}_i}{\partial \tilde{s}} \right) d\tilde{s} = \tilde{b}_i, \tag{2.11}$$

where the integral is counterclockwise along the closed loop $\widetilde{\mathbf{C}}$ around the dislocation line in the x_3-axis. The solution is the displacement field

$$\tilde{u}_3 = \frac{\tilde{b}}{2\pi}\theta = \frac{\tilde{b}}{2\pi} \arctan\left(\frac{\tilde{x}_2}{\tilde{x}_1} \right). \tag{2.12}$$

and consecutively the non-zero components of the stress field

$$\begin{aligned} \widetilde{\sigma}_{13} &= \widetilde{G}\widetilde{\gamma}_{13} = -\frac{\widetilde{G}\tilde{b}}{2\pi} \frac{\tilde{x}_2}{\tilde{x}_1^2 + \tilde{x}_2^2}, \\ \widetilde{\sigma}_{23} &= \widetilde{G}\widetilde{\gamma}_{23} = \frac{\widetilde{G}\tilde{b}}{2\pi} \frac{\tilde{x}_1}{\tilde{x}_1^2 + \tilde{x}_2^2}, \end{aligned} \tag{2.13}$$

where $\widetilde{G}$ is the shear modulus. It is apparent that the screw dislocation only causes shear stresses and the normal stresses are zero. Thus the dislocation does not cause a hydrostatic stress field. As a result the screw dislocation can interact with other dislocations both edge and screw type and free surfaces (e.g. image dislocation) described by the Peach-Koehler equation introduced in chapter 2.3.1. However, there is no elastic interaction with point defects as diffusive ions or vacancies.

Edge dislocation in an infinitely long cylinder

An edge dislocation is placed in an infinitely long cylinder in positive x_3 direction, and its Burgers vector is in positive x_1 direction, as indicated in figure 2.2a. The edge dislocation is characterised in that the displacements are within the x_1 and x_2 directions where the x_3 direction is displacement free. It can be formulated as a plain strain problem in 2 dimensions in an infinitely long cylinder that can be solved by finding the Airy stress equation satisfying the biharmonic equation.

$$\left(\frac{\partial^2}{\partial\tilde{x}_1^2}+\frac{\partial^2}{\partial\tilde{x}_2^2}\right)\left(\frac{\partial^2}{\partial\tilde{x}_1^2}+\frac{\partial^2}{\partial\tilde{x}_2^2}\right)\widetilde{\Phi}(\tilde{x}_1,\tilde{x}_2)=0, \tag{2.14}$$

with the solution of the stress function $\widetilde{\Phi}(\tilde{r},\theta)$in cylindrical coordinates

$$\widetilde{\Phi}(\tilde{r},\theta)=(\widetilde{B}\tilde{r}^3-\widetilde{A}\tilde{r}\ln\tilde{r})\sin\theta, \tag{2.15}$$

where $\widetilde{A}$ and $\widetilde{B}$ are variable terms that are evaluated from the boundary conditions as $\widetilde{B}=0$ and $\widetilde{A}=\widetilde{G}\tilde{b}/[2\pi(1-\nu)]$. The displacement field of an edge dislocation is

$$\begin{aligned}\tilde{u}_1^{\infty}&=\frac{\tilde{b}}{2\pi}\left[\arctan\left(\frac{\tilde{x}_2}{\tilde{x}_1}\right)+\frac{1}{2(1-\nu)}\frac{\tilde{x}_1\tilde{x}_2}{\tilde{x}_1^2+\tilde{x}_2^2}\right],\\ \tilde{u}_2^{\infty}&=-\frac{\tilde{b}}{2\pi}\left[\frac{1-2\nu}{4(1-\nu)}\ln(\tilde{x}_1^2+\tilde{x}_2^2)+\frac{1}{4(1-\nu)}\frac{\tilde{x}_1^2-\tilde{x}_2^2}{\tilde{x}_1^2+\tilde{x}_2^2}\right].\end{aligned} \tag{2.16}$$

The non zero components of the stress field are

$$\begin{aligned}\widetilde{\sigma}_{11}^{\infty}&=\frac{\partial^2\widetilde{\Phi}^{\infty}}{\partial\tilde{x}_2^2}=-\frac{\widetilde{G}\tilde{b}}{2\pi(1-\nu)}\frac{\tilde{x}_2(3\tilde{x}_1^2+\tilde{x}_2^2)}{(\tilde{x}_1^2+\tilde{x}_2^2)^2},\\ \widetilde{\sigma}_{22}^{\infty}&=\frac{\partial^2\widetilde{\Phi}^{\infty}}{\partial\tilde{x}_1^2}=\frac{\widetilde{G}\tilde{b}}{2\pi(1-\nu)}\frac{\tilde{x}_2(\tilde{x}_1^2-\tilde{x}_2^2)}{(\tilde{x}_1^2+\tilde{x}_2^2)^2},\\ \widetilde{\sigma}_{12}^{\infty}&=-\frac{\partial^2\widetilde{\Phi}^{\infty}}{\partial\tilde{x}_1\partial\tilde{x}_2}=\frac{\widetilde{G}\tilde{b}}{2\pi(1-\nu)}\frac{\tilde{x}_1(\tilde{x}_1^2-\tilde{x}_2^2)}{(\tilde{x}_1^2+\tilde{x}_2^2)^2},\\ \widetilde{\sigma}_{33}^{\infty}&=\nu(\widetilde{\sigma}_{11}^{\infty}+\widetilde{\sigma}_{22}^{\infty})=-\frac{\widetilde{G}\tilde{b}\nu}{\pi(1-\nu)}\frac{\tilde{x}_2}{(\tilde{x}_1^2+\tilde{x}_2^2)}.\end{aligned} \tag{2.17}$$

The stress fields have both normal and shear components. The resulting hydrostatic stress field enables strong elastic interaction with point defects. In real materials dislocations are not ideally straight and can contain both screw and edge components. The elastic

fields are then described as a superposition of the stress fields of the screw and edge dislocation, where the fraction is described with the dislocation character angle ϕ. As only the edge component causes a hydrostatic stress, point defects can only interact with the edge component. Therefore this work will focus on edge dislocations and the observations can be interpolated on curved dislocations, where the strongest interaction will be in areas with pure edge component and will decrease with increasing screw component.

Edge dislocation in an infinitely long cylinder of finite radius

For dislocations in a finite medium surface effects have to be taken into account. The free surface will act in the form of image stresses on the dislocation. The corrections for the resulting stress field are here exemplary shown for an edge dislocation in a cylinder with finite radius, based on the solution of the edge dislocation in a cylinder with infinite radius. The corrected stress field has to fulfill the traction free boundary conditions at the cylindrical surface, such that

$$\widetilde{\sigma}_{rr}(\tilde{r} = \widetilde{R}) = \widetilde{\sigma}_{\theta\tilde{r}}(\tilde{r} = \widetilde{R}) = 0, \tag{2.18}$$

with an image function describing a correction field

$$\widetilde{\Phi}^{img} = \widetilde{B}\tilde{r}^3 \sin\theta, \tag{2.19}$$

with $\widetilde{B}$ a non-zero constant defined by the boundary conditions. Calculating the image stress fields leads to the non-zero components of the stress field as

$$\begin{aligned}
\widetilde{\sigma}_{rr} &= \widetilde{\sigma}_{rr}^{\infty} + \widetilde{\sigma}_{rr}^{img} = -\frac{\widetilde{G}\tilde{b}\sin\theta}{2\pi(1-\nu)\tilde{r}}\left[1 - \left(\frac{\tilde{r}}{\widetilde{R}}\right)^2\right], \\
\widetilde{\sigma}_{\theta\theta} &= \widetilde{\sigma}_{\theta\theta}^{\infty} + \widetilde{\sigma}_{\theta\theta}^{img} = -\frac{\widetilde{G}\tilde{b}\sin\theta}{2\pi(1-\nu)\tilde{r}}\left[1 - 3\left(\frac{\tilde{r}}{\widetilde{R}}\right)^2\right], \\
\widetilde{\sigma}_{\tilde{r}\theta} &= \widetilde{\sigma}_{\tilde{r}\theta}^{\infty} + \widetilde{\sigma}_{\tilde{r}\theta}^{img} = -\frac{\widetilde{G}\tilde{b}\cos\theta}{2\pi(1-\nu)\tilde{r}}\left[1 - \left(\frac{\tilde{r}}{\widetilde{R}}\right)^2\right].
\end{aligned} \tag{2.20}$$

Screw dislocation in an infinitely long cylinder of finite radius

The derivation for the stress field of a screw dislocation in an infinitely long cylinder of finite radius is similar to that for the edge dislocation. It is not shown here but details can

be found in [13]. The nonzero component of the stress field is

$$\widetilde{\sigma}_{\theta 3} = \widetilde{\sigma}_{\theta 3}^{\infty} - \widetilde{\sigma}_{3\theta}^{img} = \frac{\widetilde{G}\tilde{b}}{2\pi\tilde{r}} - \frac{\widetilde{G}\tilde{b}}{\pi\widetilde{R}^2}\tilde{r}. \tag{2.21}$$

2.2.2 Non-singular dislocation models

Although the classic analytical solution for dislocation stress fields provides mathematical simplicity, the singularity at the dislocation core is a major drawback when it comes to simulation. Also the dislocation core is not naturally described by the simple form and the dislocation self energy cannot be calculated straight forward. This motivates dislocation models that remove the singularity at the dislocation core and give a physically sound description of the dislocation core. The non-singular dislocation theories described in this chapter are based on a spreading function for the Burgers vector [12] and the gradient elasticity [63, 38].

Non-singular dislocation model with distributed dislocation core

In the following the non-singular solution for dislocations developed by Cai et al. [12] is presented, which utilizes a spreading of the Burgers vector as

$$\tilde{b}_i = \int \tilde{\zeta}(\tilde{x}) d^3\tilde{x}, \tag{2.22}$$

with the Burgers vector density function

$$\tilde{\zeta}(\tilde{x}) = \tilde{b}_i \hat{w}(\tilde{x}). \tag{2.23}$$

The distribution function $\bar{w}(\tilde{x})$ is defined as the convolution of the distribution function $\hat{w}(\tilde{x})$ with itself

$$\bar{w}(\tilde{x}) = \hat{w}(\tilde{x}) * \hat{w}(\tilde{x}), \tag{2.24}$$

which has the analytical form

$$\bar{w}(\tilde{x}) = \frac{15}{8\pi\tilde{h}^3[(\tilde{r}/\tilde{h})^2 + 1]^{7/2}}, \tag{2.25}$$

where $\tilde{r} = ||\tilde{x}||$. The second spreading function $\bar{w}(\tilde{\mathbf{x}})$ modifies the distance function $\widetilde{R} = \sqrt{\tilde{x}_1^2 + \tilde{x}_2^2 + \tilde{x}_3^2}$ to $\widetilde{R}_h = \sqrt{\widetilde{R}^2 + \tilde{h}^2}$ and introduces the dislocation core parameter

$\tilde{h}$. For $\tilde{h} > 0$, the modified distance function $\widetilde{R}_h$ is non-zero and the singularity at the dislocation core is removed. For large distances from the core, $\widetilde{R}_h \approx \widetilde{R}$, so that the resulting non-singular solution closely correlates to the singular solution of the classical theory outside the dislocation core.The analytical form of $\hat{w}(\tilde{x})$ is unknown, but it can be approximated via

$$\hat{w} = \frac{15}{8\pi}\left[\frac{1-m}{\tilde{h}_1^3(\tilde{r}^2/\tilde{h}_1^2+1)^{7/2}} + \frac{m}{\tilde{h}_2^3(\tilde{r}^2/\tilde{h}_2^2+1)^{7/2}}\right]. \tag{2.26}$$

Here $\tilde{h}_1 = 0.9038\tilde{h}$, $\tilde{h}_2 = 0.5451\tilde{h}$ and $m = 0.6575$. The eigendistortion of the dislocation can then be written as the convolution with the distribution function as [101]

$$\beta_{ij}^{p} = \beta_{ij}^{p0} * \hat{w}(\tilde{x}). \tag{2.27}$$

The non-singular analytical solutions for the stress fields of an infinite straight screw dislocation are

$$\begin{aligned}
\widetilde{\sigma}_{13} &= -\frac{\widetilde{G}\tilde{b}}{2\pi}\frac{\tilde{x}_2}{\widetilde{\rho}_h^2}\left(1+\frac{\tilde{h}^2}{\widetilde{\rho}_h^2}\right),\\
\widetilde{\sigma}_{23} &= \frac{\widetilde{G}\tilde{b}}{2\pi}\frac{\tilde{x}_1}{\widetilde{\rho}_h^2}\left(1+\frac{\tilde{h}^2}{\widetilde{\rho}_h^2}\right),\\
\widetilde{\sigma}_{11} &= \widetilde{\sigma}_{22} = \widetilde{\sigma}_{33} = \widetilde{\sigma}_{12} = 0,
\end{aligned} \tag{2.28}$$

where $\widetilde{G}$ is the shear modulus and $\tilde{\rho}_h = \sqrt{\tilde{x}_1^2+\tilde{x}_2^2+\tilde{h}^2}$. The non-singular analytical solutions for the stress fields of an infinite straight edge dislocation are

$$\begin{aligned}
\widetilde{\sigma}_{11} &= -\frac{\widetilde{G}\tilde{b}}{2\pi(1-\nu)}\frac{\tilde{x}_2}{\tilde{\rho}_h^2}\left(1+\frac{2(\tilde{x}_1^2+\tilde{h}^2)}{\tilde{\rho}_h^2}\right),\\
\widetilde{\sigma}_{22} &= \frac{\widetilde{G}\tilde{b}}{2\pi(1-\nu)}\frac{\tilde{x}_2}{\tilde{\rho}_h^2}\left(1-\frac{2(\tilde{x}_2^2+\tilde{h}^2)}{\tilde{\rho}_h^2}\right),\\
\widetilde{\sigma}_{33} &= -\frac{\widetilde{G}\tilde{b}\nu}{\pi(1-\nu)}\frac{\tilde{x}_2}{\tilde{\rho}_h^2}\left(1+\frac{\tilde{h}^2}{\tilde{\rho}_h^2}\right),\\
\widetilde{\sigma}_{12} &= \frac{\widetilde{G}\tilde{b}}{2\pi(1-\nu)}\frac{\tilde{x}_1}{\tilde{\rho}_h^2}\left(1-\frac{2\tilde{x}_2^2}{\tilde{\rho}_h^2}\right),\\
\widetilde{\sigma}_{13} &= \widetilde{\sigma}_{23} = 0,
\end{aligned} \tag{2.29}$$

where ν is the Poisson's ratio. As a conclusion the description of the dislocation stress field is non-singular and the stresses in the dislocation core are physical reasonable. The core parameter $\tilde{h}$ can also be understood as a balancing parameter for the dislocation self energy, with that the strain energy outside the dislocation core is balanced to the strain energy inside the core. The core width can be found by calibrating the dislocation self energy found in atomistic simulation to the non-singular continuum self energy. Note that for $\tilde{h} = 0$ the singular solution for the dislocation in an infinitely long cylinder is retrieved.

Non-singular dislocation model in strain gradient elasticity

A different approach to an analytical non-singular solution for dislocations is within the framework of strain gradient elasticity by Lazar [63, 60]. In this theory a characteristic length scale $\tilde{l}$ related to the dislocation core is introduced and non-singular displacement fields for the dislocations are derived. The classical dislocation density and plastic distortion tensors formulated by DeWit [21] and Kosseka [58] are reformulated to a non-singular form. The strain energy density of the simplified strain gradient elasticity is

$$\widetilde{W}^{sge} = \frac{1}{2}\widetilde{C}^{sge}_{ijkl}\beta_{ij}\beta_{kl} + \frac{1}{2}\tilde{l}^2\widetilde{C}^{sge}_{ijkl}\partial_m\beta_{ij}\partial_m\beta_{kl}, \tag{2.30}$$

with the isotropic elasticity tensor $\widetilde{C}^{sge}_{ijkl} = G(\delta_{ik}\delta_{jl} + \delta_{il}\delta_{jk}) + \tilde{\lambda}\delta_{ij}\delta_{kl}$ and the elastic distortion tensor β_{ij}. The three dimensional Green tensor of the Helmholz Navier equation is calculated as

$$\widetilde{G}_{ij}(\widetilde{R}) = \frac{1}{16\pi\widetilde{G}(1-\nu)}[2(1-\nu)\delta_{ij}\Delta - \partial_i\partial_j]\widetilde{A}(\widetilde{R}), \tag{2.31}$$

with

$$\widetilde{A}(\widetilde{R}) = \widetilde{R} + \frac{2\tilde{l}^2}{\widetilde{R}}(1 - e^{-\widetilde{R}/\tilde{l}}), \tag{2.32}$$

and the position defined as $\widetilde{R} = |\tilde{x} - \tilde{x}'|$. The Green tensor is non-singular and is written in the explicit form as

$$\begin{aligned}\widetilde{G}_{ij}(\widetilde{R}) = \frac{1}{16\pi\widetilde{G}(1-\nu)}\Bigg[&\frac{\delta_{ij}}{\widetilde{R}}\Bigg((3-4\nu)(1-e^{-\widetilde{R}/\tilde{l}}) \\ &+\frac{1}{\widetilde{R}^2}(2\tilde{l}^2 - (\widetilde{R}^2 + 2\tilde{l}\widetilde{R} + 2\tilde{l}^2)e^{-\widetilde{R}/\tilde{l}})\Bigg) \\ &+\frac{\widetilde{R}_i\widetilde{R}_j}{\widetilde{R}^3}\left(1 - \frac{6\tilde{l}^2}{\widetilde{R}^2} + \left(2 + \frac{6\tilde{l}}{\widetilde{R}} + \frac{6\tilde{l}^2}{\widetilde{R}^2}\right)e^{-\widetilde{R}/\tilde{l}}\right)\Bigg].\end{aligned} \tag{2.33}$$

The eigendistortion of the dislocation can then be written as [101]

$$\beta_{ij}^{p} = \beta_{ij}^{p0} * \widetilde{G}, \tag{2.34}$$

where $\widetilde{G}$ is the isotropic Green's function, with $\widetilde{G}_{ij} = \widetilde{G}_{ij}^{0} * \widetilde{G}$. The explicit form of the distortion tensor is given for straight dislocations [61]. For the screw dislocation in the anti-plain strain problem the non-vanishing components of the non-singular distortion tensor are

$$\beta_{31} = -\frac{\tilde{b}_3}{2\pi}\frac{\tilde{x}_2}{\tilde{r}^2}\left(1 - \frac{\tilde{r}}{\tilde{l}}K_1(\tilde{r}/\tilde{l})\right), \tag{2.35}$$

$$\beta_{32} = \frac{\tilde{b}_3}{2\pi}\frac{\tilde{x}_1}{\tilde{r}^2}\left(1 - \frac{\tilde{r}}{\tilde{l}}K_1(\tilde{r}/\tilde{l})\right), \tag{2.36}$$

with K_i the modified Bessel function of order i and $\tilde{r} = \sqrt{\tilde{x}_1^2 + \tilde{x}_2^2}$. The non-vanishing components of the non-singular distortion tensor for the edge dislocation for the plain strain problem are

$$\begin{aligned}\beta_{11} = -\frac{\tilde{b}_1}{4\pi(1-\nu)}\frac{\tilde{x}_2}{\tilde{r}^2}\Bigg((1-2\nu) + \frac{2\tilde{x}_1^2}{\tilde{r}^2} + \frac{4\tilde{l}^2}{\tilde{r}^4}(\tilde{x}_2^2 - 3\tilde{x}_1^2) \\ - \frac{2(\tilde{x}_2^2 - 3\tilde{x}_1^2)}{\tilde{r}^2}K_2(\tilde{r}/\tilde{l}) - \frac{2(\tilde{x}_2^2 - \nu\tilde{r}^2)}{\tilde{l}\tilde{r}}K_1(\tilde{r}/\tilde{l})\Bigg),\end{aligned} \tag{2.37}$$

$$\begin{aligned}\beta_{12} = \frac{\tilde{b}_1}{4\pi(1-\nu)}\frac{\tilde{x}_1}{\tilde{r}^2}\Bigg((3-2\nu) - \frac{2\tilde{x}_2^2}{\tilde{r}^2} - \frac{4\tilde{l}^2}{\tilde{r}^4}(\tilde{x}_1^2 - 3\tilde{x}_2^2) \\ + \frac{2(\tilde{x}_1^2 - 3\tilde{x}_2^2)}{\tilde{r}^2}K_2(\tilde{r}/\tilde{l}) - \frac{2(\tilde{x}_2^2 + (1-\nu)\tilde{r}^2)}{\tilde{l}\tilde{r}}K_1(\tilde{r}/\tilde{l})\Bigg),\end{aligned} \tag{2.38}$$

$$\begin{aligned}\beta_{21} = -\frac{\tilde{b}_1}{4\pi(1-\nu)}\frac{\tilde{x}_1}{\tilde{r}^2}\Bigg((1-2\nu) + \frac{2\tilde{x}_2^2}{\tilde{r}^2} + \frac{4\tilde{l}^2}{\tilde{r}^4}(\tilde{x}_1^2 - 3\tilde{x}_2^2) \\ - \frac{2(\tilde{x}_1^2 - 3\tilde{x}_2^2)}{\tilde{r}^2}K_2(\tilde{r}/\tilde{l}) + \frac{2(\tilde{x}_2^2 - (1-\nu)\tilde{r}^2)}{\tilde{l}\tilde{r}}K_1(\tilde{r}/\tilde{l})\Bigg),\end{aligned} \tag{2.39}$$

$$\begin{aligned}\beta_{22} = -\frac{\tilde{b}_1}{4\pi(1-\nu)}\frac{\tilde{x}_2}{\tilde{r}^2}\Bigg((1-2\nu) - \frac{2\tilde{x}_1^2}{\tilde{r}^2} - \frac{4\tilde{l}^2}{\tilde{r}^4}(\tilde{x}_2^2 - 3\tilde{x}_1^2) \\ + \frac{2(\tilde{x}_2^2 - 3\tilde{x}_1^2)}{\tilde{r}^2}K_2(\tilde{r}/\tilde{l}) - \frac{2(\tilde{x}_1^2 - \nu\tilde{r}^2)}{\tilde{l}\tilde{r}}K_1(\tilde{r}/\tilde{l})\Bigg).\end{aligned} \tag{2.40}$$

Discussion

Within this chapter three models for dislocations have been discussed, which are the classical singular model and two non-singular models from Cai et al. [12] and Lazar et al. [61]. The main drawback of the classical model is the singularity at the dislocation core introduced by the delta function which deviates from the behavior of dislocations in real materials that can only have finite displacement and stress within the dislocation core. The non-zero stress fields of an edge dislocation calculated with the different models are summarized in figure 2.3. The parameter $\tilde{h} = 2$ nm in the model of Cai et al. is defined as the core width and the parameter $\tilde{l} = 1$ nm in the Model of Lazar et al. is defined as the core radius. The non-zero stress fields are compared in figure 2.3. It is shown that the predicted stress fields of the non-singular solutions are finite within the dislocation core region and converge to the singular solution for large distances compared to the core radius. The two non-singular solutions have a similar course, although the solution of Lazar et al. has the maximum closer to the dislocation core.

It is of high interest to implement a non-singular dislocation solution in numerical models as the infinite stress at the dislocation core of the singular solution is physically impossible. Further the numerically computed stresses of an infinite analytical solution can only be a large but finite approximation, which strongly depends on the mesh as the approximation will more and more approach the analytical infinite solution the more the mesh is refined. Both non-singular models provide solutions for arbitrary shaped dislocations in 3 dimensions. The advantages and disadvantages are discussed in the following. The model of Cai et al. has the advantage of a simple formulation related to the distance function $\tilde{\rho}_h$ and the distribution function $\bar{w}$. However, the distribution function $\hat{w}$ is only derived in the form of a numeric approximation, so that the model lacks the analytic closed forms of the Burgers equation and the Peach-Koehler stress equation [101]. Further the calculated stress field is convoluted with the distribution function such that the calculation of the Peach-Koehler force needs an integration operation. The approach by Lazar et al. provides closed form analytical forms of the Burgers equation and the Peach-Koehler stress equation [101]. However, the formulation in the strain gradient elasticity introduces more complexity compared to linear elastic models. In this model the mechanical problem is solved in the form of a displacement field and the dislocation is implemented in the form of an eigenstrain distortion. The interaction of dislocations with other defects or external forces is implicitly covered by solving the partial differential equation for the displacement field. Therefore an explicit form of the Peach-Koehler force is not required in the model. Also the numerical approximation of the distribution function is acceptable due to the approximative nature of the FEM. With that the advantage of a mathematical simple form

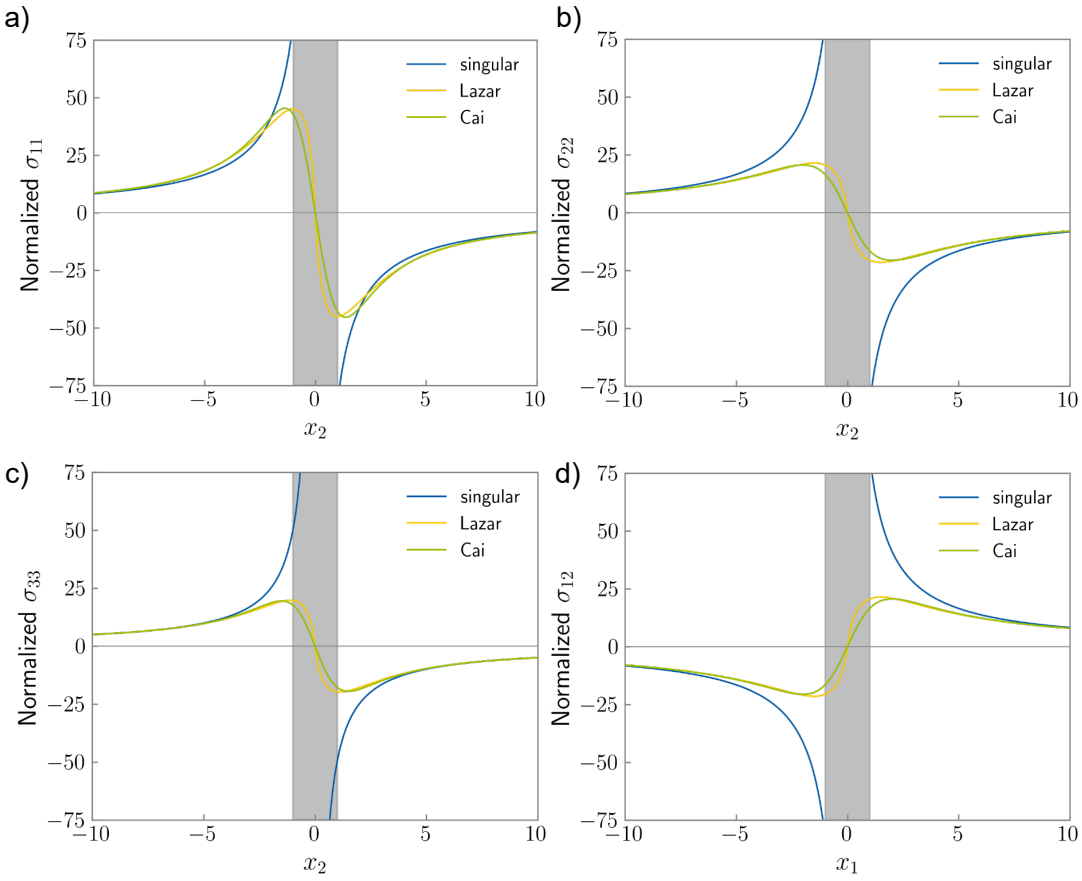

Figure 2.3: Comparison of the stress field solutions from the classical singular dislocation model [13], the non-singular dislocation model in strain gradient elasticity by Lazar et al. [63, 60] and the non-singular dislocation model with distributed dislocation core by Cai et al. [12].

the model following Cai et al. [12] is an excellent choice for the numerical non-singular dislocation model. A single integration operation is sufficient for the convolution of the Burgers vector to obtain the non-singular dislocation eigenstrain.

2.3 Driving Forces on Dislocations

Driving forces on dislocations can be understood in the sense of an energy release rate during the movement of the dislocation. The evaluation of the driving forces on a dislocation defect are schematically depicted in figure 2.4. The methods considered in this work are the calculation of the Peach-Koehler force and the configurational forces. The driving force on a point P on the dislocation line can be calculated by the Peach-Koehler force. Driving forces on a dislocation can also be obtained within the configurational mechanics, and are found by integrating the configurational forces along the Burgers surface S. At the end of this section it will be shown that the two methods are equivalent when only linear elastic contributions are considered.

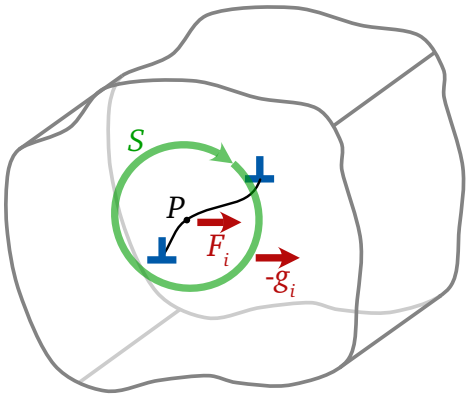

Figure 2.4: Driving forces on an edge dislocation. For this configuration the configurational forces g_i obtained from the integration along the surface S are equivalent to the Peach-Koehler force F_i.

2.3.1 Peach-Koehler force

The Peach-Koehler force first introduced in 1950 [99] evaluates the force acting on a dislocation due to a local stress field. The Peach-Koehler equation [43] translates the stresses to a driving force on one unit length of the dislocation

$$\widetilde{\mathbf{F}} = (\widetilde{\sigma} \cdot \tilde{\mathbf{b}}) \times \xi, \tag{2.41}$$

which is written in index notation as

$$\widetilde{F}_k = \epsilon_{kij} \widetilde{\sigma}_{il} \tilde{b}_l \xi_j. \tag{2.42}$$

The stress $\widetilde{\sigma}$ can exemplarily be an external stress field due to mechanical loading, the stress field of other defects such as dislocations or the stress field from an image dislocation at a free surface in a finite volume. The interaction forces between dislocations finds wide application in discrete dislocation dynamics [123, 121, 32, 52]. Typically the stress field of the dislocation is expressed in the classic singular theory, which then also leads to unphysical singular forces for distances smaller than the dislocation core. Non-singular forces can be obtained by expressing the stress field with non-singular dislocation theory [59]. The direction of the force is independent on the definition of the dislocation with its sense vector ξ and the Burgers vector $\tilde{\mathbf{b}}$, because if the sense vector is reversed, then the Burgers vector will be reversed as well. The relation of the Peach-Koehler force with the work required for the displacement of a dislocation can be shown in the derivation with the infinitesimal work approach [99, 77]. The Peach-Koehler equation can also be derived from the configurational force proving the equivalence between the Peach-Koehler force and the configurational force, which is shown in the next section. The Peach-Koehler force is utilized for benchmarking the driving forces on dislocations numerically computed with the configurational mechanics in chapter 2.5.6 and 2.5.7.

2.3.2 Configurational mechanics of dislocations

One general approach to calculate driving forces on defects is within the configurational mechanics (see e.g. [90]). The configurational force balance allows to directly evaluate forces on defects within a volume. For the pure mechanical case, the strain energy density $\tilde{f} = \hat{f}(\tilde{u}_{i,j}; \tilde{x}_k)$ is a function of the strain and position for a body subject to body forces $\tilde{q}_i$ where the symmetric stresses satisfy the equilibrium condition in equation 2.2. From the identity,

$$\dot{\tilde{f}} - \widetilde{\sigma}_{ij} \dot{\tilde{u}}_{i,j} = 0, \tag{2.43}$$

the configurational force balance in the local form can be derived as [90]

$$\widetilde{\Sigma}_{kj,j} + \tilde{g}_k = 0, \tag{2.44}$$

where the Eshelby stress tensor is

$$\widetilde{\Sigma}_{kj} = \tilde{f}\delta_{kj} - \widetilde{\sigma}_{ij}\tilde{u}_{i,k}, \tag{2.45}$$

and the configurational body forces $\tilde{g}_k$ are given by

$$\tilde{g}_k = -\tilde{q}_i\tilde{u}_{i,k} - \left.\frac{\partial \tilde{f}}{\partial \tilde{x}_k}\right|_{expl.}, \tag{2.46}$$

where the free energy density explicitly depends on the position. Integration of the Eshelby stress tensor or the configurational body forces returns the average of the forces within the integration volume. This means that the driving forces on a defect can be found by defining the integration area such that only the defect is contained. One major advantage is that the configurational mechanics can be generalized, as the configurational force balance can also be derived from the free energy density. Then by considering contributions such as chemical or electrostatic to the free energy density, a multiphysical force on the defect can be found [131].

In the following the configurational mechanics for dislocations are introduced according to ref. [139]. Subsequently it is shown that the Peach-Koehler force can be derived from the configurational forces [3, 139]. Consider a body containing an edge dislocation with Burgers vector $\tilde{b}$ but free of body forces, e.g. $\tilde{q}_i = 0$. The configurational forces are reformulated to explicitly include the dislocation. Therefore the elastic distortion of a dislocated body is defined as

$$\beta_{ij} = \tilde{u}_{i,j} - \beta^D_{ij}, \tag{2.47}$$

with the displacement gradient $\tilde{u}_{i,j}$ and the dislocation induced distortion β^D_{ij}. Integration along the Burgers circuit $\widetilde{\mathbf{C}}$ allows to define the Burgers vector as

$$\tilde{b}_i = -\oint_{\widetilde{\mathbf{C}}} \beta^D_{ij}\tilde{l}_j = \oint \beta^D_{ij}\tilde{l}_j = \int_{\widetilde{\mathbf{S}}} \alpha_{ij} d\widetilde{\mathbf{S}}_j, \tag{2.48}$$

where $\widetilde{\mathbf{S}}$ is the surface bounded by $\widetilde{\mathbf{C}}$ and the dislocation density α_{ij} is defined as

$$\alpha_{ij} = -\epsilon_{jkl}\beta^D_{il,k} \quad \text{and} \quad \alpha_{ij} = \epsilon_{jkl}\beta_{il,k}, \tag{2.49}$$

where ϵ_{jkl} is the permutation tensor. The strain energy density now includes the dislocation contribution with

$$\tilde{f} = \frac{1}{2}\widetilde{\sigma}_{ij}\left(\varepsilon_{ij} - \varepsilon_{ij}^{D}\right) = \frac{1}{2}\widetilde{\sigma}_{ij}\beta_{ij}, \tag{2.50}$$

with the gradient

$$\tilde{f}_{,k} = \widetilde{\sigma}_{ij}\beta_{ij,k} = \widetilde{\sigma}_{ij}\left(\beta_{ij,k} - \beta_{ik,j}\right) + \widetilde{\sigma}_{ij}\beta_{ik,j}. \tag{2.51}$$

Multiplication of equation 2.49 with ϵ_{kjl} gives $\epsilon_{kjl}\alpha_{ij} = \beta_{ij,k} - \beta_{ik,j}$. By using the mechanical equilibrium condition the strain energy density gradient can be rewritten as

$$\tilde{f}_{,k} = \widetilde{\sigma}_{ij}\epsilon_{kjl}\alpha_{il} + \left(\widetilde{\sigma}_{ij}\beta_{ik}\right)_{,j} - \widetilde{\sigma}_{ij,j}\beta_{ik} = \widetilde{\sigma}_{ij}\epsilon_{kjl}\alpha_{il} + \left(\widetilde{\sigma}_{ij}\beta_{ik}\right)_{,j}. \tag{2.52}$$

This relation can be rearranged to the local form

$$\widetilde{\Sigma}_{kj,j} + \tilde{g}_k = 0, \tag{2.53}$$

with the Eshelby stress tensor

$$\widetilde{\Sigma}_{kj} = \tilde{f}\delta_{kj} - \widetilde{\sigma}_{ij}\beta_{ik}, \tag{2.54}$$

and the configurational forces

$$\tilde{g}_k = -\epsilon_{kjl}\widetilde{\sigma}_{ij}\alpha_{il}. \tag{2.55}$$

As an example, a straight dislocation is defined by its dislocation density $\alpha_{il} = \tilde{b}_i\delta(\tilde{x}_1 - \tilde{x}_1^D)\delta(\tilde{x}_2 - \tilde{x}_2^D)\hat{\xi}_l$. The integral

$$\tilde{f}_k = \int_{\widetilde{\mathbf{S}}} \widetilde{\Sigma}_{kj,j} d\widetilde{\mathbf{S}} = -\int_{\widetilde{\mathbf{S}}} \tilde{g}_k d\widetilde{\mathbf{S}} = \epsilon_{kjl}\widetilde{\sigma}_{ij}^{0}\tilde{b}_i\hat{\xi}_l, \tag{2.56}$$

returns the Peach-Koehler force given in equation 2.42 [99], where $\tilde{x}_i^D$ is the location of the dislocation line, $\hat{\xi}_l$ is the sense vector of the dislocation line, and $\widetilde{\sigma}_{ij}^{0} = \widetilde{\sigma}_{ij}|_{\tilde{x}_i=\tilde{x}_i^D}$ is the stress field at dislocation core due to external loading. For more details regarding the physical interpretation of the Eshelby stress tensor and Peach-Koehler force, one can refer to ref. [62, 3].

2.4 Non-singular Continuum Dislocation Model

2.4.1 Singular representation

The description for a dislocation as an eigenstrain defined on the dislocation slip plane is shown in the following. The description is based on the Dirac delta distribution and

is singular. Considered is a dislocated body $\mathrm{B} \subset \mathbb{R}^3$ with a volume V enclosed by the boundary $S = \partial\mathrm{B}$. The dislocated body is governed by the mechanical equilibrium

$$\widetilde{\sigma}_{ij,j} = 0 \quad \text{in} \quad \mathrm{B}, \tag{2.57}$$

by taking the assumptions for small strain and a quasistatic problem into account, where $\widetilde{\sigma}_{ij}$ is the stress tensor, and the body force is neglected. The general anisotropic linear constitutive relation for the stress $\widetilde{\sigma}_{ij}$ and elastic strain ε_{ij}^{E} is given as

$$\widetilde{\sigma}_{ij} = \widetilde{C}_{ijkl}\varepsilon_{kl}^{E} = \widetilde{C}_{ijkl}\left(\varepsilon_{kl} - \varepsilon_{kl}^{D}\right), \tag{2.58}$$

where $\widetilde{C}_{ijkl}$ is the stiffness tensor, ε_{kl}^{E} is the elastic strain and ε_{kl}^{D} is the eigenstrain of dislocations. With the assumption of linear elasticity, that means small deformations can be described by an infinitesimal strain tensor, the total strain ε_{kl} is defined as the symmetric part of the displacement gradient $\tilde{u}_{k,l}$ as

$$\varepsilon_{kl} = \frac{1}{2}\left(\tilde{u}_{k,l} + \tilde{u}_{l,k}\right). \tag{2.59}$$

Either displacement or traction boundary condition can be considered

$$\tilde{u}_i = \bar{u}_i \quad \text{or} \quad \widetilde{\sigma}_{ij}n_j = \tilde{t}_i \quad \text{on} \quad S, \tag{2.60}$$

where $\bar{u}_i$ is the prescribed displacement on the boundary, n_j is the normal vector of the boundary, and $\tilde{t}_i$ is the applied traction on the boundary. The displacement jump caused by a gliding dislocation is associated with the eigenstrain tensor ε_{ij}^{D}, which is defined as the symmetric form of the dyadic product of the Burgers vector $\tilde{b}_i$ and the normal vector n_i of the slip plane $\widetilde{\mathbf{D}}$

$$\varepsilon_{ij}^{D}(\tilde{\mathbf{x}}) = \frac{1}{2}\left(\tilde{b}_i n_j + \tilde{b}_j n_i\right)\delta(\tilde{\mathbf{x}} - \widetilde{\mathbf{D}}) = \frac{1}{2}\int_{\widetilde{D}}\left(\tilde{b}_i n_j + \tilde{b}_j n_i\right)\delta(\tilde{\mathbf{x}} - \tilde{\mathbf{x}}^{D})d\widetilde{D}(\tilde{\mathbf{x}}^{D}), \tag{2.61}$$

where $\delta(\tilde{\mathbf{x}} - \widetilde{\mathbf{D}})$ is the one-dimensional Dirac delta function in the normal direction of the slip plane $\widetilde{\mathbf{D}}$. The second equality in equation(2.61) indicates that the Burgers vector distribution is described by the three-dimensional Dirac delta function $\delta(\tilde{\mathbf{x}} - \tilde{\mathbf{x}}^{D})$, where $\tilde{x}_i^{D}$ denotes the location vector of points on the slip plane [91]. Equation 2.61 confines the location of the eigenstrain onto the slip plane, i.e. when $\tilde{\mathbf{x}} \in \widetilde{\mathbf{D}}$. In the eigenstrain theory, by introducing the dislocation density concept, the Burgers vector can be defined as [2]

$$\tilde{b}_i = -\oint_{\widetilde{\mathbf{C}}} \beta_{ij}^{D} d\tilde{C}_j = \int_{\tilde{\mathbf{A}}} \alpha_{ij} d\tilde{A}_j, \tag{2.62}$$

where $\widetilde{\mathbf{C}}$ is the Burgers circuit and $\tilde{\mathbf{A}}$ is the Burgers surface bounded by $\widetilde{\mathbf{C}}$. Here $\beta_{ij}^{D} = \tilde{b}_i n_j \delta(\mathbf{x})$ is the plastic distortion due to the dislocation and α_{ij} is the dislocation density tensor defined in equation 2.49.

2.4.2 Non-singular representation

The major drawback of the classical solution discussed above is the singularity at the dislocation core related to the delta function. Therefore the solution is only valid outside the core, and the singularity within the core has no physical meaning and leads to numerical inconvenience for the numerical simulation. An alternative is to spread the eigenstrain over the region surrounding the slip plane (regularization of the dislocation slip) [123]. A non-singular continuum representation for spreading the Burgers vector proposed by [12] ensures that the derived stress field agrees with that of the classic solution. The model can be calibrated with a molecular dynamics model to a more accurate description of the core energy. The model is implemented based on the spread of the burgers vector around an arbitrary point on the slip plane in the three-dimensional space given in equation 2.22 utilizing the spreading functions $\hat{w}(\tilde{x})$ and $\bar{w}(\tilde{x})$ defined in equations 2.23, 2.24 and 2.26. In particular the spreading function in the framework of the non-singular continuum theory of dislocations $\hat{w}(||\tilde{\mathbf{x}} - \tilde{\mathbf{x}}^D||, \tilde{h})$ is a replacement for the Dirac delta function, so that the convolution defines the non-singular dislocation eigenstrain

$$\varepsilon_{ij}^D(\tilde{\mathbf{x}}) = \int_{\widetilde{D}} \epsilon_{ij} \hat{w}(||\tilde{\mathbf{x}} - \tilde{\mathbf{x}}^D||, \tilde{h}) \mathrm{d}\widetilde{D}(\tilde{\mathbf{x}}^D) = \epsilon_{ij} * \hat{w}(\tilde{\mathbf{x}}). \tag{2.63}$$

2.5 Implementation in the Finite Element Method

The FEM is applied to solve partial differential equations approximately discretizing the simulation space into elements, on which the PDE is solved. The FEM was implemented following the previous work [139]. In the first part of this section the variables are normalized to the natural units and the derivation of the residuals and the stiffness matrix for the implementation in the FEM formulation is shown employing the dimensionless governing equations. The model formulation is completed with the definition of the properties of $LiMn_2O_4$ applied for the isotropic examples in this work without phase separation. Artificial spurious stresses are discussed that can rise from plastic incompatibilities caused by incorrect implementation of the dislocation eigenstrain. The dislocation model is benchmarked by comparing the stress fields of an edge and a screw dislocation to the analytical solutions. The configurational mechanics for dislocations is benchmarked first by comparing the driving force on an edge dislocation in a sheared particle and second by computing the driving force on a dislocation close to a free surface and compare the

solution to the analytical calculated Peach-Koehler force resulting from the stress field of an image dislocation.

2.5.1 Numerical computation of the regularized dislocation eigenstrain

The non-singular continuum dislocation model is reformulated to a numerical computed eigenstrain. The dislocation eigenstrain in equation 2.63 is reformulated in the numerical form

$$\varepsilon_{ij}^{D}(\tilde{\mathbf{x}}) = \epsilon_{ij}\hat{W}(\tilde{\mathbf{x}}, \tilde{h}), \tag{2.64}$$

with the numerical distribution function

$$\hat{W}(\tilde{\mathbf{x}}, \tilde{h}) = \int_{\widetilde{D}} \hat{w}(||\tilde{\mathbf{x}} - \tilde{\mathbf{x}}^{D}||, \tilde{h}) \mathrm{d}\widetilde{D}(\tilde{\mathbf{x}}^{D}), \tag{2.65}$$

of the dislocation eigenstrain around the slip plane. The integration is truncated at a distance $\tilde{r}_c$ by introducing the Heaviside step function $H(\tilde{r}_c - \tilde{r})$

$$\hat{W}(\tilde{\mathbf{x}}, \tilde{h}) \cong \int_{\widetilde{D}} H(\tilde{r}_c - \tilde{r})\hat{w}(||\tilde{\mathbf{x}} - \tilde{\mathbf{x}}^{D}||, \tilde{h}) \mathrm{d}\widetilde{D}(\tilde{\mathbf{x}}^{D}) = (1-m)\hat{W}_1(\tilde{\mathbf{x}}, \tilde{h}_1) + m\hat{W}_1(\tilde{\mathbf{x}}, \tilde{h}_2), \tag{2.66}$$

with

$$\hat{W}_1(\tilde{\mathbf{x}}, \tilde{h}) = \int_{\widetilde{D}} H(\tilde{r}_c - \tilde{r}) w(||\tilde{\mathbf{x}} - \tilde{\mathbf{x}}^{D}||, \tilde{h}) \mathrm{d}\widetilde{D}(\tilde{\mathbf{x}}^{D}), \tag{2.67}$$

reducing the computation cost at the expense of an underestimation of the dislocation eigenstrain. The truncation distance of $\tilde{r}_c = 2\tilde{h}$ utilized in this work leads to an error of less than $5\,\%$ compared to the analytical solution [52]. In the following the distribution function is integrated for a two-dimensional setup where a dislocation along the x_3-axis and the slip plane normal to the x_2-axis is placed at $\tilde{\mathbf{x}} = \{0, 0, 0\}^T$ as depicted in figure 2.5a. With this the surface integration of w follows as

$$\hat{W}_1(\tilde{\mathbf{x}}, \tilde{h}) = \int_{\tilde{L}} \int_{-\tilde{r}_c}^{\tilde{r}_c} w(||\tilde{\mathbf{x}} - \tilde{\mathbf{x}}^{D}||, \tilde{h}) \mathrm{d}\tilde{x}_3^{D} \mathrm{d}\tilde{x}_1^{D}, \tag{2.68}$$

where $\tilde{L}$ is the integration path along the x_1 direction on the slip plane. With the integration domain inside $-\tilde{r}_c$ and $\tilde{r}_c$ the Heaviside step function $H(\tilde{r}_c - \tilde{r})$ can be removed. The integration along the $\tilde{x}_3^{D}$ axis is solved analytically with

$$\int_{-\tilde{r}_c}^{\tilde{r}_c} w(||\tilde{\mathbf{x}} - \tilde{\mathbf{x}}^{D}||, \tilde{h}) \mathrm{d}\tilde{x}_3^{D} = \frac{\tilde{h}^4 \tilde{r}_c (15\tilde{X}^2 + 20\tilde{r}_c^2\tilde{X} + 8\tilde{r}_c^4)}{4\pi\tilde{X}^3(\tilde{X} + \tilde{r}_c^2)^{5/2}}, \tag{2.69}$$

introducing the numerical distance function $\tilde{X} = (\tilde{x}_1 - x_1^D)^2 + \tilde{x}_2^2 + \tilde{h}^2$. The integral along the x_1 direction can only be solved numerical and is given as

$$\hat{W}_1(\tilde{\mathbf{x}}, \tilde{h}) = \sum_{i=1}^{N} \frac{\tilde{h}^4 \tilde{r}_c (15\tilde{X}_i^2 + 20\tilde{r}_c^2 \tilde{X}_i + 8\tilde{r}_c^4)}{4\pi X_i^3 (\tilde{X}_i + \tilde{r}_c^2)^{5/2}} \mathrm{d}\tilde{x}_1^D, \tag{2.70}$$

utilizing trapezoidal integration where $N = 20$ is the number of integration points. $\tilde{X}_i$ is the distance function calculated at the i-th integration point. The numerical calculated distribution $\hat{W}$ is exemplarily shown in figure 2.5b and c. Note that $\hat{W}(\tilde{\mathbf{x}}, \tilde{h})$ is treated as a constant function so that it is sufficient to be calculated once at the beginning of the simulation.

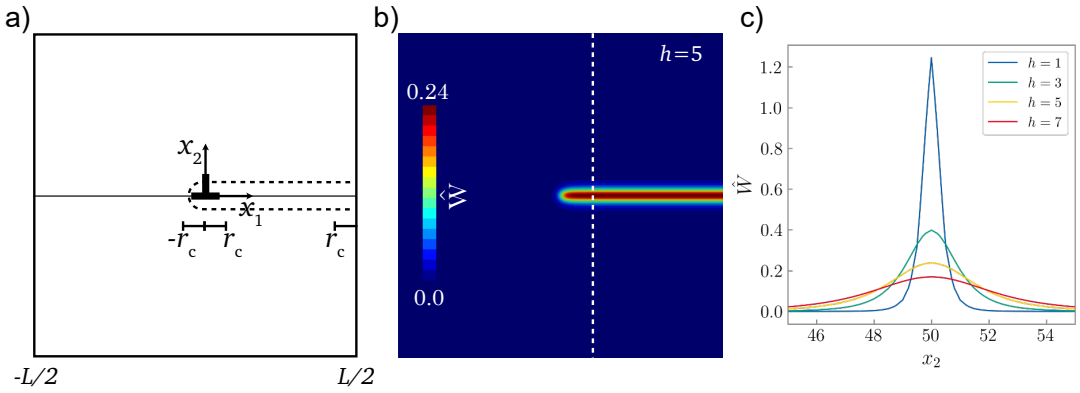

Figure 2.5: a) Schematic depiction of the integration of the distribution function $\hat{W}$. b) $\hat{W}$-distribution along the glide plane with the glideplane normal $n = (010)$ for $h = 5$. c) $\hat{W}$ plotted along the line indicated in b).

2.5.2 Finite element formulation

The variables are normalized to the natural units by defining the dimensionless stiffness tensor with $C_{ijkl} = \widetilde{C}_{ijkl}/(\widetilde{R}\widetilde{T}\tilde{c}_{max})$ and the dimensionless space with $\mathbf{x} = \tilde{\mathbf{x}}/\widetilde{L}_0$, where $\widetilde{L}_0$ is the characteristic length scale, $\widetilde{R}$ the gas constant, $\widetilde{T}$ absolute temperature and $\tilde{c}_{max}$ the solubility limit for lithium ions. The governing equations in dimensionless form are

then

$$\sigma_{ij,j} = 0 \quad \text{in } B, \tag{2.71}$$

$$u_i = \bar{u}_i \quad \text{on } \partial B_u, \tag{2.72}$$

$$\sigma_{ij} n_j = \bar{t}_i \quad \text{on } \partial B_\sigma, \tag{2.73}$$

and the equilibrium condition is written in the dimensionless weak form by multiplication with the test function η_i and integrating over the volume $\mathcal{B}$ as

$$-\int_{\mathcal{B}} \eta_{i,j} \sigma_{ij} \mathrm{d}V = 0. \tag{2.74}$$

The element-wise interpolations of the test function and its gradient are

$$\eta_i = \sum_I N^I \eta_i^I, \quad \eta_{i,j} = \sum_I N^I_{,j} \eta_i^I, \tag{2.75}$$

where N^I is the shape function and η_i^I are the nodal values of the test function. The superscript I denotes the node number. By inserting equation 2.75 into the weak form formulation, the elemental residual is

$$R^I_{u_i} = -\int_{\mathcal{B}^E} N^I_{u,j} \sigma_{ij} \mathrm{d}V, \tag{2.76}$$

where N_u is the shape function for the displacement u_i. The non-zero component of the element stiffness matrix follows as

$$K^{IJ}_{u_i u_k} = -\int_{\mathcal{B}^E} N^I_{u,j} C_{ijkl} N^J_{u,l} \mathrm{d}V. \tag{2.77}$$

The configurational force is computed by first solving the differential equations for the elastic field. From this solution the Eshelby stress tensor can be computed. The configurational force balance in equation 2.53 is transformed to the weak form by first multiplying with a test form η employing the additive rule, integrating over the volume B and applying the divergence theorem [104]

$$-\int_{\mathcal{B}} \Sigma_{ij} \eta_{i,j} \mathrm{d}V + \int_{\mathcal{S}} \Sigma_{ij} n_j \eta_i \mathrm{d}S + \int_{\mathcal{B}} g_i \eta_j \mathrm{d}V = 0. \tag{2.78}$$

The nodal configurational forces on a node I are computed with the assembly operation $\bigcup$ over all adjacent elements n_{el}

$$G_i^I = \bigcup_{e=1}^{n_{el}} \int_{\mathcal{B}_e} \Sigma_{ij}^{ns} N^I_{,j} \mathrm{d}V. \tag{2.79}$$

The nodal forces in an arbitrary integration volume can then be calculated in the sum

$$F_i = -\sum_{I=1}^{n_{nod}} G_i^I. \tag{2.80}$$

The driving forces on a dislocation can then be found by choosing an appropriate integration volume including the dislocation core.

The finite element simulations are performed within the open source software MOOSE, where the here presented numerical model is implemented in the form of user elements [100].

2.5.3 Spurious stresses

Solving the boundary value problem in FEM, plastic incompatibilities can rise "spurious stresses" [52]. The origin is found in the integration order of the strain which is one order lower than the degree of freedom, the displacement. When an eigenstrain is defined on the dislocation gliding plane in the same integration order as the degree of freedom variable, this cannot be captured in the space of strain. The incompatibility will be compensated by originating spurious stresses at the element boundaries. Exemplarily, when the displacement variables are linear, the strain is piece-wise constant. An applied linear eigenstrain will lead to incompatibilities. Underintegrated elements can be utilized to approach this issue, for example 8 node hexaedrons with 1-IP point quadratur [52]. Spurious stresses will be eliminated as the sampling on a reduced number of integration points reduces the incompatibilities. However, the use of underintegrated elements may lead to the so called "hour-glass" effect. A more simple approach is to assure that the eigenstrain is calculated on the same integration order as the strain, resolving the incompatibility and preventing the origination of spurious stresses. This approach is more flexible as it is not restricted to simulation environments that support underintegrated elements. A demonstration for a dislocation is shown in figure 2.6. If the eigenstrain has the same order of magnitude, than the displacement variables, "spurious stresses" in σ_{12} emerging on the gliding plane where the eigenstrain is applied. Reducing the integration order for the eigenstrain eliminates these "spurius stresses".

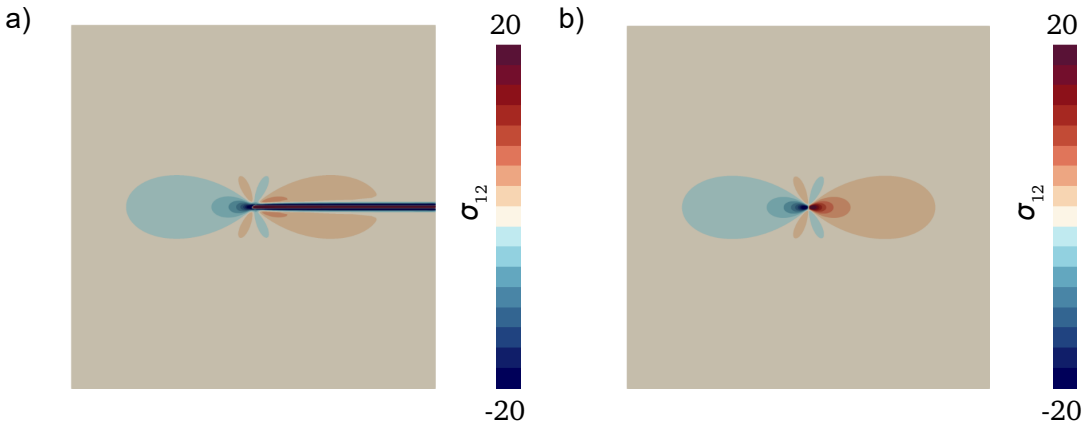

Figure 2.6: Stress field σ_{12} of an edge dislocation in the center of a finite volume with traction boundary conditions t_j applied on the outer boundaries. a) The dislocation eigenstrain has the same order of approximation as the displacements b) The order of approximation of the dislocation eigenstrain is one order lower than that of the displacement. Spurious stresses emerge if the eigenstrain has the same order of approximation as the displacements. The computation of the stress field can only be correct, when the eigenstrain has the same order of approximation as the strain.

2.5.4 Material properties of $LiMn_2O_4$

Spinel $LiMn_2O_4$ is a reasonably relevant cathode material and because of its isotropic properties an ideal candidate for a model material. As simplification, the isotropic lithium partial molar volume is given as $\widetilde{\Omega}_{ij} = \widetilde{\Omega}\delta_{ij}$ with the second order unit tensor as δ_{ij}. Note that the reference concentrations for the non-lithiated and fully lithiated state of $LiMn_2O_4$ in this work are defined at $c = 0$ and $c = 1$, respectively. The isotropic Young's modulus is measured as 93 GPa [4]. The structure of dislocations have not been analyzed in depth for $LiMn_2O_4$ but are confirmed for $LiMn_2O_3$ [70] and $LiMn_2O_4$ [105, 126], where structural defects were induced by means of ion irradiation. In the following analytical considerations show that a geometrical possible Burgers vector can be calculated, where the focus is on total dislocations and partial dislocations that include a stacking fault are neglected. According to Hornstra [47], the Burgers vector can be defined by the distance of two equivalent sites, e.g., two equivalent oxygen sites. The dislocation slip directions are in planes with the highest atom density. The structural similar Spinel has the highest density plane of oxygen in the (111) plane with slip directions in [110] [47]. The distance between two equivalent oxygen sites in the (111) plane for $LiMn_2O_4$ is $\tilde{a}_0\sqrt{2}/2$, with the lattice parameter $\tilde{a}_0$. The corresponding Burgers vector is $\tilde{a}_0/2[110]$ with the magnitude of $\tilde{b}_0 = \tilde{a}_0\sqrt{2}/2$. In an earlier experiment, a Burgers vector with similar length has been found for an edge dislocation in $LiMn_2O_4$ [126]. All material parameters applied in the model are summarized in table 2.1.

2.5.5 Benchmark for the elastic fields of dislocations

In this section the benchmarks for the stress field of an edge and a screw dislocation are shown as validation for the proposed numerical model. The straight edge dislocation is modeled as a plane strain problem in an elastic material. The anti plane strain problem is considered to model a straight screw dislocation. The mechanical properties defined for the benchmarks correspond to $LiMn_2O_4$ described in chapter 2.5.4.

A straight edge dislocation is modeled as a plane strain problem. The sample size for the simulation is $200\,\mathrm{nm} \times 200\,\mathrm{nm}$, and the mesh consists of 200×200 four-node quadrilateral elements. The dislocation with normalized Burgers vector $\mathbf{b} = [b_0, 0, 0]$ and normal vector $\mathbf{n} = [0, 1, 0]$ is placed at the center of the sample. To compare the numerical finite domain solution to the analytical infinite domain solution, the infinite domain is emulated by a traction boundary condition that cancels out the boundary effect. In particular the traction boundary condition is chosen in a way that defines a stress state on the outer boundary that

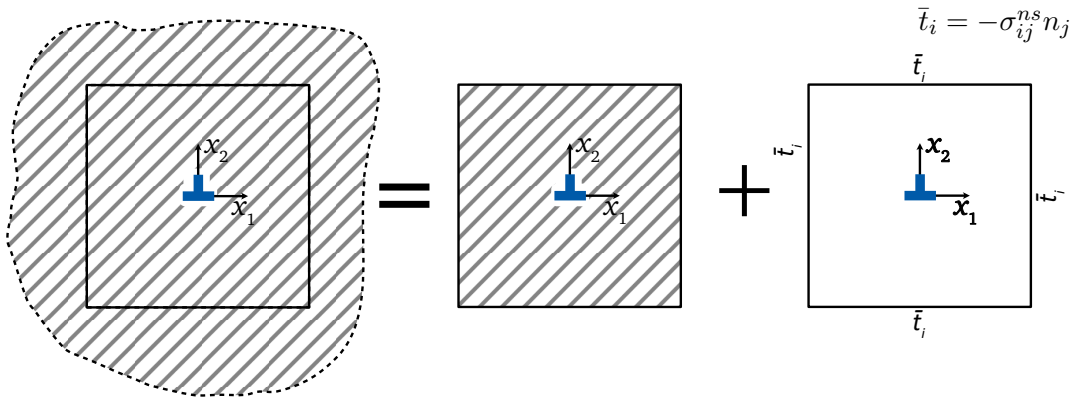

Figure 2.7: The solution for a dislocation on a finite domain has to satisfy the stress free boundary conditions which can be fulfilled by the addition of the stress fields of image dislocations and a correction stress field. To compute a numerical solution on a finite domain that is equivalent to the analytical solution on an infinite domain, traction boundary conditions have to be applied on the free surfaces of the finite domain. As indicated in the figure, the analytical solution from the infinite volume marked by the square can be recovered in the numerical solution when the traction boundary condition $\bar{t}_i$ defines a stress state of the analytical solution on the boundaries thus canceling out the boundary effect.

Table 2.1: General and specific parameters corresponding to spinel $LiMn_2O_4$.

Parameter	Symbol	Value
Gas constant	$\widetilde{R}$	$8.314\,462\,1\,\mathrm{J\,mol^{-1}\,K^{-1}}$
Absolute temperature	$\widetilde{T}$	$300\,\mathrm{K}$
Current density	$\tilde{i}_n$	$2\,\mathrm{A\,m^{-2}}$
Faraday constant	$\widetilde{F}$	$96.485\,336\,521\,\mathrm{C\,mol^{-1}}$
Young's modulus	$\widetilde{E}$	$93\,\mathrm{GPa}$ [4]
Poisson's ratio	ν	0.3 [4]
Lattice parameter	$\tilde{a} = \tilde{b} = \tilde{c}$	$0.820\,51\,\mathrm{nm}$ [105]
Burgers vector	$\tilde{b}_0$	$0.580\,19\,\mathrm{nm}$
Lithium partial molar volume	$\widetilde{\Omega}$	$3.497 \times 10^{-6}\,\mathrm{m^3\,mol^{-1}}$ [133]
Solubility limit	$\tilde{c}_{max}$	$2.29 \times 10^{4}\,\mathrm{mol\,m^{-3}}$ [133]
Interaction parameter	χ	1.0
Diffusion coefficient	$\widetilde{D}_0$	$7.08 \times 10^{-15}\,\mathrm{m^2\,s^{-1}}$ [133]
Stress-free concentration	$\tilde{c}_{ref}$	$1.145 \times 10^{3}\,\mathrm{mol\,m^{-3}}$

corresponds to the analytical solution as described in figure 2.7. The boundary condition is defined as

$$\bar{t}_i = \sigma_{ij}^{ns} n_j, \tag{2.81}$$

where σ_{ij}^{ns} is the non-singular analytical solution for the edge dislocation [12]. Note the difference to the construction of an image dislocation, where the stress field of a dislocation in an infinite body is corrected, such that it fulfills the traction free boundary condition on a surface close to the dislocation. For a more physical meaningful core energy, the core parameter h can be calibrated with a molecular dynamics simulation. In absence of that, the behavior of the solution with the h-variation is studied for better understanding. The variation of the stress field σ_{11} with the h-parameter is shown in figure 2.8a. The singular analytical solution is included as reference, marked by the black dashed line. The influence of the core width shows in the core region, as the maximum of the stress field increases with a smaller h-value, while the position of the maximum stress shifts towards a smaller distance from the core. The smoothness of the solution increases with the core width. The reason is that a constant mesh size was chosen for all simulations so that the ratio between mesh size and core width is in favour for the simulations with a larger core width. This is analyzed in the following by variation of the mesh size with a constant core width $h = 2$ in figure 2.8b. Exemplarily the stress field σ_{11} is shown for sizes of the mesh elements between $0.5h$ and $0.25h$. In the inset,

the mesh dependence of the numerical computed distribution function $\hat{W}$ is shown. The numerical distribution function is element-wise constant, and thus a step function. For a mesh size larger than the core width the distribution function is not accurate and with that the error in the computed stress fields is large. Exemplary for σ_{11} converging of the stress field between the mesh size of $0.5h$ and $0.25h$ indicates a sufficient mesh resolution. A mesh size of $0.5h$ is chosen as a compromise between an accurate solution for the stress field and computation efficiency. A detailed study of the non-zero stress fields of the edge dislocation is shown in figure 2.9 for a dislocation core width $h = 2$. As reference are the analytical singular and non-singular solutions [12] shown and the core width is indicated by a grey shaded area. The solutions for the stress fields σ_{11}, σ_{22} and σ_{33} are shown as line-plots along the x_2-axis and the stress field σ_{12} is shown along the x_1-axis. This is also indicated in the lower insets where the respective stress field distributions are shown. The numerical solution is between the singular and the non-singular analytical solution. The stress field outside the dislocation core region agrees well with both the singular and the non-singular analytical solution. The upper inset shows the variation of the stress field with the h-parameter.

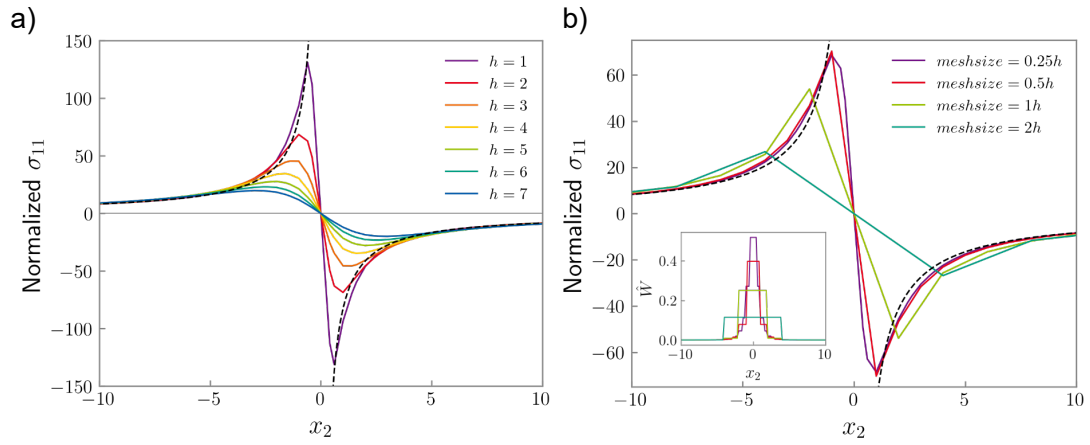

Figure 2.8: Benchmarks of the edge dislocation for the variation of the h parameter. a) The normalized stress field σ_{11} for different h parameter, compared to the analytical solution indicated with the black dashed line. b) The stress field σ_{11} is depicted for different mesh sizes. The inset shows the respective numerical distribution function $\hat{W}$.

In the following the benchmark for the screw dislocation is discussed. The size of the three dimensional sample for the simulation is $200\,\mathrm{nm} \times 200\,\mathrm{nm} \times 4\,\mathrm{nm}$, and the mesh

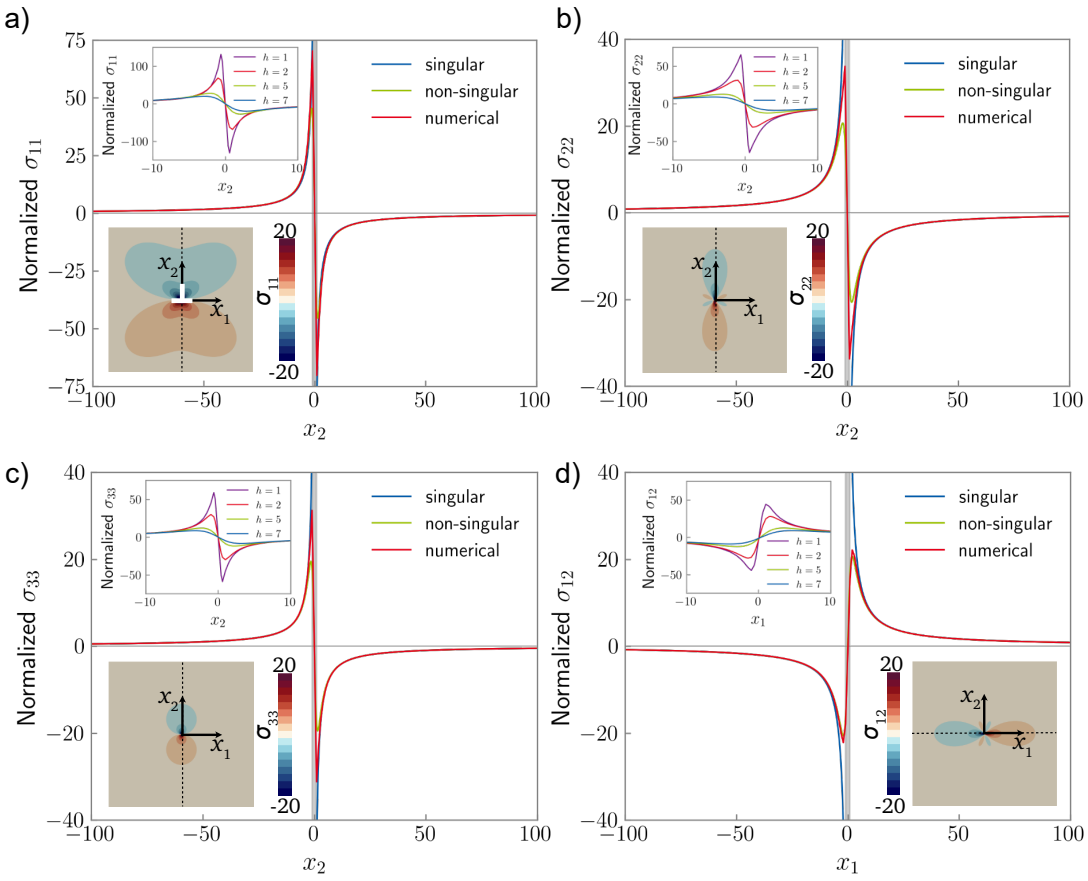

Figure 2.9: Benchmarks for the nonzero components of the stress field a) σ_{11}, b) σ_{22}, c) σ_{33} and d) σ_{12} of the edge dislocation. The numerical and analytical solutions [12] agree well outside the core region defined by the dislocation core width h marked by the shaded grey area.

consists of $200 \times 200 \times 4$ eight-node quadrilateral elements. The dislocation with Burgers vector $\mathbf{b} = [0, 0, b_0]$ and normal vector $\mathbf{n} = [0, 1, 0]$ is placed at the center of the sample. The outer boundaries of the sample with normal directions in the x_1, x_2, and x_3 direction are subject to the traction boundary condition to cancel out the boundary effect as before. The results for the non-zero stress fields of the screw dislocation are shown in figure 2.10 and the stress field outside the dislocation core region agrees well with both the classical (singular) and the non-singular analytical solution from Cai et al. [12].

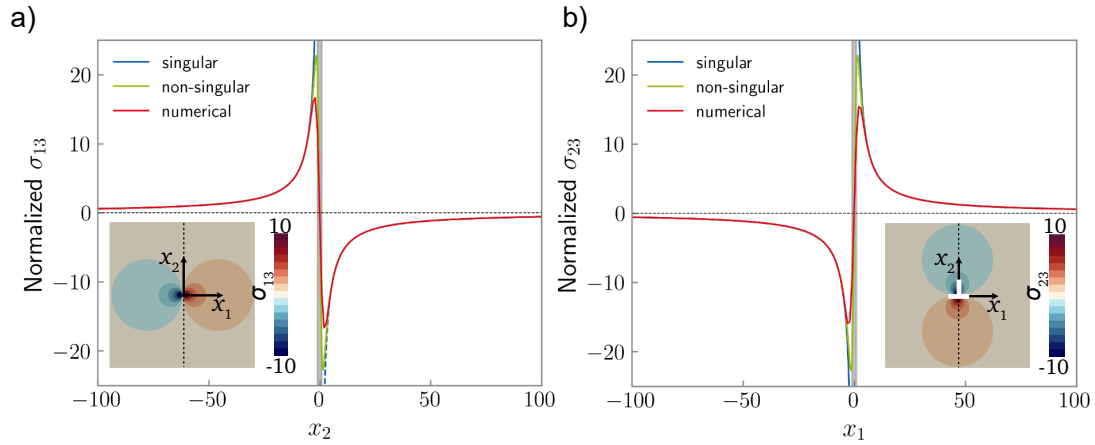

Figure 2.10: Benchmarks for the nonzero components of the stress field a) σ_{13} and b) σ_{23} of the screw dislocation. The numerical and analytical solutions [12] agree well outside the core region defined by the homogenization length h marked by the shaded grey area.

2.5.6 Benchmark for an edge dislocation within a particle under shear load

In this section the configurational force on a dislocation inside a particle subject to a shear load is compared to the analytical solution for the Peach-Koehler force. The dislocation with a normalized Burgers vector $b_0 = 1.033$ is placed in the center of a particle and the boundary condition on the free surfaces for the displacement is a shear load $\tau = 50$ as depicted in figure 2.11. The particle size is 50×50 nm^2 with 200×200 mesh elements. The benchmark is computed for different core parameters and elastic properties. For the isotropic case, the elastic properties of $LiMn_2O_4$ were applied as defined in chapter 2.5.4. The elastic properties for the anisotropic cases are defined in chapter 3.4.3, where LFP

stands for $LiFePO_4$ and FP is $FePO_4$. For LFP/FP the particle is defined containing two phases, where $FePO_4$ is in the upper half and $LiFePo_4$ is in the lower half of the particle. According to the Peach-Koehler formular, the driving force on the dislocation is then $F_1^{PK} = b\sigma_{12} = -51.65$ and $F_2^{PK} = 0$. The calculated and computed driving forces are summarized in table 2.2. Compared to the theoretical calculated value, the numerical computed driving force has a maximum difference of 1.3%. Overall, the driving forces for the isotropic and anisotropic cases agree well with a small dependence on the core parameter. The F_2 component of the numerical computed driving forces differs between the isotropic and anisotropic cases, but do not depend on the core parameter. While the isotropic case $F_2^{isotropic} = 2.94 \times 10^{-8}$ agrees well with the analytical solution, considering numerical error, the F_2 components for the anisotropic cases are nonzero. Specifically $F_2^{\text{FP}} = F_2^{\text{LFP}} = -30.934$ for the single phase materials and $F_2^{\text{LFP/FP}} = 18.31$ for the two phase material. The driving force points towards the tensile side of the dislocation for the

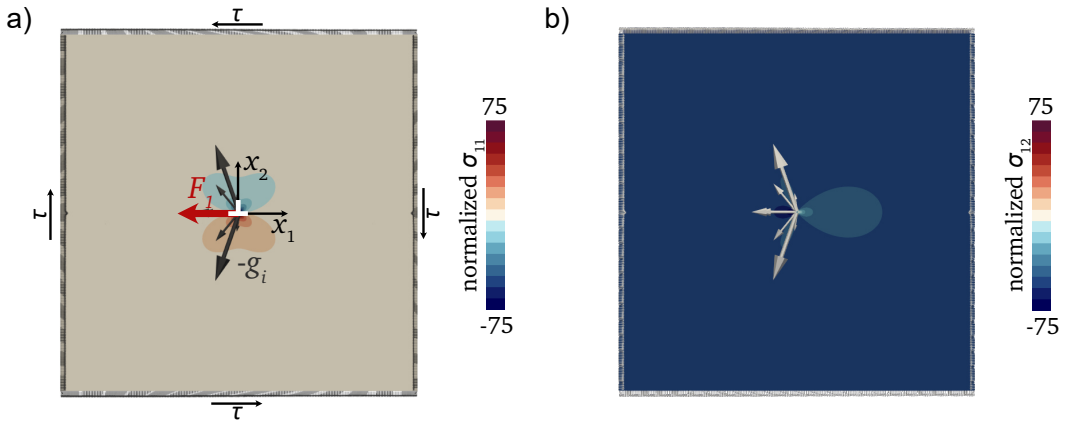

Figure 2.11: A particle with a dislocation is subject to a shear load $\tau = -50$. a) σ_{11} b) σ_{12}. The arrows represent the nodal configurational body forces.

Table 2.2: Benchmark for the Peach-Koehler force on a dislocation with normalized Burgers vector $b_0 = 1.033$ inside a particle subject to a shear $\tau = 50$. The difference between the numerical and theoretical value is calculated relative to the theoretical value for the driving force $F_1^{PK} = -51.65$.

	$h = 1.5$		$h = 2.0$		$h = 2.5$	
	F_1	Diff. [%]	F_1	Diff. [%]	F_1	Diff. [%]
Isotropic	52.28	1.2	51.57	0.2	51.38	0.5
FP	−52.27	1.2	51.56	0.2	51.37	0.5
LFP	−52.30	1.2	51.59	0.1	51.39	0.5
LFP/FP	−52.31	1.3	51.61	0.1	51.41	0.4

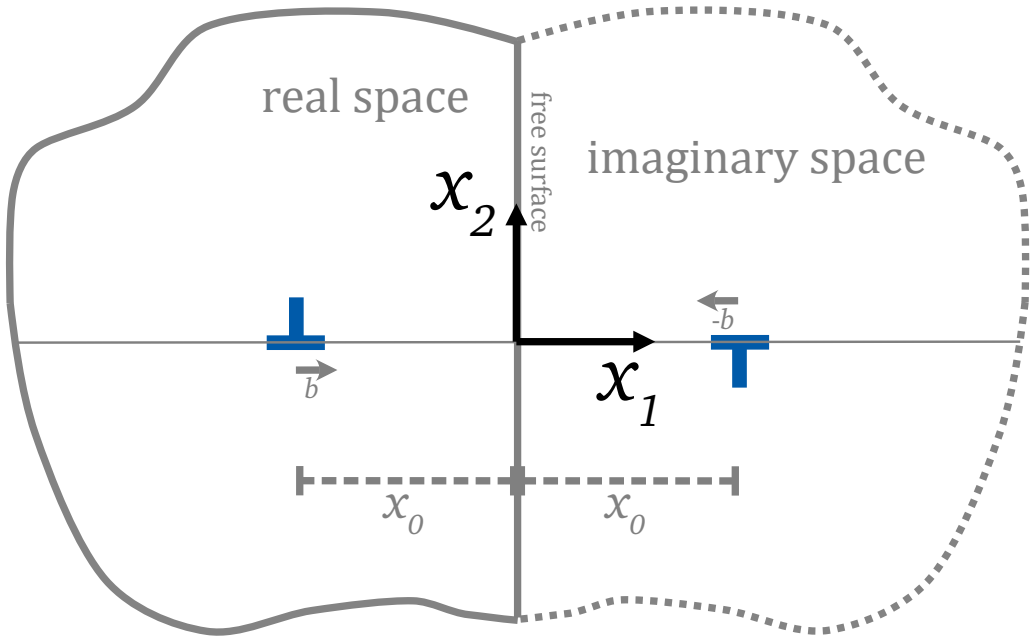

Figure 2.12: Construction of an image dislocation.

2.5.7 Benchmark for an edge dislocation close to a free surface

Dislocations close to free surfaces are subject to driving forces, caused by the so called image dislocations [13]. In short, an image dislocation is constructed to modify the stress field of the real dislocation, such that it fulfills the traction free boundary conditions at the surface. Then the modified stress field will raise driving forces on the real dislocation. For a screw dislocation the boundary conditions are fulfilled with the construction of the image dislocation, where for the case of an edge dislocation an additional correction stress field is necessary. Consider an edge dislocation with Burgers vector $b = b_0(100)$ and gliding plane normal vector $n = (010)$ placed in a distance $\tilde{x}_0$ to a traction free surface normal to the $\tilde{x}_1$ direction at $\tilde{x}_1 = 0$, as depicted in figure 2.12. The stress field of the dislocation has to satisfy the traction free boundary condition $\tilde{t}_i = 0$. A construction of a so called image dislocation with the Burgers vector $\tilde{b}^{img} = -\tilde{b}$ at position $\tilde{x}_1 = \tilde{x}_0$ reduces the stress field at the surface. With an additional correction stress field $\widetilde{\sigma}_{ij}^{corr}(\tilde{x}_1 = 0, \tilde{x}_2)$ the boundary condition is satisfied. The resulting stress is then described as

$$\widetilde{\sigma}_{ij}(\tilde{x}_1, \tilde{x}_2) = \widetilde{\sigma}_{ij}^{self}(\tilde{x}_1 + \tilde{x}_0, \tilde{x}_2) - \widetilde{\sigma}_{ij}^{img}(\tilde{x}_1 - \tilde{x}_0, \tilde{x}_2) + \widetilde{\sigma}_{ij}^{corr}(\tilde{x}_1, \tilde{x}_2), \tag{2.82}$$

where according to [13] the correction stress field is

$$\begin{aligned}
\widetilde{\sigma}_{11}^{corr} &= -\frac{\widetilde{G}\tilde{b}_1}{2\pi(1-\nu)}(4\tilde{x}_0\tilde{x}_1\tilde{x}_2)\frac{3(\tilde{x}_1-\tilde{x}_0)^2-\tilde{x}_2^2}{((\tilde{x}_1-\tilde{x}_0)^2+\tilde{x}_2^2)^3}, \\
\widetilde{\sigma}_{22}^{corr} &= \frac{\widetilde{G}\tilde{b}_1}{2\pi(1-\nu)}(4\tilde{x}_0\tilde{x}_2)\frac{(\tilde{x}_1-\tilde{x}_0)^2(\tilde{x}_1+2\tilde{x}_0)-(3\tilde{x}_1-2\tilde{x}_0)\tilde{x}_2^2}{((\tilde{x}_1-\tilde{x}_0)^2+\tilde{x}_2^2)^3}, \\
\widetilde{\sigma}_{12}^{corr} &= \frac{\widetilde{G}\tilde{b}_1}{2\pi(1-\nu)}(2\tilde{x}_0)\frac{(\tilde{x}_1-\tilde{x}_0)^3(\tilde{x}_1+\tilde{x}_0)-6\tilde{x}_1(\tilde{x}_1-\tilde{x}_0)\tilde{x}_2^2+\tilde{x}_2^4}{((\tilde{x}_1-\tilde{x}_0)^2+\tilde{x}_2^2)^3}.
\end{aligned} \tag{2.83}$$

The construction of the image dislocation and the correction stress field leads to driving forces on the real dislocation, than can be calculated by solving the Peach-Koehler equation at the position of the real dislocation, e.g. $\tilde{x}_1 = -\tilde{x}_0$. The driving force towards the free surface is defined as $\widetilde{F}_1 = \tilde{b}_1(\widetilde{\sigma}_{11} + \widetilde{\sigma}_{12} + \widetilde{\sigma}_{13})$. For the edge dislocation the shear stress component $\widetilde{\sigma}_{13} = 0$. Further at the position of the real dislocation $\widetilde{\sigma}_{11}^{corr}(\tilde{x}_1 = -\tilde{x}_0, \tilde{x}_2 = 0) = 0$. Thus only the $\widetilde{\sigma}_{12}^{img}$ component of the stress field contributes to the $\widetilde{F}_1$ component of the Peach-Koehler force and $\widetilde{F}_1 = \tilde{b}_1\widetilde{\sigma}_{12}^{img}$.

The Peach-Koehler force due to the image dislocation on the dislocation for the non-singular dislocation theory [12] is calculated in the following. It is shown that the correction stress

field does not contribute to the Peach-Koehler force, so the derivation is omitted here. As discussed above, the non-zero image dislocation stress fields contributing to the Peach-Koehler force of the real dislocation at position $(\tilde{x}_1 = -\tilde{x}_0, \tilde{x}_2 = 0)$ are the normal stress $\widetilde{\sigma}_{11}^{nonsi,img}$ and the shear stress $\widetilde{\sigma}_{12}^{nonsi,img}$. Considering $\tilde{b}^{img} = -\tilde{b}$, the stress fields of the image dislocation at position $(\tilde{x}_1 = \tilde{x}_0, \tilde{x}_2 = 0)$ follows from equation 2.29 as

$$\widetilde{\sigma}_{11}^{nonsi,img} = -\frac{\widetilde{G}\tilde{b}}{2\pi(1-\nu)}\frac{\tilde{x}_2}{\tilde{\rho}_h^2}\left(1 + \frac{2((\tilde{x}_1 - \tilde{x}_0)^2 + \tilde{h}^2)}{\tilde{\rho}_h^2}\right),$$

$$\widetilde{\sigma}_{12}^{nonsi,img} = \frac{\widetilde{G}\tilde{b}}{2\pi(1-\nu)}\frac{\tilde{x}_1 - \tilde{x}_0}{\tilde{\rho}_h^2}\left(1 - \frac{2\tilde{x}_2^2}{\tilde{\rho}_h^2}\right),$$

where $\tilde{\rho}_h = \sqrt{(\tilde{x}_1 - \tilde{x}_0)^2 + \tilde{x}_2^2 + \tilde{h}^2}$. As for the singular case, the resulting stress field defined by equation 2.82 is utilized to evaluate the stress field at the position of the real dislocation. It can be seen that $\widetilde{\sigma}_{11}^{nonsi}(\tilde{x}_1, \tilde{x}_2 = 0) = 0$, which means that the respective image dislocation stress field and correction stress fields have to be zero. This leaves the shear stress as the remaining contribution to the Peach-Koehler force. Comparing the stress fields of the real and the image dislocation shows that at the boundary and $\tilde{x_2} = 0$ the equality is $\widetilde{\sigma}_{12}^{nonsi,self}(\tilde{x}_1 = 0, \tilde{x}_2 = 0) = \widetilde{\sigma}_{12}^{nonsi,img}(\tilde{x}_1 = 0, \tilde{x}_2 = 0)$. This means that the resulting stress in equation 2.82 already satisfies the traction free boundary condition at this point when the stress field of the image dislocation is added and thus the correction stress field needs to be zero, e.g. $\widetilde{\sigma}_{12}^{nonsi,corr}(\tilde{x}_1 = 0, \tilde{x}_2 = 0)$. Then the non-singular Peach-Koehler force can be calculated from the image dislocation stress field with $\widetilde{F}_1^{nonsi} = \tilde{b}_1\widetilde{\sigma}_{12}^{nonsi,img}$.

In the following the analytical forms of the image stress field are utilized to calculate the Peach-Koehler forces on a dislocation close to an interface in an otherwise infinite medium. The material properties correspond to isotropic spinel $LiMn_2O_4$ as described in chapter 2.5.4. Numerical solutions with the non-singular dislocation model are computed for a dislocation in a finite but large particle. The non-coupled numerical example particle has the dimensions 1000×1000 nm^2 consisting of 500×500 mesh elements. The analysis is summarized in figure 2.13. The singular and non-singular Peach-Koehler-force agree perfectly outside the core region. Towards the free surface, the singular Peach-Koehler-force has a positive singularity, while the non-singular Peach-Koehler-force reduces to zero. The maximum of the non-singular Peach-Koehler-force is at a distance of $\tilde{h}/2$, which marks the position where the distance between the real and the image dislocation equals $\tilde{h}$. The numerically computed driving force agrees well with the non-singular solution. However, there are differences. Directly at the surface the numerical solution reaches

a small but non-zero value. This could be caused by a numerical error. The maximum driving force is found at a distance of $\tilde{h}$ to the free surface. This can be explained as the area within the core subject to the prescribed eigenstrain gradually moves out of the volume, once the distance to the free surface is smaller than the core radius, reducing the total distortion due to the dislocation.

The integral $\Delta\widetilde{W} = \int_0^{\tilde{x}_0} \widetilde{F}_1 d\tilde{x}_1$ defines the change of the system energy to introduce a dislocation from the free surface into the material. The calculation of $\Delta\widetilde{W}$ is discussed in detail in chapter 5 in figure 5.4. In order to obtain a physical reasonable value for the singular solution it is common to introduce a cut-off radius to deal with the infinite singular solution at the dislocation position. In this sense the contribution of the area within the dislocation core from the free surface can be removed from the evaluation of the image forces, as adapted for the singular case in figure 2.13b. The change of the system energy for all three solutions shows a similar trend but the numerical solution shows deviations of up to 50 percent relative to the analytical solutions. The slope of the singular and non-singular analytical solutions agree well with only minor deviations caused by the different solution in the core region.

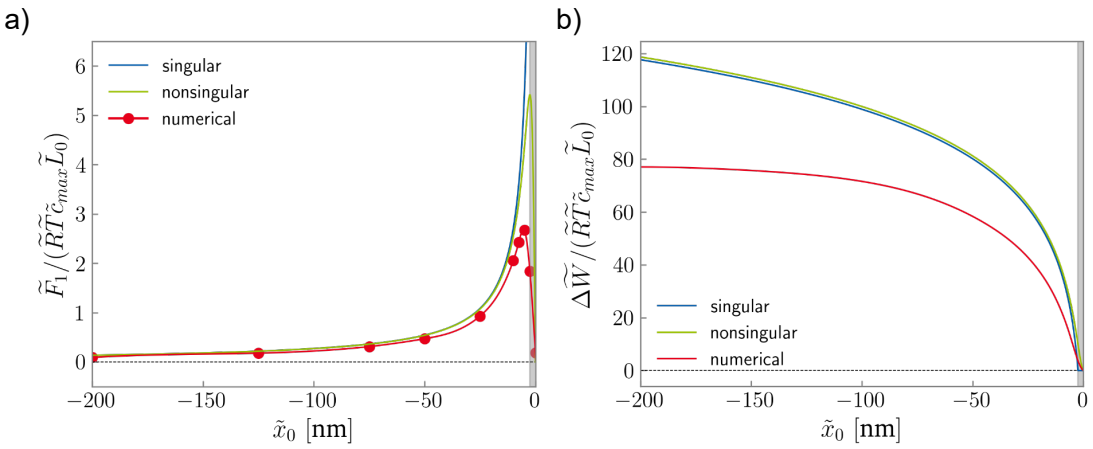

Figure 2.13: a) Image force calculated with the Peach-Koehler force from singular and non-singular stress fields and comparison to the numerical obtained configurational force. b) Work on the dislocation obtained from integration of the image force in a).

3 Chemo-mechanical Modeling and Simulation of Dislocated Solids

In this chapter the chemo-mechanical modeling and simulation of dislocated solids is described as depicted in figure 3.1. The fundamentals of diffusion are covered with the Fick's laws and the Cahn-Hilliard phase separation. The numerical non-singular dislocation model is coupled to a Cahn-Hilliard type phase field model via a stress term in the free energy density of diffusive ions. Then the configurational mechanics for dislocations in chemo-mechanical problems is formulated. The implementation into FEM is described, where the residuals and Jacobian matrix are derived and normalized to natural units. The numerical model is benchmarked by studying the mechanical influence on spinodal decomposition and the interface width and comparing the equilibrium ion concentration in the vicinity of an edge dislocation to the analytical solution. Then the material properties for $LiFePO_4$ are introduced which find application in the examples in this work considering anisotropic elastic properties and phase separation.

The mechanically coupled dilute diffusion problem has been published in [103]. The derivation of the Eshelby stress tensor from the gradient of the free energy density follows the previous works [139, 138] and the extension to the configuration mechanics of dislocations in mechanically coupled phase transformation problems has been published in [140].

3.1 Fundamentals of Diffusion

3.1.1 Diffusion: Fick's laws

In the following the equations describing diffusion are presented in the form of Fick's first and second law according to [84]. Fick's first law relates the Flux $\widetilde{J}_i$ to the concentration

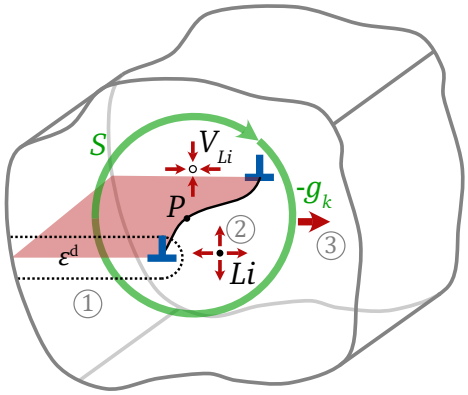

Figure 3.1: Chemo-mechanical coupled model for dislocated solids. 1) The dislocation is modeled as a non-singular eigenstrain distribution ε^D along the gliding plane. 2) The strain of intercalated ions interacts with the dislocation elastic field. The chemistry of the intercalated lithium ions Li and respective vacancies V_{Li} are described in a phase field model with the stress field contributing to the free energy density of the ion phase field. 3) By integration along the closed path S the configurational forces $-g_k$ give the driving forces on the dislocation.

gradient $\tilde{c}_{,j}$ as

$$\widetilde{J}_i = -\widetilde{D}_{ij}\tilde{c}_{,j}. \tag{3.1}$$

In the general case the diffusion constant $\widetilde{D}_{ij}$ is a tensor defined as

$$\widetilde{D}_{ij} = \begin{pmatrix} \widetilde{D}_{11} & 0 & 0 \\ 0 & \widetilde{D}_{22} & 0 \\ 0 & 0 & \widetilde{D}_{33} \end{pmatrix}, \tag{3.2}$$

that can be reduced to an isotropic constant $\widetilde{D}$ when $\widetilde{D}_{11} = \widetilde{D}_{22} = \widetilde{D}_{33}$. The continuity equation states that the in- and outflux of a volume element is the change in the concentration over time

$$-\widetilde{J}_{i,i} = \dot{\tilde{c}}, \tag{3.3}$$

which assumes that there are no sinks or sources for the diffusive species within the volume element. Combining equation 3.1 and 3.3 leads to the diffusion equation or Fick's second law

$$\dot{\tilde{c}} = \left(\widetilde{D}_{ij}\tilde{c}_{,j}\right)_{,j}. \tag{3.4}$$

3.1.2 Phase Separation: Cahn-Hilliard Equation

The Cahn-Hilliard equation describes diffusion as an evolving field for the distribution of diffusive species. The theory behind the Cahn-Hilliard equation is described in [11, 10]. Considered is the diffusion of ions in a host material, where species A corresponds to the diffusive ions and species B to the according vacancies. The total number of diffusive species is then $N = n_A + n_B$. The mixing entropy $\widetilde{S}$ of such a system is then

$$\widetilde{S} = \tilde{k}_B \ln(\Gamma), \tag{3.5}$$

where the total number of states $\Gamma = N!/(n_A!n_B!)$. The Stirling's approximation [64] allows to simplify the mixing entropy with $a! \simeq a\ln(a) - a$, where higher order terms are neglected, to

$$\widetilde{S} = \tilde{k}_B \left[N\ln(N) - N - (n_A\ln(n_A) - n_A) - ((N-n_A)\ln(N-n_A) - (N-n_A))\right], \tag{3.6}$$

which reduces to

$$\widetilde{S} = -N\tilde{k}_B \left[\left(\frac{n_A}{N}\right)\ln\left(\frac{n_A}{N}\right) + \left(1-\frac{n_A}{N}\right)\ln\left(1-\frac{n_A}{N}\right)\right]. \tag{3.7}$$

Then a concentration $\tilde{c} = n_A/(\widetilde{N}_A\widetilde{V}_m)$ that can reach the maximum concentration $\tilde{c}_{max} = N/(\widetilde{N}_A\widetilde{V}_m)$ is defined, where $\widetilde{N}_A$ is the Avogadro constant and $\widetilde{V}_m$ is the molar volume. This leads to the molar mixing entropy

$$\widetilde{S}_m = -\tilde{c}_{max}\widetilde{R}\widetilde{V}_m \left[(c)\ln(c) + (1-c)\ln(1-c)\right], \tag{3.8}$$

where the normalized concentration is $c = \tilde{c}/\tilde{c}_{max}$ and the gas constant $\widetilde{R} = \widetilde{N}_A\tilde{k}_B$. The molar free energy is

$$\widetilde{G}_m = \widetilde{U}_m - \widetilde{T}\widetilde{S}_m, \tag{3.9}$$

where $\widetilde{T}$ is the temperature and a regular solution model [36] is utilized to define the molar interaction energy $\widetilde{U}_m = \widetilde{R}\widetilde{T}\chi\widetilde{V}_m c(1-c)$ with the dimensionless interaction parameter χ. Then the chemical free energy density can be defined as

$$\tilde{f}^C = \frac{\widetilde{G}_m}{\widetilde{V}_m} = \tilde{c}_{max}\widetilde{R}\widetilde{T}\left[\chi(c)(1-c) + (c\ln(c) + (1-c)\ln(1-c))\right]. \tag{3.10}$$

The free energy density describes a mixing behavior when the interaction parameter $\chi < 2.5$ and a non-mixing behavior for $\chi \geq 2.5$, as described in figure 3.2a. In the latter case, the system tends to form two separated phases with a low concentration phase and a high concentration phase, respectively. An interface will form between the two separated phases and its interface tension contributes to the free energy density as

$$\tilde{f}^i = \frac{1}{2}\tilde{\kappa}c_{,i}^2. \tag{3.11}$$

The interface position is found by the local concentration gradient and the interface parameter $\tilde{\kappa}$ defines its width, where a small $\tilde{\kappa}$ leads to a wide interface and a large $\tilde{\kappa}$ leads to a thin interface. The thickness of the interface shown in figure 3.2b can be calculated as

$$\tilde{s} = \frac{\delta c}{\tan\theta} = (c_\beta - c_\alpha)\sqrt{\frac{\widetilde{\kappa}}{2\Delta\tilde{f}^C}} \tag{3.12}$$

where c_β and c_α are the concentrations at the local minima, $\Delta\tilde{f}^C$ is the energy barrier which can be calculated in a simplification as $\Delta\tilde{f}^C = \tilde{f}^C_{max} - \tilde{f}^C_{min}$. For the ideal, symmetric case, $\tilde{f}^C_{max}$ is the local maximum at $c = 0.5$ and $\tilde{f}^C_{min}$ is equal for either of the two minima. The total free energy density $\tilde{f}$ is consequently

$$\tilde{f} = \tilde{f}^C + \tilde{f}^I. \tag{3.13}$$

The gradient of the free energy density with respect to the concentration $\tilde{c}$ returns the chemical potential

$$\tilde{\mu} = \frac{\delta \tilde{f}}{\delta \tilde{c}} = \widetilde{RT}\left[\chi(1-2c) + \ln\left(\frac{c}{1-c}\right)\right] - \tilde{\kappa}\tilde{c}_{,jj}. \tag{3.14}$$

Following the approach described by Di Leo et al. [22], the concentration-dependent ionic flux is defined as

$$\widetilde{J}_i = -\tilde{M}\tilde{\mu}_{,i} = -\frac{\widetilde{D}\tilde{c}_{max}}{\widetilde{RT}} c(1-c)\tilde{\mu}_{,i}, \tag{3.15}$$

which is equivalent to Fick's first law and $\tilde{M} = \widetilde{D}\tilde{c}_{max}c(1-c)/(\widetilde{RT})$ is the mobility. The Cahn-Hilliard equation is

$$\dot{\tilde{c}} = -\widetilde{J}_{i,i} = (\tilde{M}\tilde{\mu}_{,i})_{,j}, \tag{3.16}$$

and is equivalent to Fick's second law.

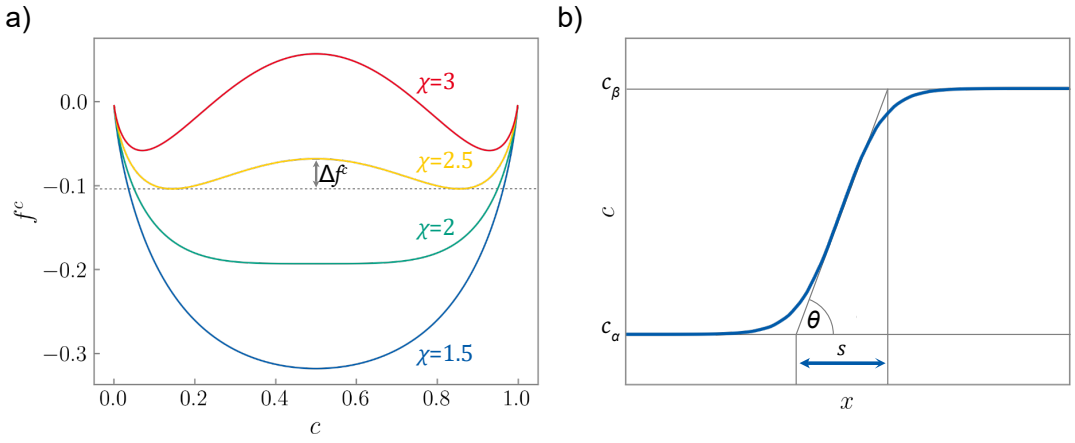

Figure 3.2: a) Normalized bulk free energy for different mixing behavior depending on the parameter χ. b) Cross section of the interface between the low and high concentration phase for the non-mixing behavior and definition of the interface thickness.

3.2 Mechanically Coupled Diffusion Model

The chemo-elastic model is based on the conventional Cahn-Hilliard phase-field model. A free energy functional is formulated including the contribution from the chemical energy, an interface energy and the elastic energy as a function of the ion concentration in the host material. A chemical potential is derived and its gradient describes chemical and elastic driving forces for the diffusion of ions. The total free energy functional $\tilde{\mathcal{F}}$ of the system is

$$\tilde{\mathcal{F}} = \int_{\widetilde{V}} \tilde{f} \mathrm{d}\widetilde{V}. \tag{3.17}$$

Assuming a regular solution (see e.g. [36]), the bulk chemical free energy density $\tilde{f}$ can be described as a linear combination of the chemical energy density $\tilde{f}^C$, the interface energy density $\tilde{f}^I$ and the elastic energy density $\tilde{f}^E$

$$\tilde{f} = \tilde{f}^C + \tilde{f}^I + \tilde{f}^E. \tag{3.18}$$

The individual parts are formulated as functions of the concentration $c = \tilde{c}/\tilde{c}_{max}$, which is normalized by the maximum concentration $\tilde{c}_{max}$, so that

$$\tilde{f}^C = \widetilde{R}\widetilde{T}\tilde{c}_{max}[c \ln c + (1-c)\ln(1-c) + \chi c(1-c)], \tag{3.19}$$

$$\tilde{f}^I = \frac{1}{2} c_{max} \widetilde{\kappa} c_{,j} c_{,j}, \tag{3.20}$$

$$\tilde{f}^E = \frac{1}{2} \widetilde{\sigma}_{ij} \left(\varepsilon_{ij} - \varepsilon^D_{ij} - \varepsilon^C_{ij} \right), \tag{3.21}$$

where the elastic energy density $\tilde{f}^E$ is formulated based on the Khachaturyan model [54]. Further χ is a dimensionless parameter describing non-ideal ion-ion interaction, $\widetilde{R}$ is the gas constant, $\widetilde{T}$ is the absolute temperature and $\widetilde{\kappa}$ is the interface energy coefficient. The strain field caused by the dislocation ε^D_{ij} is discussed in chapter 2.4. The lattice strain due to ion intercalation $\varepsilon^C_{ij} = [\tilde{c} - \tilde{c}_{ref}]\, \widetilde{\Omega}_{ij}/3$ is related to the partial molar volume $\widetilde{\Omega}_{ij}$ of diffusive ions in the host material [102, 15], where $\tilde{c}_{ref}$ is the stress-free concentration state in the reference material. In fact this is a linear approximation for the lattice strain due to the phase transformation upon ion intercalation between the non-intercalated state and the fully intercalated state, which are characterized by the reference concentrations at the two minima in the chemical free energy density in equation 3.19. Therefore $\widetilde{\Omega}_{ii}$ can directly take the value of the misfit strain. The linear constitutive relation between

stress and strain in equation 2.58 is then transformed to

$$\widetilde{\sigma}_{ij} = \frac{\partial \tilde{f}}{\partial \varepsilon_{ij}} = \widetilde{C}_{ijkl}\varepsilon^E_{kl} = \widetilde{C}_{ijkl}\left(\varepsilon_{kl} - \varepsilon^D_{kl} - \varepsilon^C_{kl}\right), \tag{3.22}$$

where the stress tensor is considered as concentration dependent $\widetilde{C}_{ijkl} = \widetilde{C}_{ijkl}(c)$. In this work two types of material are applied, where the stress tensor of $LiMn_2O_4$ described in chapter 2.5.4 is considered as independent on the concentration and the stress tensor of $LiFePO_4$ described in chapter 3.4.3 is considered as concentration dependent. Consequently the derivative of the stress tensor of $LiMn_2O_4$ with respect to the concentration will be $\partial \widetilde{C}^{\text{LMO}}_{ijkl}/\partial \tilde{c} = 0$ and the following equations will simplify accordingly. The evolution of the concentration follows the mass conservation law

$$\dot{\tilde{c}} + \widetilde{J}_{i,i} = 0 \quad \text{in } B, \tag{3.23}$$

with $\dot{\tilde{c}}$ being the time derivative of the concentration and the concentration dependent ion flux $\widetilde{J}_i$ is [22]

$$\widetilde{J}_i = -\tilde{M}\tilde{\mu}_{,i}. \tag{3.24}$$

The variational derivative of the free energy functional gives then the chemical potential

$$\tilde{\mu} = \frac{\delta \tilde{\mathcal{F}}}{\delta \tilde{c}} = \tilde{\mu}^0 - \tilde{\kappa} c_{,jj}, \tag{3.25}$$

where the homogeneous chemical potential $\tilde{\mu}^0$ is defined as

$$\tilde{\mu}^0 = \frac{\partial \tilde{f}}{\partial \tilde{c}} = \widetilde{R}\widetilde{T}\left[\chi(1-2c) + \ln\left(\frac{c}{1-c}\right)\right] - \frac{1}{3}\widetilde{\sigma}_{ij}\widetilde{\Omega}_{ij} + \frac{1}{2}\frac{\partial \widetilde{C}_{ijkl}}{\partial \tilde{c}}\varepsilon^E_{ij}\varepsilon^E_{kl}. \tag{3.26}$$

The elastic contribution to the free energy density translates in two terms in the chemical potential related to the stress tensor and the gradient of the elasticity tensor providing an additional driving force on diffusive ions. Thus the ions will not only follow the concentration field but also the stress field will influence the ion flux and the ion equilibrium concentration. The elastic contribution in $\tilde{\mu}^0$ to the driving force is also known as the inhomogeneity force [81]. Further the diffusion of ions is accompanied by a volume change, which will act as a diffusion induced stress implemented in the form of the elastic strain ε^E in equation 3.22. Eventually a two way coupling between the mechanical and chemical model is accomplished. The mobility of diffusive ions $\tilde{M}$ is related to the diffusion constant $\widetilde{D}_0$ with

$$\tilde{M} = \frac{\widetilde{D}_0}{\partial^2 \tilde{f}/\partial \tilde{c}^2} = \frac{\widetilde{D}_0 \tilde{c}_{max}}{\widetilde{R}\widetilde{T}[\frac{1}{c(1-c)} - 2\chi] + \frac{1}{9}\tilde{c}_{max}\widetilde{C}_{ijkl}\widetilde{\Omega}_{ij}\widetilde{\Omega}_{kl}}. \tag{3.27}$$

In the derivation, the chemical bulk free energy of a regular solution is considered, instead of an ideal solution. This introduces the additional term related to χ characterizing the mixing heat, which is often not regarded in the literature. With the given constant, the term related to the diffusion induced stress $\tilde{c}_{max}\widetilde{C}_{ijkl}\widetilde{\Omega}_{ij}\widetilde{\Omega}_{kl}/9$ is positive. Given $\chi = 1$ the above equation shows that ignoring χ leads to an underestimation of the stress effect on the mobility. Note that Vasconcelos et al. [122] has reported recently that ignoring the activity coefficient, which is related to both the mixing heat and the excess entropy, results in an overestimation of the stress effect on the mobility. It may imply that the excess entropy and the mixing heat play competing roles in determining mobility. Numerical examples on this topic are discussed in detail in chapter 4.2.1

The resulting governing equation for the stress dependent diffusion problem is

$$\dot{\tilde{c}} - \left(\tilde{M}\tilde{\mu}_{,i}\right)_{,i} = 0 \quad \text{in } B, \tag{3.28}$$

with the boundary conditions for the diffusion problem as

$$\tilde{c} = \tilde{c}_0 \quad \text{on } \partial B_c, \tag{3.29}$$

$$\widetilde{J}_i n_i = -\frac{\tilde{\tilde{i}}_n}{\widetilde{F}} = -\tilde{j}_0 \quad \text{on } \partial B_J. \tag{3.30}$$

Here $\tilde{\tilde{i}}_n$ is the applied current density, $\tilde{j}_0$ the applied flux on the boundary and $\widetilde{F}$ the Faraday's constant. The applied current density on the boundary in the simulation refers to the average of the total integral of the current density in the material measured experimentally. Furthermore the partial boundaries are defined such that $\partial B = \partial B_c \cup \partial B_J$ and $\partial B_c \cap \partial B_J = 0$ so that the partial boundaries fully enclose the volume B without overlap.

Inserting 3.25 into 3.28, one obtains the mechanically coupled diffusion equation which is a 4th order differential equation. A standard weak formulation of using the concentration c and the displacement u_i as independent field variables would require higher order elements in the FEM [112]. To avoid this, the coupled diffusion equation is solved by using a mixed finite element formulation, where both the concentration c and the chemical potential μ are treated as separate degrees of freedom [33]. By doing so, the original 4th order differential equation can be replaced by two lower order equations 3.25 and 3.28. Then the conventional linear finite elements can be applied to solve the two equations.

3.3 Configurational Mechanics of Dislocations in Chemo-mechanical Problems

In this work the theory of configurational forces is utilized to obtain the driving forces on dislocations interacting with intercalated ions. The configurational mechanics for dislocations in chemo-mechanical problems is proposed as an extension of a previous work on the configurational mechanics of dislocations in linear elasticity [139]. The starting point for the derivation of the Eshelby stress tensor and the configurational force balance is the gradient of the free energy density [24, 62]. With the principles in the previous works [139, 138] the Eshelby stress tensor is derived from the gradient of the total free energy density $\tilde{f}$ for mechanical coupled diffusion problems.

Following equation 3.18 the total free energy density $\tilde{f}$ can be represented as a function of the concentration $\tilde{c}$, the gradient of the normalized concentration $c_{,j}$, the total strain ε_{ij}, and the eigenstrain of the dislocation ε^D_{ij}

$$\tilde{f} = \tilde{f}(\tilde{c}, \nabla c, \boldsymbol{\varepsilon}, \boldsymbol{\varepsilon}^D). \tag{3.31}$$

The gradient is accordingly

$$\begin{aligned} \tilde{f}_{,k} &= \frac{\partial \tilde{f}}{\partial \tilde{c}} \tilde{c}_{,k} + \frac{\partial \tilde{f}}{\partial c_{,j}} c_{,jk} + \frac{\partial \tilde{f}}{\partial \varepsilon_{ij}} \varepsilon_{ij,k} + \frac{\partial \tilde{f}}{\partial \varepsilon^D_{ij}} \varepsilon^D_{ij,k} \\ &= \tilde{\mu}^0 \tilde{c}_{,k} + \tilde{c}_{max} \tilde{\kappa} c_{,j} c_{,jk} + \widetilde{\sigma}_{ij} (\beta_{ij,k} - \beta^D_{ij,k}). \end{aligned} \tag{3.32}$$

Here the symmetry of the stress tensor is considered to replace the gradient of the total strain ε_{ij} and eigenstrain strain ε^D_{ij} with the displacement gradient (total distortion) $\beta_{ij} = \tilde{u}_{i,j}$ and plastic distortion β^D_{ij}, respectively. Utilizing the definition of the chemical potential in equation 3.25 and the normalized concentration in equation. 3.39, the first two terms of the free energy density gradient can be further derived as

$$\tilde{\mu}^0 \tilde{c}_{,k} + \tilde{c}_{max} \tilde{\kappa} c_{,j} c_{,jk} = (\tilde{\mu} \tilde{c})_{,k} - \tilde{\mu}_{,k} \tilde{c} + (\tilde{c}_{max} \tilde{\kappa} c_{,j} c_{,k})_{,j}. \tag{3.33}$$

Utilizing the stress equilibrium condition 2.57 and the dislocation density tensor 2.49 as proposed by Lazar et al. [2, 62], leads to

$$\begin{aligned} \widetilde{\sigma}_{ij} (\beta_{ij,k} - \beta^D_{ij,k}) &= \widetilde{\sigma}_{ij} (\beta_{ik,j} - \beta^D_{ik,j}) - \widetilde{\sigma}_{ij} (\beta^D_{ij,k} - \beta^D_{ik,j}) \\ &= [\widetilde{\sigma}_{ij} (\beta_{ik} - \beta^D_{ik})]_{,j} - \widetilde{\sigma}_{ij,j} (\beta_{ik} - \beta^D_{ik}) + \widetilde{\sigma}_{ij} \epsilon_{kjl} \alpha_{il} \\ &= [\widetilde{\sigma}_{ij} (\beta_{ik} - \beta^D_{ik})]_{,j} + \widetilde{\sigma}_{ij} \epsilon_{kjl} \alpha_{il}, \end{aligned} \tag{3.34}$$

where $\beta_{ij,k} = \tilde{u}_{i,jk} = \tilde{u}_{i,kj} = \beta_{ik,j}$ is considered. Then equation 3.33 and equation 3.34 are substituted into equation 3.32. Then with $\tilde{f}_{,k} = \tilde{f}_{,j}\delta_{kj}$ the equations are rearranged to the configurational force balance in its local form

$$\widetilde{\Sigma}_{kj,j} + \tilde{g}_k = 0 \quad \text{in } V, \tag{3.35}$$

where the Eshelby stress tensor is

$$\widetilde{\Sigma}_{kj} = (\tilde{f} - \tilde{\mu}\tilde{c})\delta_{kj} - \widetilde{\sigma}_{ij}(\beta_{ik} - \beta^D_{ik}) - \tilde{c}_{max}\tilde{\kappa}c_{,j}c_{,k}, \tag{3.36}$$

and the configurational force is

$$\tilde{g}_k = \tilde{\mu}_{,k}\tilde{c} - \widetilde{\sigma}_{ij}\epsilon_{kjl}\alpha_{il}. \tag{3.37}$$

The first term of the configurational force is the chemical contribution which agrees with the driving force for the motion of a grain boundary in ionic polycrystalline ceramics derived by Vikrand et al. [124]. Another similar formulation of the configurational force and the Eshelby stress tensor in the thermomechanical theory without dislocations can be found in ref. [37]. The second term is the contribution of the dislocation, which has been obtained in a previous work [139]. The driving force on the defect can then be computed by the volume integration of the divergence of the Eshelby stress tensor or the configurational force

$$\tilde{F}_k = \int_V \widetilde{\Sigma}_{kj,j}\mathrm{d}V = -\int_V \tilde{g}_k \mathrm{d}V. \tag{3.38}$$

Particular useful is the relation of the chemical potential gradient with the flux $\tilde{J}_k$ given as $\tilde{\mu}_{,k} = -\tilde{M}^{-1}\tilde{J}_k$, as followed from equation 3.24. In the equilibrium state, the flux is zero at every point, labeling the first term to be zero in the volume integration. Then the driving force on the dislocation is numerically computed by integrating the divergence of the Eshelby stress tensor over the volume. This is equivalent to the volume integral of the configurational force in the presence of both terms on the right hand side of equation 3.37 and therefore chemical and mechanical contributions to the driving force are included. In this work the focus is on the driving force on misfit dislocations and their size dependent stability at the phase boundary in two-phase particles. The influences of misfit dislocations on the chemical driving force and phase transformation are topics for further studies in the future.

3.4 Implementation in the Finite Element Method

In this section the chemo-mechanical model introduced in the previous section is implemented into FEM. The FEM is applied to solve partial differential equations appoximatively. The simulation space is discretized into elements, on which the PDE is solved. In the first part of this section the variables are normalized to the natural units. In the second part the derivation of the residuals and the stiffness matrix for the implementation in the FEM formulation is shown. Note that the dimensionless form of the governing equations are employed. In conclusion, a series of examples is shown as benchmarks.

3.4.1 Normalization

A wide range of the order of magnitude in the model can cause inaccuracies during computation due to rounding errors. In particular, the order of magnitude of a typical elasticity tensor is in the range 10^9 and that of a concentration in the range 10^{-3}. A simple mean to this issue is to normalize the variables by scaling to the natural units. The normalization procedure is defined in the following section. The dimensionless concentration and molar volume are

$$c = \tilde{c}/\tilde{c}_{max}, \quad \Omega_{kj} = \tilde{c}_{max}\widetilde{\Omega}_{kj}. \tag{3.39}$$

The dimensionless chemical potential μ, mobility M, and stiffness tensor C_{ijkl} are defined with

$$\mu = \frac{\tilde{\mu}}{\widetilde{R}\widetilde{T}}, \quad M = \frac{\widetilde{R}\widetilde{T}}{\widetilde{D}_0\widetilde{c}_{max}}\tilde{M}, \quad C_{ijkl} = \frac{\widetilde{C}_{ijkl}}{\widetilde{R}\widetilde{T}\widetilde{c}_{max}}. \tag{3.40}$$

Defining the dimensionless space and time

$$\mathbf{x} = \frac{\tilde{\mathbf{x}}}{\widetilde{L}_0}, \quad t = \frac{\widetilde{D}_0}{\widetilde{L}_0^2}\tilde{t}, \tag{3.41}$$

where $\widetilde{L}_0$ is the characteristic length scale, allows to transform the temporal derivatives with

$$\frac{\partial}{\partial\tilde{t}} = \frac{\widetilde{D}_0}{\widetilde{L}_0^2}\frac{\partial}{\partial t}. \tag{3.42}$$

The governing equations in dimensionless form are then

$$\sigma_{ij,j} = 0 \quad \text{in } B, \tag{3.43}$$

$$\dot{c} - (M\mu_{,i})_{,i} = 0 \quad \text{in } B, \tag{3.44}$$

$$\mu = \chi(1-2c) + \ln\left(\frac{c}{1-c}\right) - \frac{1}{3}\sigma_{ij}\Omega_{ij} + \frac{1}{2}\frac{\partial C_{ijkl}}{\partial c}\varepsilon^E_{ij}\varepsilon^E_{kl} - \kappa c_{,jj} \quad \text{in } B, \tag{3.45}$$

$$u_i = \bar{u}_i \quad \text{on } \partial B_u, \tag{3.46}$$

$$\sigma_{ij}n_j = \bar{t}_i \quad \text{on } \partial B_\sigma, \tag{3.47}$$

$$c = c_0 \quad \text{on } \partial B_c, \tag{3.48}$$

$$J_i n_i = j_0 \quad \text{on } \partial B_J. \tag{3.49}$$

3.4.2 Finite element formulation

The governing equations are written in their dimensionless weak forms as

$$-\int_{\mathcal{B}} \eta_{i,j}\sigma_{ij}\mathrm{d}V = 0, \tag{3.50}$$

$$\int_{\mathcal{B}} (\eta\dot{c} - \eta_{,i}J_i)\mathrm{d}V = 0, \tag{3.51}$$

$$\int_{\mathcal{B}} \left\{ \eta \left[\mu - \chi(1-2c) - \ln\left(\frac{c}{1-c}\right) + \frac{1}{3}\sigma_{ij}\Omega_{ij} - \frac{1}{2}\frac{\partial C_{ijkl}}{\partial c}\varepsilon^E_{ij}\varepsilon^E_{kl} \right] - \eta_{,j}\kappa c_{,j} \right\} \mathrm{d}V = 0. \tag{3.52}$$

where η_i and $\eta_{i,j}$ are the test function and its gradient. The element-wise interpolations of the test function and its gradient are

$$\eta_i = \sum_I N^I \eta_i^I, \quad \eta_{i,j} = \sum_I N^I_{,j}\eta_i^I, \tag{3.53}$$

where N^I is the shape function and η_i^I are the nodal values of the test function and the superscript I denotes the node number. By inserting equation 3.53 into the weak form

formulations, the elemental residuals are

$$R^I_{u_i} = -\int_{\mathcal{B}^e} N^I_{u,j}\sigma_{ij}\mathrm{d}V, \tag{3.54}$$

$$R^I_c = \int_{\mathcal{B}^e} \left(N^I_c \dot{c} + N^I_{c,i} M \mu_{,i}\right) \mathrm{d}V, \tag{3.55}$$

$$R^I_\mu = \int_{\mathcal{B}^e} \left\{ N^I_\mu \left[\mu - \chi(1-2c) - \ln\left(\frac{c}{1-c}\right) + \frac{1}{3}\sigma_{ij}\Omega_{ij} - \frac{1}{2}\frac{\partial C_{ijkl}}{\partial c}\varepsilon^E_{ij}\varepsilon^E_{kl} \right] - N^I_{\mu,j}\kappa c_{,j} \right\} \mathrm{d}V, \tag{3.56}$$

where N_u, N_c, and N_μ are the shape functions for the variables u_i, c, and μ, respectively. The non-zero components of the element stiffness matrix are

$$K^{IJ}_{u_i u_k} = -\int_{\mathcal{B}^e} N^I_{u,j} C_{ijkl} N^J_{u,l}\mathrm{d}V, \tag{3.57}$$

$$K^{IJ}_{u_i c} = \frac{1}{3}\int_{\mathcal{B}^e} N^I_{u,j} C_{ijkl}\Omega_{kl} N^J_c \mathrm{d}V, \tag{3.58}$$

$$K^{IJ}_{cc} = \int_{\mathcal{B}^e} \frac{\partial M}{\partial c} N^I_{c,i}\mu_{,i} N^J_c \mathrm{d}V, \tag{3.59}$$

$$K^{IJ}_{c\mu} = \int_{\mathcal{B}^e} N^I_{c,i} M N^J_{\mu,i}\mathrm{d}V, \tag{3.60}$$

$$K^{IJ}_{\mu u_k} = \frac{1}{3}\int_{\mathcal{B}^e} N^I_\mu C_{ijkl}\Omega_{ij} N^J_{u,l}\mathrm{d}V, \tag{3.61}$$

$$K^{IJ}_{\mu c} = \int_{\mathcal{B}^e} \left\{ N^I_\mu \left[2\chi - \frac{1}{c(1-c)} + \frac{1}{9} C_{ijkl}\Omega_{ij}\Omega_{kl} \right] N^J_c - N^I_{\mu,j}\kappa N^J_{c,j} \right\} \mathrm{d}V, \tag{3.62}$$

$$K^{IJ}_{\mu\mu} = \int_{\mathcal{B}^e} N^I_\mu N^J_\mu \mathrm{d}V, \tag{3.63}$$

where the mobility gradient is

$$\frac{\partial M}{\partial c} = \frac{(1-2c)}{[1 - c(1-c)(2\chi - C_{ijkl}\Omega_{ij}\Omega_{kl}/9)]^2}. \tag{3.64}$$

The nonzero component of the damping matrix is

$$D^{IJ}_{cc} = \frac{1}{\Delta t}\int_{\mathcal{B}^e} N^I_c N^J_c \mathrm{d}V. \tag{3.65}$$

The driving forces on the dislocation are found by computing the nodal configurational forces according to chapter 2.5.2 by utilization of the configurational mechanics of dislocations in chemo-mechanical problems described in chapter 3.3.

The finite element simulations are performed within the open source software MOOSE, where the here presented numerical model was implemented in the form of user elements [100].

3.4.3 Material properties of $LiFePO_4$

$LiFePo_4$ (LFP) is an anisotropic lithium ion intercalation material with distinct differences in elasticity for the lithiated and non-lithiated phase. The material properties regarding diffusion and elasticity of $LiFePO_4$ are listed in table 3.1. The orthotropic elastic stiffness tensor of the LFP and the $FePO_4$ (FP) phases are taken from first principle calculation results from ref. [82], where the GGA+U case was adopted. The remaining material properties were taken from refs. [129, 117]. The anisotropic misfit strain due to the lattice mismatch between the LFP and the FP phase are $\varepsilon_{[100]} = 5\%$, $\varepsilon_{[010]} = 3.6\%$, and $\varepsilon_{[001]} = -1.9\%$ [117]. The diagonal components of the partial molar volume are then defined as $\Omega_{11} = 3\varepsilon_{[100]}$, $\Omega_{22} = 3\varepsilon_{[010]}$, $\Omega_{33} = 3\varepsilon_{[001]}$. The non-diagonal components of the partial molar volume are zero. Note that the value of Ω_{ii} should be depending on the value of $\tilde{c}_{ref}$.

To adopt the model to the non-homogeneous elasticity, the phase dependent stiffness tensor $\widetilde{C}_{ijkl}(c) = c\widetilde{C}^{\text{LFP}}_{ijkl} + (1-c)\widetilde{C}^{\text{FP}}_{ijkl}$ is defined, where $\widetilde{C}^{\text{LFP}}_{ijkl}$ and $\widetilde{C}^{\text{FP}}_{ijkl}$ correspond to the stiffness tensors of the LFP phase and the FP phase, respectively. The mobility is simplified as $\tilde{M} = \widetilde{D}\tilde{c}_{max}c(1-c)/(\widetilde{R}\widetilde{T})$ with the gradient $\partial\tilde{M}/\partial\tilde{c} = \widetilde{D}\tilde{c}_{max}(1-2c)$. It can be noted, that the part of this work utilizing the properties for the LFP two-phase material is focusing on the equilibrium state and dynamic effects play only a minor role.

3.4.4 Benchmark for the phase separation in isotropic solids

In the following the phase separation is numerically computed for lithium ions in spinel $LiMn_2O_4$ with and without contribution of the diffusion induced stress to the free energy density. The influence of the mechanical contribution on the interface is studied. The defined material properties are described in chapter 2.5.4. The parameter χ is related to ion-ion coupling and a value $\chi > 2.0$ leads to phase separation, where the phases are separated by an interface characterised by the interface parameter κ, as discussed

Table 3.1: General and specific parameters corresponding to $LiFePO_4$ [129, 117]. The stiffness tensor was calculated from first principles (GGA+U case) in [82]

Parameter	Symbol		Value
Gas constant	$\widetilde{R}$		$8.31\,\mathrm{J\,mol^{-1}\,K^{-1}}$
Absolute temperature	$\widetilde{T}$		$296\,\mathrm{K}$
Solubility limit	$\tilde{c}_{max}$		$21\,190\,\mathrm{mol\,m^{-3}}$
Interaction parameter	χ		3.56
Interface energy coefficient	$\tilde{c}_{max}\tilde{\kappa}$		$5 \times 10^{-10}\ \mathrm{J\,m^{-1}}$
Diffusion coefficient	$\widetilde{D}_0$		$7 \times 10^{-15}\ \mathrm{m^2\,s^{-1}}$
Stress-free concentration	$\tilde{c}_{ref}$		$0.03\tilde{c}_{max}$
		$FePO_4$	$LiFePO_4$
Stiffness tensor	$\widetilde{C}_{11}$	175.9 GPa	138.9 GPa
	$\widetilde{C}_{22}$	153.6 GPa	198.0 GPa
	$\widetilde{C}_{33}$	135.0 GPa	173.0 GPa
	$\widetilde{C}_{44}$	38.8 GPa	36.8 GPa
	$\widetilde{C}_{55}$	47.5 GPa	50.6 GPa
	$\widetilde{C}_{66}$	55.6 GPa	47.6 GPa
	$\widetilde{C}_{12}$	29.6 GPa	72.8 GPa
	$\widetilde{C}_{13}$	54.0 GPa	52.5 GPa
	$\widetilde{C}_{23}$	19.6 GPa	45.8 GPa

.

in chapter 3.1. When the definition for the mobility in equation 3.27 is applied, the mobility has singularities for $\chi \geq 2$. To avoid this, the mobility was simplified as $\tilde{M} = \widetilde{D}\tilde{c}_{max}c(1-c)/(\widetilde{R}\widetilde{T})$, where the gradient is $\partial\tilde{M}/\partial\tilde{c} = \widetilde{D}\tilde{c}_{max}(1-2c)$. More details on the topic are discussed in chapter 4.2.1. In the ideal, non-coupled case the interface width can be calculated with equation 3.12. By analyzing equation 3.10, for $\chi = 2.5$ the normalized free energy difference $\Delta f^C = 0.0359$ and the concentrations at the minima $c_\alpha = 0.145$ and $c_\beta = 0.855$ are obtained. Then the interface parameter was chosen as $\kappa = 5.0$ so that the theoretical interface thickness has a reasonable value, that is $\tilde{s} \approx 5.9$ nm.

In the following the influence of the stress field on the phase separation in a dislocation free sample, where the first example covers the decoupled case and the second covers the case with the full chemo-mechanical coupling. This allows to compare the chemo-mechanical coupled model to the well known spinodal decomposition governed by the Cahn-Hilliard equation and analyze the differences in the ion distribution and interface thickness. For both examples a sample size of $200\,\mathrm{nm} \times 200\,\mathrm{nm}$ with a mesh size of 200×200 is defined. The model is modified for the decoupled case to neglect the elastic part of the free energy density, e.g. $\tilde{f}^E = 0$, which is then equivalent to the Cahn-Hilliard equation. On all free surfaces traction free and flux free boundary conditions are defined. Initially a random concentration distribution between $0.45 < c(t=0) < 0.55$ was chosen. The simulation is conducted until a state close to the equilibrium is reached. The results for the concentration distribution of the decoupled case are shown in figure 3.3. An early stage featuring initial grains homogeneously nucleated over the sample is shown in figure 3.3a. A later stage close to the equilibrium is shown in figure 3.3b, where only a few large grains remain. Therefore the initial random structure transforms towards larger grains as would be expected from the spinodal decomposition. The interface thickness is measured across the grain boundary indicated by the white line in figure 3.3b. The concentration distribution along this line is shown in the inset. The concentration profile across the interface with the analysis of the interface thickness is shown in figure 3.5a. The measured interface thickness is close to the theoretical non-coupled value.

In the following the coupled case is presented, where the strain energy component of the bulk free energy is considered for the chemo-mechanical coupling. The geometry of the sample and the boundary and initial conditions is equal to that of the decoupled example. The results for the fully coupled case are shown in figure 3.4. In figure 3.4a the concentration distribution of an early stage where the initial grains are nucleated is shown. A later stage close to equilibrium is shown in figure 3.4b, where only a few large grains are left. In contrast to the non coupled case nucleation happens at the free surfaces and then the spinodal decomposition gradually evolves towards the center. The

interface thickness shows strong heterogeneity. More specifically, the interface is thin close to the free surfaces and widened in the center of the sample. The measured interface thickness at the free surfaces is slightly larger than in the decoupled case. The results for the concentration fields are complemented with the hydrostatic stress fields for the early stage in figure 3.4c and the late stage in figure 3.4d. The largest compressive stress fields are in the high concentration particles close to the interface and the largest tensile stressfields are in the low concentration particles also close to the interface. In the center of the interface the stresses relax to zero.

The different observations for the fully coupled case can be related to the elastic part of the free energy density. The heterogeneous ion distribution causes stresses at the interface that contribute to the elastic part of the free energy density $\tilde{f}^E$. To reduce the free energy density, those stresses have to relax. In the surface near regions, stresses can easily relax by deformation. In the bulk that heterogeneous deformation is limited. This leaves only the concentration redistribution to reduce the stresses, which causes a widening and smoothing of the interface. The numerical decoupled equilibrium concentrations are $c_\alpha = 0.142$ and $c_\beta = 0.858$, which are close to the theoretical values. It is observed that the concentration of the coupled example is decreased to $c_\alpha = 0.138$ and increased to $c_\beta = 0.862$. The coupled concentrations are highly depending on the stress field. The concentrations at the chemical free energy density minima and the interface thickness analyzed in the following are summarized in table 3.2. The interface thickness is calculated via trigonometry as $\tilde{s} = (\tilde{c}_\beta - \tilde{c}_\alpha)/\tilde{c}_{,i}^{max}$ and analyzed in figure 3.5. Here $\tilde{c}_{,i}^{max}$ is the numerical obtained gradient of the tangent of through the turning point of the concentration distribution, e.g. the center of the interface. The line plots across the interfaces utilized for the calculation are indicated in the figures 3.3b and 3.4b. The interface for the decoupled case is $\tilde{s}_{decoupled} = 5.97$ nm. This is close to the theoretical value $\tilde{s} \approx 5.9$ nm. The interface for the coupled case is $\tilde{s}_{coupled} = 7.6$ nm on the surface and $\tilde{s}_{decoupled} = 37.7$ nm in the bulk. That means that the difference between the theoretical interface thickness predicted by the Cahn-Hilliard model and the one calculated with the coupled model is about one order of magnitude. However, this is only a qualitative indicator of the bulk interface thickness as the interface thickness is too large in comparison to the sample dimensions, so that surface effects cannot be excluded.

Table 3.2: Analysis of the interface thickness. For the coupled case the interface thickness is measured once close to the surface and once in the center (bulk) of the sample.

	theoretical	decoupled	coupled
c_α	0.145	0.142	0.138
c_β	0.855	0.858	0.862
$\tilde{s}$	5.9 nm	5.97 nm	5.97 nm (surface); 37.7 nm (bulk)

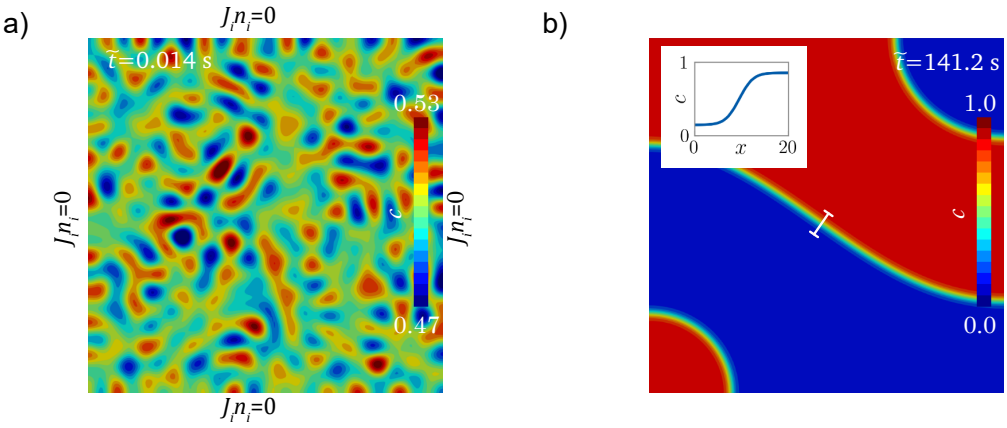

Figure 3.3: Concentration distribution for the non-coupled model. a) Homogeneous nucleation in the bulk after the first timesteps from the random initial distribution. b) In a late timestep the seeds agglomerate to few large particles. The concentration change across the interface along the white line is shown in the inset and analyzed in detail in figure 3.5.

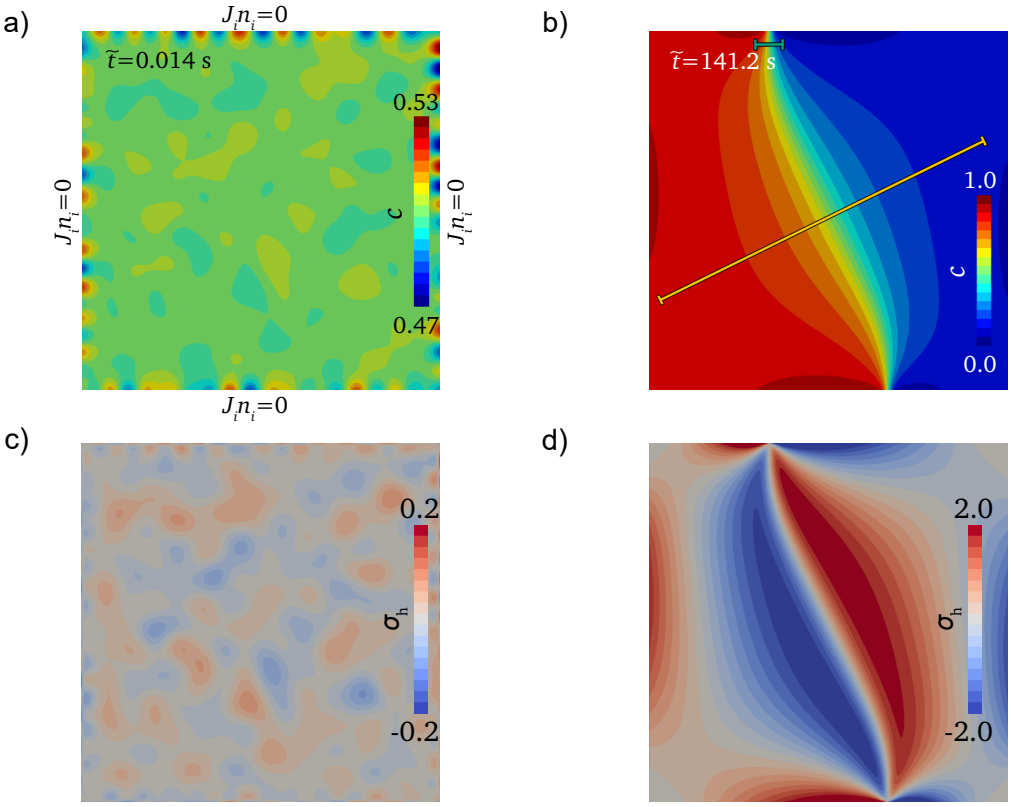

Figure 3.4: Concentration distribution for the chemo-mechanical coupled model. a) Nucleation on the free surfaces after the first timesteps from the random initial distribution. b) In the late timesteps the structure has evolved and only one grain of the high concentration phase and the low concentration phase each remains. Apparently the interface is much wider in the center of the volume than close to the free surfaces which is analyzed in figure 3.5 at the cross sections of the interface indicated by the white lines. The hydrostatic stress field σ_h is shown in c) after the first timesteps and b) at a late timestep. The largest compressive stress fields are in the high concentration particles close to the interface and the largest tensile stressfields are in the low concentration particles also close to the interface. In the center of the interface the stresses relax to zero.

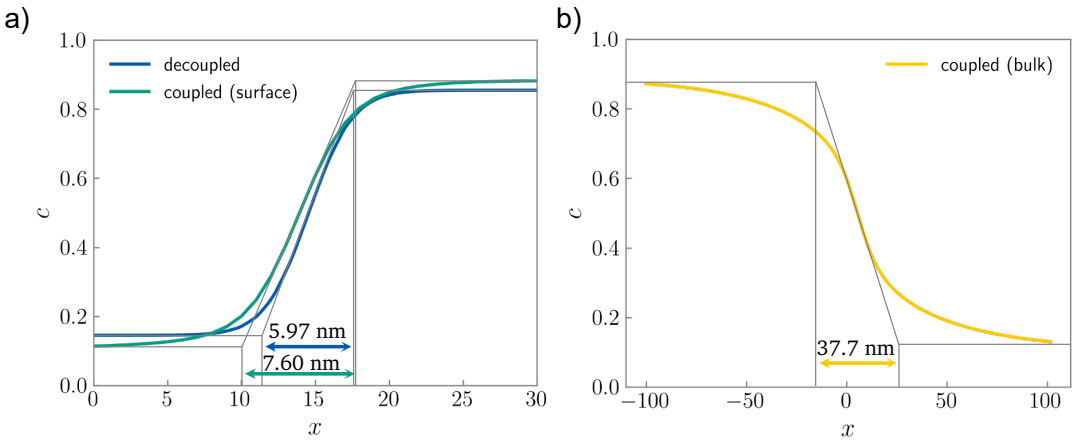

Figure 3.5: Concentration line plots across the interface as indicated in figures 3.3b) and 3.4b). a) The interfaces for the decoupled case is compared to the interface of the coupled case in the stress relaxed region near the surface. The interface thickness is close for two cases and the increase for the coupled case can be related to remaining stresses at the surface and the change of the concentrations with minimal chemical free energy density of the two phases. b) The stresses at the interface in the bulk cannot be released which causes a strong widening of the interface related to the elastic contribution to the free energy density.

3.4.5 Benchmark for the equilibrium concentration in the vicinity of an edge dislocation

The coupling of the stress and diffusion, e.g. the contribution of the hydrostatic stress field to the free energy density will cause the ions to redistribute around stress sources. For the equilibrium concentration around the stress field of an edge dislocation an analytical solution is derived in [125]. With the assumption of a small concentration $c \ll 1$, elastic parameters can be modified to open system elastic constants that account for the coupling between the concentration and a known stress field in equilibrium. The dimensionless analytical solution of the equilibrium concentration derived from the singular dislocation stress field solution is then given as [125]

$$c_{eq} = c_0 - c\eta(1+\nu_0)\frac{G_0 b}{\pi(1-\nu_0)}\frac{x_1^2 x_2 + x_2^3}{(x_1^2+x_2^2)^2}, \tag{3.66}$$

$$\nu_0 = \frac{\nu - c\eta^2 E}{1 + c\eta^2 E}, \tag{3.67}$$

where $\eta = \Omega/3$ is the coupling parameter, E is the Young's modulus and $G_0 = 0.5E/(1+\nu)$ is the shear modulus.

As a benchmark, a numerical simulation is done for the ion redistribution in the vicinity of a dislocation and the equilibrium concentration is compared and verified with the analytical solution. The sample size, mesh size, and traction boundary condition are equal to the stress benchmark for the edge dislocation described before. A homogeneous initial concentration $c|_{t=0} = c_{ref}$ is defined on the volume and boundary conditions for the concentration are set on all surfaces as $c_0 = c_{ref}$. The material properties defined correspond to $LiMn_2O_4$ as described in chapter 2.5.4. However, it should be noted that a Young's modulus of $10\,\mathrm{GPa}$ is applied in this simulation to avoid a large enrichment of concentration on the tensile side of the dislocation, which accounts for the fact that the analytical solution only applies to a small concentration. The equilibrium concentration from the numerical simulation and analytical calculation is depicted in figure 3.6.

Enrichment and depletion of concentration, referring to solute segregation, can be observed on the tensile and compressive sides of the dislocation, respectively. The numerical solution agrees well with the analytical solution outside the dislocation core region. However, in the analytical solution an infinite jump of the concentration across the dislocation core is calculated, whereas the jump of the concentration across the dislocation core for the numerical solution is finite. The origin for this is that the analytical solution is derived from

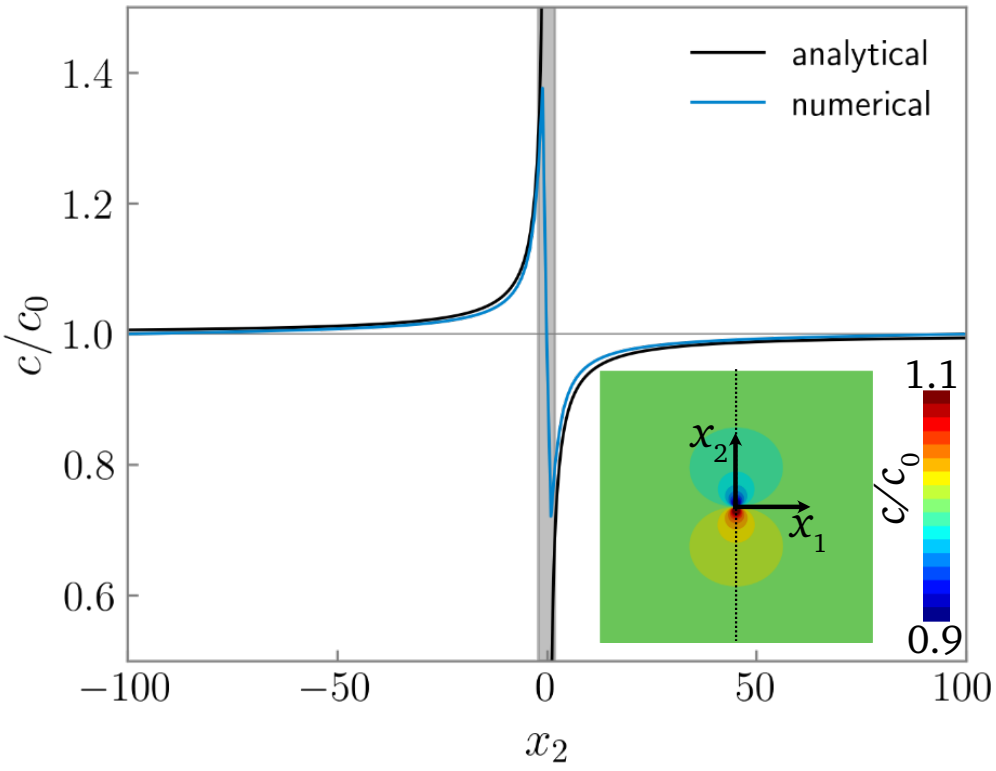

Figure 3.6: Redistribution of the concentration due to the stress field of the edge dislocation. The equilibrium distribution calculated with FEM shows good accordance with the analytical solution [125].

the classic singular solution and the numerical model is derived from the non-singular dislocation theory.

3.4.6 Benchmark for an edge dislocation close to a free surface in a two-phase material

In this section the benchmark for the driving force on a dislocation close to a free surface discussed in chapter 2.5.7 is extended with the mechanically coupled diffusion model for a misfit dislocation in a two-phase material. The material properties utilized for this benchmark correspond to lithiated and nonlithiated $LiFePO_4$ as described in chapter 3.4.3. In the numerical model the diffusion induced stress resulting from the concentration gradient across the interface accounts for the misfit strain. A fully coupled analytical solution is difficult to obtain, thus for a coupled solution the misfit strain is accounted for by a misfit stress field. The misfit strain is computed numerically for a particle with the dimensions 1500×1500 nm^2 consisting of 375×375 mesh elements. The coupled Peach-Koehler force is then $\widetilde{F}_1^{coupled} = \tilde{b}_1(\widetilde{\sigma}_{12}^{img} + \widetilde{\sigma}_{12}^{misfit})$. The coupled numerical example particle has the dimensions 1500×1500 nm^2 consisting of 1500×1500 mesh elements. The results are summarized in figure 3.7. The analytical driving forces are negative in the bulk volume of the sample and have strong positive values at the free surface. For the case of the singular solution, the driving force has a positive singularity at the position of the free surface. The non-singular solution has a positive peak close to the free surface and decreases to zero driving forces at the position of the free surface. The difference to the pure mechanical driving forces in figure 2.13 can be explained with the additional stress field due to the interface causing a negative driving force in the bulk pushing the dislocation inside the particle. Close to the surface is a point with zero driving force. For distances closer to the surface than this zero driving force the dislocation is pushed outside the particle. For the numerical solution however, the driving force is negative for all positions with a minimum close to the surface. The change of the system energy is then calculated. The analytical solutions show good agreement with minor differences related to the different solutions in the dislocation core. The kink of the singular solution in the core region has the origin in the misfit stress field not being subject to the cut-off radius. The numerical solution for the change of the system energy has larger negative values compared to the analytical solutions. This indicates a larger stabilization for the fully coupled model of the interface. With a singular dislocation theory it is necessary to specifically treat the core region to avoid unphysical results. Typically a cut-off radius is introduced. Here lies an advantage of using non-singular theory for dislocations where the results in the core region are finite and no such post processing is necessary.

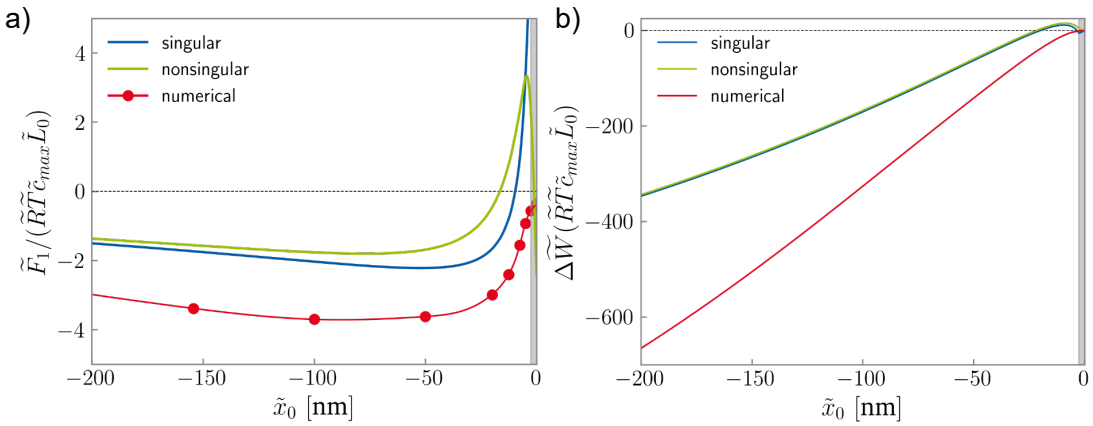

Figure 3.7: a) Driving forces on a misfit dislocation due to the image stress field superposed by the misfit stress field. The chemo-mechanical coupling in the numerical model causes a deviation. b) Work on a misfit dislocation calculated from the integration of the driving force in a).

4 Dislocation Mediated Ion-Diffusion in Lithium Ion Battery Materials

In this chapter dislocation mediated ion diffusion is analyzed and discussed, where the chemo-mechanical model for dislocations presented in chapter 3 is applied. As starting point the SOC dependence of the dislocation induced heterogeneity and its influence on the DIS is studied. Then the potentiostatic and galvanostatic charging behavior of a dislocation containing sample is analyzed. The SOC dependence of the ion mobility in dislocation containing samples is studied within the whole sample and the core near regions. A dislocation cluster shows the effect of multiple dislocations in close distance on the concentration distribution and the mobility. Finally the diffusion along the dislocation core in 3D for a pipe diffusion model with varying diffusion constant within the dislocation core is studied. The content of chapter has been partially published in [103].

4.1 Dislocation Induced Concentration Field Heterogeneity

Analyzing the interaction between diffusive ions and dislocations aids the understanding of various phenomena related to heterogeneous concentration observed in dislocation containing materials [130]. In the following a two-dimensional chemo-mechanical model is utilized to study the interaction between a single dislocation and diffusive ions within an $LiMn_2O_4$ particle in various examples. The numerical model considers a free standing particle with the sample size of $200\,\mathrm{nm} \times 200\,\mathrm{nm}$ and the mesh size of 200×200. The setting will be utilized for all the following two-dimensional simulations. In the simulations was observed that the DIS in the core region exceeds the yield stress for the material fracture [16] when the dislocation core parameter $\tilde{h}$ is small. Here it is referred to the figures 2.8 and 2.9. To model a more realistic material parameter the core parameter is chosen as $\tilde{h} = 5$ nm for all simulations in this chapter.

The first example shows the influence of the SOC on the concentration field heterogeneity in the vicinity of the dislocation core. For this purpose a series of experiments with varied SOC is conducted. The SOC is defined as the average concentration evaluated over the whole sample volume and is controlled by prescribing a concentration $c = c_0$ on the outer boundaries and the initial condition $c(t = 0) = c_0$ in the whole sample volume. The contour plot of the equilibrium concentration for SOC $= 0.5$ is shown in figure 4.1a and the concentration distributions along the x_2 axis for different SOC are shown in figure 4.1b. The ion redistribution around the dislocation generates an ion enrichment zone in the tensile and an ion depletion zone in the compressive side of the dislocation and the balance between the enrichment and the depletion zone is varying with the SOC. The redistribution is most pronounced at SOC $= 0.5$ reaching a maximum concentration jump that reduces towards lower and higher SOC. The redistribution is anti-symmetric with respect to SOC $= 0.5$, where the enrichment is stronger at low SOC and the depletion is stronger at high SOC. Further analysis leads to a relative concentration enrichment and depletion shown in figure 4.1c. Correlated to a lower ion concentration, the relative enrichment or depletion is more notable at a lower SOC, and the relative influence of the dislocation becomes negligible for an SOC close to 1. This could be an indicator, that the influence of dislocations on diffusion is stronger at low SOC. In fact, a similar experimental observation has been reported. The enrichment of Na-ions near the dislocation is more visible experimentally at a lower SOC, as reported by Xiao et al. [130]. The total jump of the concentration across the dislocation core $c_{max} - c_{min}$ is symmetric with respect to SOC $= 0.5$. Nevertheless, the amount of concentration enrichment and depletion are different for all SOC. At low SOC the maximum concentration enrichment is larger than the maximum concentration depletion. At high SOC, the maximum concentration depletion is larger than maximum concentration enrichment, but the relative difference between enrichment and depletion with respect to the SOC is small.

The first example is further analyzed regarding the diffusion induced stress. Ion intercalation causes a lattice deformation represented by the molar volume of the ions. In a free standing particle, stresses emerge at deformation gradients. Consequently, a concentration gradient will induce a deformation gradient and consecutive stresses, which in this work are referenced as DIS. Analoguous to the heterogeneous concentration distribution in the tensile and compressive sides of the dislocation, the dislocation induced DIS is non-uniform. Because of its opposite sign, the dislocation induced DIS causes a relaxation of the dislocation self stress. It can be described as the reduced hydrostatic stress $\Delta\sigma_h = \sigma_h - \sigma_h^0$, which is shown for different SOC in figure 4.1d, where σ_h^0 is the self-stress of the dislocation calculated by setting the lattice strain ε_{ij}^C to be zero. The SOC dependent DIS has the maximum value around SOC $= 0.5$ where the largest concentration jump was observed

across the dislocation core. It can be noted that the maximum and minimum DIS is not symmetric with respect to the SOC $= 0.5$ as highlighted in the inset of figure 4.1d. In the compressive side, the maximum tensile DIS is reached at SOC > 0.5 and in the tensilde side, and the maximum compressive DIS is reached at SOC < 0.5.

Until now only the equilibrium condition is considered. However, the dynamics during the charging operation do not allow the battery materials to relax to the equilibrium state during the process. In the following the diffusion influenced by the SOC dependent, heterogeneous concentration field related to the dislocation presence is analyzed during the two cases of potentiostatic and galvanostatic charging. The lithiation of the material is simulated with and without the dislocation to specifically show how the SOC dependent and heterogeneous concentration field around the dislocation core influences the diffusion. The potentiostatic charging is modeled by prescribing a concentration of $c_0 = 0.99$ on the bottom boundary, where the other boundaries are flux free. The galvanostatic charging is modeled by prescribing a constant, comparable ion flux of $j_0 = 0.001$ on the bottom boundary, where the other boundaries remain flux free. For the respective cases, the dislocation is placed in the center of the sample as before. The initial condition for both potentiostatic and galvanostatic charging is a homogeneous distribution $c(t = 0) = 0.05$. As reference a dislocation free body subject to equivalent boundary conditions is modeled. The resulting concentration profiles along the x_2 axis for various time steps are displayed in figure 4.2.

The potentiostatic charging is characterized by a strong concentration gradient at the beginning and a comparable fast charging rate, which both reduce over time. The concentration gradient in the galvanostatic charging is smaller and constant over time and the charging rate is slower. The concentration gradient and charging rate of the galvanostatic charging is strongly dependent on the prescribed parameters. In particular the concentration gradient is stronger for a higher prescribed flux boundary condition, and the charging is limited by the bulk diffusion into the sample. A comparable small flux boundary condition was chosen also to make sure that the center of the volume is charged before the surface concentration approaches $c = 1$ and the simulation becomes unstable as the free energy density function has a singularity at this concentration. Compared to the dislocation free reference an increase or decrease of the diffusion speed could not be observed. However, the solute segregation due to the dislocation stress field already leads to a heterogeneous concentration distribution around the dislocation core, which varies over time. This heterogeneous concentration distribution seems to be primarily dependent on the concentration level, as the profiles are similar to the equilibrium states discussed in figure 4.1b, and secondarily dependent on the time with the change of the charge state.

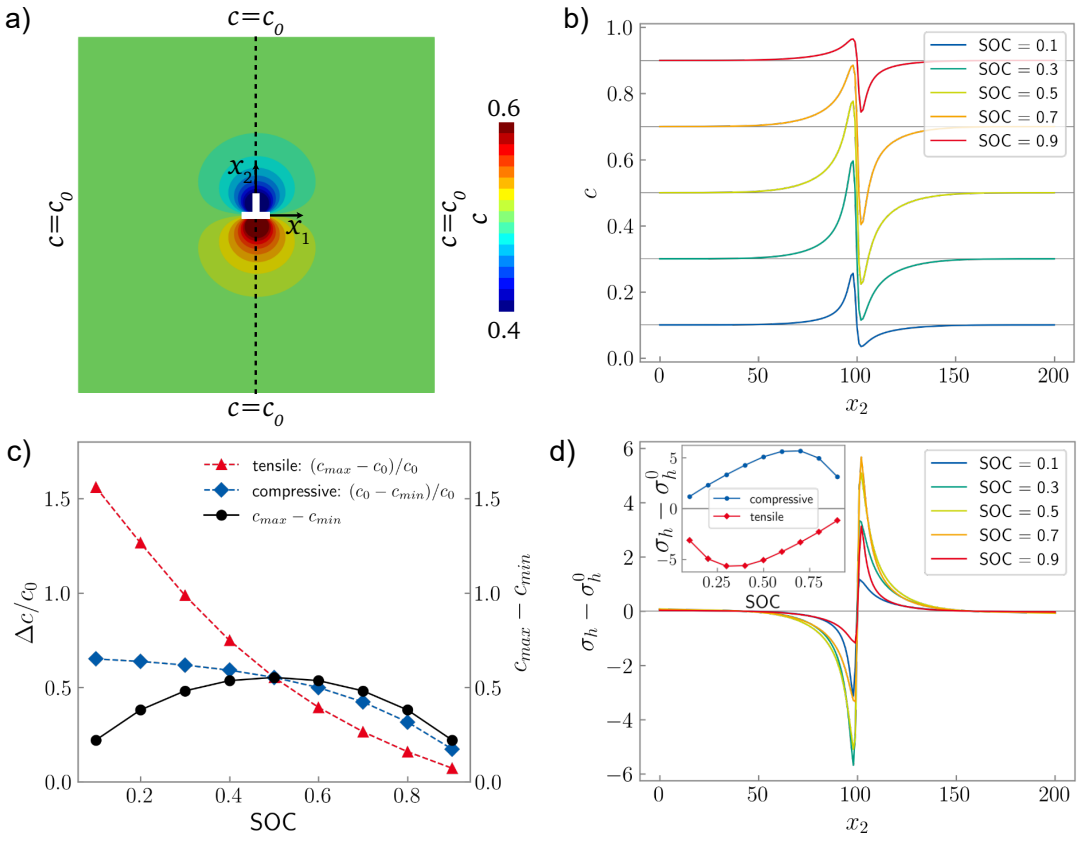

Figure 4.1: The simulations show the SOC dependency of the dislocation influence on the diffusion. a) Equilibrium concentration distribution near the edge dislocation for SOC $= 0.5$. b) The concentration along the x_2 axis for different SOC. The ion redistribution is most significant for SOC $= 0.5$ around the dislocation. c) The relative enrichment or depletion is calculated as $\Delta c/c_0 = (c_{max} - c_0)/c_0$ and $\Delta c/c_0 = (c_{min} - c_0)/c_0$ for the tensile and compressive side, respectively. c_{max} is the maximum value of the concentration field located in the tensile side as depicted in b) and c_{min} is the minimum value located in the compressive side, accordingly. The relative ion redistribution is more pronounced at a lower SOC. d) The hydrostatic DIS $\sigma_h - \sigma_h^0$ reduces both the tensile and compressive stress of the edge dislocation, where σ_h^0 is the self-stress of the dislocation. The hydrostatic DIS is also shown to be SOC dependent.

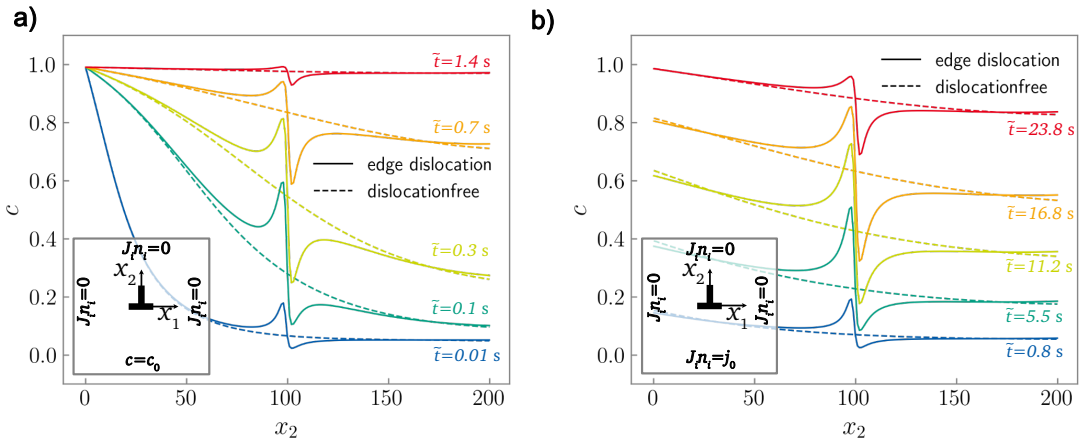

Figure 4.2: Influence of the edge dislocation on the concentration distribution during a) potentiostatic charging and b) galvanostatic charging. The inset shows the schematic setup with the boundary conditions. The concentration distribution over time along the x_2 axis is strongly influenced by the presence of the dislocation. The overall charging state is not influenced by the dislocation but its presence strongly alters the concentration distribution along the x_2 axis.

4.2 Ion Mobility in the Vicinity of an Edge Dislocation

A heterogeneous mobility can be observed in the vicinity of a dislocation, which is analogous to the enrichment and depletion of concentration around the dislocation core. To evaluate the mobility of the representative bulk material, one can consider the general idea of homogenization [96, 95]

$$\overline{J}_i = -M_{ij}^{eff}\overline{\mu}_{,j}, \tag{4.1}$$

where $\overline{J}_i$ and $\overline{\mu}_{,j}$ are the volume average of the flux and the chemical potential gradient, respectively, and M_{ij}^{eff} is the effective mobility matrix. The matrix M_{ij}^{eff} can be computed by a specific control of the boundary conditions. Here the average flux is controlled by applying constant flux boundary conditions and then the volume average of the chemical potential gradient can be evaluated. For two-dimensional problems, M_{ij}^{eff} consists of four unknown components that can be found by solving equation 4.1. Evaluation of two simulations with different flux directions leads to two groups of $\overline{\mu}_{,j}$. Accordingly one simulation is performed with a constant flux in the x_1 direction and one simulation is performed with a constant flux in the x_2 direction. To evaluate the SOC dependence the simulation is repeated accordingly by controlling the SOC by the initial condition that defines a homogeneous concentration $c(t=0) = \text{SOC}$.

The concentration distributions for the constant flux in positive and negative x_1 direction and in positive x_2 direction are shown in figure 4.3a,b and c, respectively. The results show that the numerically computed offdiagonal components of M_{ij}^{eff} are zero. The evaluation of the diagonal components M_{ii}^{eff} is depicted in figure 4.3d,e and f, where because of the anti-symmetric stress field in the x_2 direction the flux is evaluated for the positive and negative flux. The maximum mobility is observed at $\text{SOC} = 0.5$ and the mobility decreases for lower and higher SOC. The relative difference between M_{11}^{eff} and M_{22}^{eff} is only around $0.001\,\%$, which means that the dislocation does not introduce large mobility anisotropy in the material. Further the averaged mobility of the whole sample is not influenced by the dislocation presence, as indicated by comparison of the mobility of the dislocation containing sample and the dislocation free sample. However, when calculating the mobility at each node using equation 3.27, it follows that the heterogeneous concentration distribution results in a heterogeneous local mobility. Therefore the mobility is evaluated locally as M_{core}^{eff} in the tensile and compressive regions marked by square boxes of sidelength $a = 2b$ depicted in figure 4.3a. A shift of the maximum value of the SOC dependent local mobility is observed, where the maximum mobility is reached

at a lower SOC within the tensile region and at a higher SOC within the compressive region. This is caused by the enrichment and depletion of concentration at the tensile and compressive sides, respectively. The local mobility M_{22}^{eff} is analyzed in detail along the x_2 axis, where the result for the positive flux is depicted in figure 4.4a and the result for the negative flux is depicted in figure 4.4b. According to equation 4.1, the average chemical potential gradients are of opposite sign in the two simulations. However, this does not influence the local mobility (and concentration) in the dislocation core region, which can only be observed as SOC dependent.

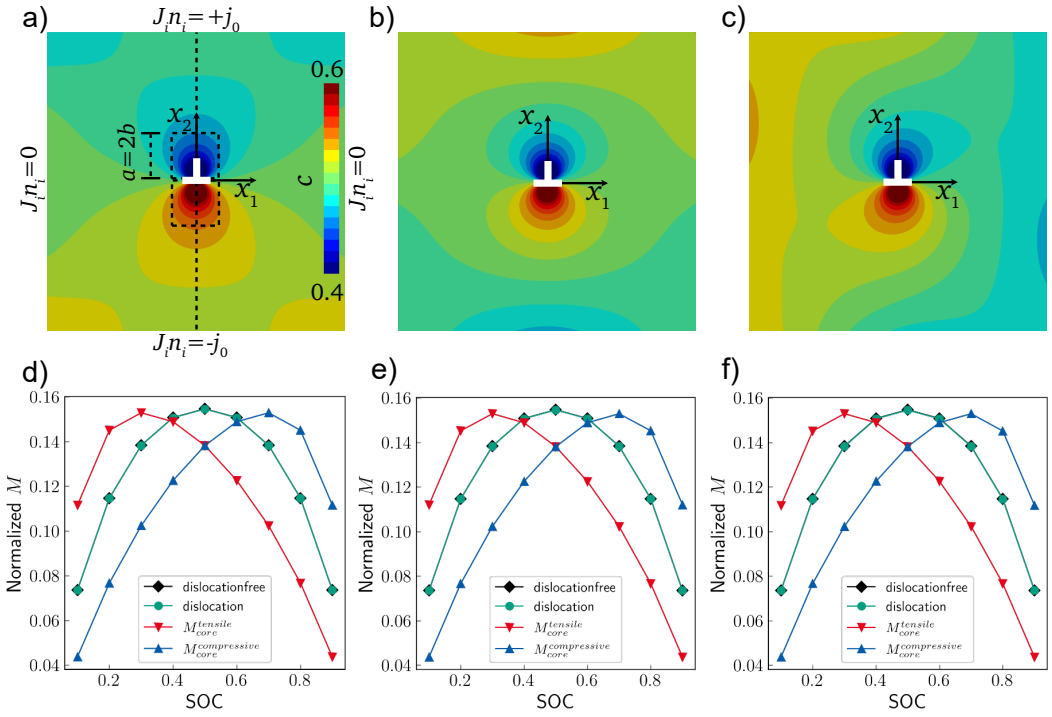

Figure 4.3: Influences of the dislocation on the ion mobility. Concentration field around the edge dislocation with a) a positive flux in the x_2 direction, b) a negative flux in the x_2 direction and c) a positive flux in the x_1 direction. The change of the mobility in dependence of the SOC is shown for d) positive x_1 direction, e) positive x_2 direction and f) negative x_2 direction. The dislocation influences the local mobility around the dislocation core, but the average mobility in the whole volume matches the mobility of a dislocation free reference sample.

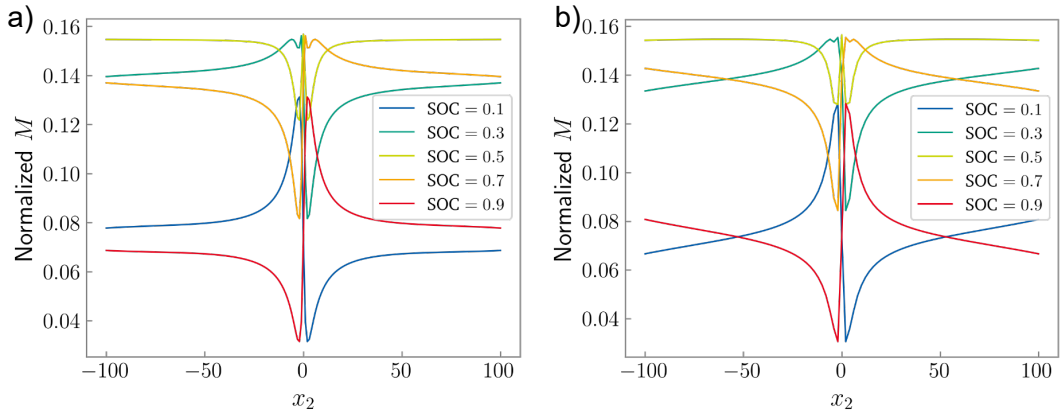

Figure 4.4: The local mobility along the x_2-axis for a flux in the positive is shown in a) and a flux in the negative x_2 direction is shown in b). The mobility in the dislocation core region is not influenced by the chemical potential gradient induced by opposite signed flux and only shows dependency on the SOC.

Oppositely signed dislocations interact in the form of a resulting shear stress acting in the dislocations, where the influence of the dislocation induced shear stress on diffusion is studied in various theoretical models [128, 68, 14, 141]. In this work the solute segregation within a dislocation array is analyzed. Each single dislocation is introduced by adding the corresponding eigenstrain distributions. An example for a dislocation array with oppositely signed edge dislocations is shown in figure 4.5. The distance between the dislocations in vertical and horizontal direction is $40\,\mathrm{nm}$. The flux boundary condition $J_i n_i = \pm 0.0001$ is applied on the bottom and top surfaces. The SOC is controlled by the initial homogeneous condition $c(t=0) = \mathrm{SOC}$ as before, where an $\mathrm{SOC} = 0.4$ is chosen as example for the discussion. Due to the superposition of the dislocation stress field of the oppositely signed edge dislocations enhances both the tensile and compressive stress fields. This results in interconnected areas of increased concentration in the tensile region and decreased concentration in the compressive region, as shown in figure 4.5a. Specifically at $\mathrm{SOC} = 0.4$, the local concentration increase on the tensile side of the dislocation creates a region where the concentration exceeds 0.5. According to figure 4.3d, for an $\mathrm{SOC} < 0.5$ an increased concentration leads to an increased mobility. However, when the concentration is further increased to $c > 0.5$, the mobility decreases. Similarly, on the compressive side of the dislocations, a decreased concentration results in a decreased mobility. Consequently a strong SOC heterogenity across the dislocation array leads to an according mobility

heterogenity. Compared to a single dislocation, a dislocation array introduces larger areas with concentration field heterogeneity.

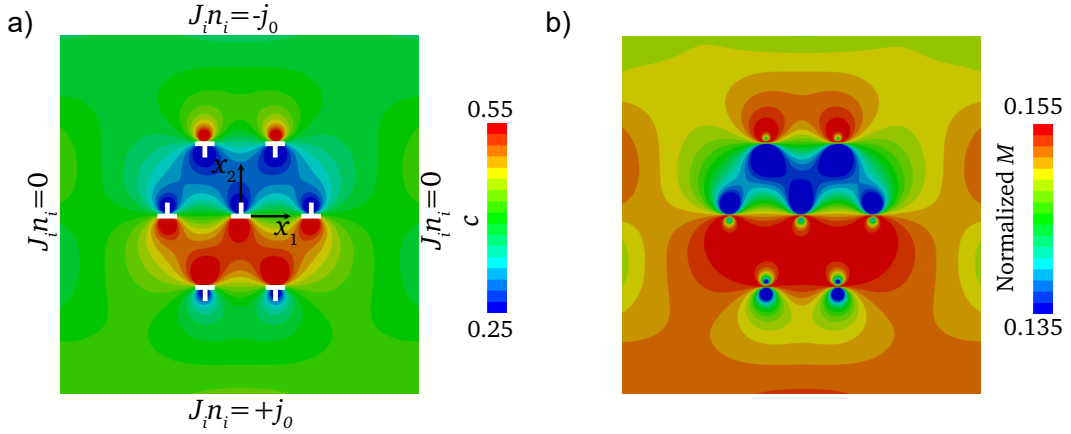

Figure 4.5: A dislocation array subject to a flux in negative x_2 direction. a) Ion enrichment and depletion due to dislocation stress fields at interconnected areas. b) Local mobility distribution. The mobility is increased in the tensile region and decreased in the compressive region.

4.2.1 Study of the different terms in the mobility

Different terms contribute to the mobility defined in equation 3.27. These are the terms for the mixing characterized by the parameter χ and the stress. In this section the individual contributions are analyzed by comparing simulations where the mobility equation is modified. The mobility variants are labeled as M_I, M_{II} and M_{III} and are defined in the following. First the equation for the mobility is replicated in its normalized form from equation 3.27 along with its derivative with respect to the concentratio

$$M = \frac{c(1-c)}{1 - c(1-c)[2\chi - \frac{1}{9}C_{ijkl}\Omega_{ij}\Omega_{kl}]},$$
$$M_{,c} = \frac{1-2c}{(1 - c(1-c)[2\chi - \frac{1}{9}C_{ijkl}\Omega_{ij}\Omega_{kl}])^2}. \tag{4.2}$$

Note that the interface parameter κ is set to zero. Also the chemical potential is unmodified and contains terms for the mixing and stress so that all three variants have chemo-

mechanical coupling. In the analysis the mobility calculated from the experiments using equation 3.27 is referred to as M. The mobility and chemical potential of the first variant I is defined by setting both the term for mixing and the stress term to zero as

$$\begin{aligned} M_I &= c(1-c), \\ M_{I,c} &= 1-2c, \end{aligned} \tag{4.3}$$

which returns the classic definition for the mobility. Variant II is defined by considering the mixing term and setting the stress term to zero as

$$\begin{aligned} M_{II} &= \frac{c(1-c)}{1-c(1-c)2\chi}, \\ M_{II,c} &= \frac{1-2c}{(1-c(1-c)2\chi)^2}. \end{aligned} \tag{4.4}$$

The last Variant III considers only the stress term and the mixing term is set to zero so that

$$\begin{aligned} M_{III} &= \frac{c(1-c)}{1+c(1-c)\frac{1}{9}C_{ijkl}\Omega_{ij}\Omega_{kl}}, \\ M_{III,c} &= \frac{1-2c}{(1+c(1-c)\frac{1}{9}C_{ijkl}\Omega_{ij}\Omega_{kl})^2}. \end{aligned} \tag{4.5}$$

The simulations were performed with all the parameters utilized in the previous section, except that the modified definitions for the mobility are applied. Accordingly the boundary conditions and setup defined given in figure 4.3a and the prescribed flux is in the positive x_2 direction. Each simulation is repeated for a different specified SOC in the range from 0.1 to 0.9. For comparison, all simulations were performed with and without a dislocation in the center of the particle. The simulations are conducted until the equilibrium is reached and then the mobility is analyzed. The results for the simulations with the mobility variants are summarized in figure 4.6. The analytically calculated mobility variant M_{II} for a bulk material is shown in figure 4.6a for different χ. Naturally, for the limit $\chi = 0$, the two variant solutions are equal $M_{II}(\chi = 0) = M_I$. In the range $0 < \chi < 2$ the mobility increases with an increased χ. When $\chi = 2$, the mobility function has a singularity at $c = 0.5$. When $\chi > 2$, the mobility function has two singularities and the mobility has negative values for the concentration between those singularity points. The results for the numerical calculated mobility with $\chi = 1$ are shown in figure 4.6b. The dashed lines indicate the respective analytical solutions, where M_{II} is identical to $M_{II}(\chi = 1)$ in figure 4.6a.

The numerical solutions agree well with the analytical solutions. The mobility M, which contains the contribution of all terms, is compared to the mobility variants. The curves for both M_I and M_{II} lie above M and the curve for M_{III} lies below M. This means that the mixing term has an increasing effect on the mobility and the stress term has a decreasing effect.

The global mobility within a particle with dislocation and without dislocation is similar. However, similar as observed in the last section, the mobility changes in the tensile and compressive region. The tensile region of the dislocation is evaluated in figure 4.6c and the compressive region of the dislocation in figure 4.6d. Coinciding with the discussion in chapter 4.2, the maximum mobility in the tensile region is shifted to a higher SOC and in the tensile region the maximum mobility is shifted to a lower SOC.

4.3 Pipe Diffusion

The proposed model is generally formulated and covers three-dimensional problems. Its phase field character enables smooth coupling to various physical phenomena. Pipe diffusion is referred to as high speed diffusion along a dislocation line [130, 118, 30, 65]. Although the phenomena is known for a long time, a fundamental understanding is lacking. In this section the chemo-mechanical coupled diffusion model is utilized to study pipe diffusion along the dislocation core. For this, the model is coupled to a pipe diffusion model following by locally modifying the diffusion constant D [84]. The homogeneous core diffusion coefficient D_{core} is defined within a tube along the dislocation line with radius of $2.5\,\mathrm{nm}$, as illustrated by the dashed curves in figure 4.7a. The diffusivity in the dislocation 'pipe', e.g. the dislocation core, can be a few orders larger than that in the bulk material [42]. Therefore pipe diffusion with $D_{core} = 100D_0$ and $D_{core} = 1000D_0$ is studied. The simulation volume is defined with an edge dislocation lying along the x_3 axis is placed in the center of a volume of $50\,\mathrm{nm} \times 50\,\mathrm{nm} \times 20\,\mathrm{nm}$ with mesh size of $50 \times 50 \times 20$. A homogeneous distribution $c(t = 0) = 0.05$ is applied as initial condition. Diffusion in the vicinity of such a dislocation pipe can be considered for three normal directions. However, for the in-plane diffusion cases in figure 4.2, the large volume of the surrounding bulk dominates the ion diffusion such that no obvious influence was observed with a larger diffusion coefficient in the dislocation core. Therefore the expected resulting flux is along the negative x_3 direction. Similar to the boundary condition of the potentiostatic charging, a prescribed concentration $c_0 = 0.99$ is applied on the front boundary (the $x_3 = 10$ plane) and flux free boundary conditions are applied on the other

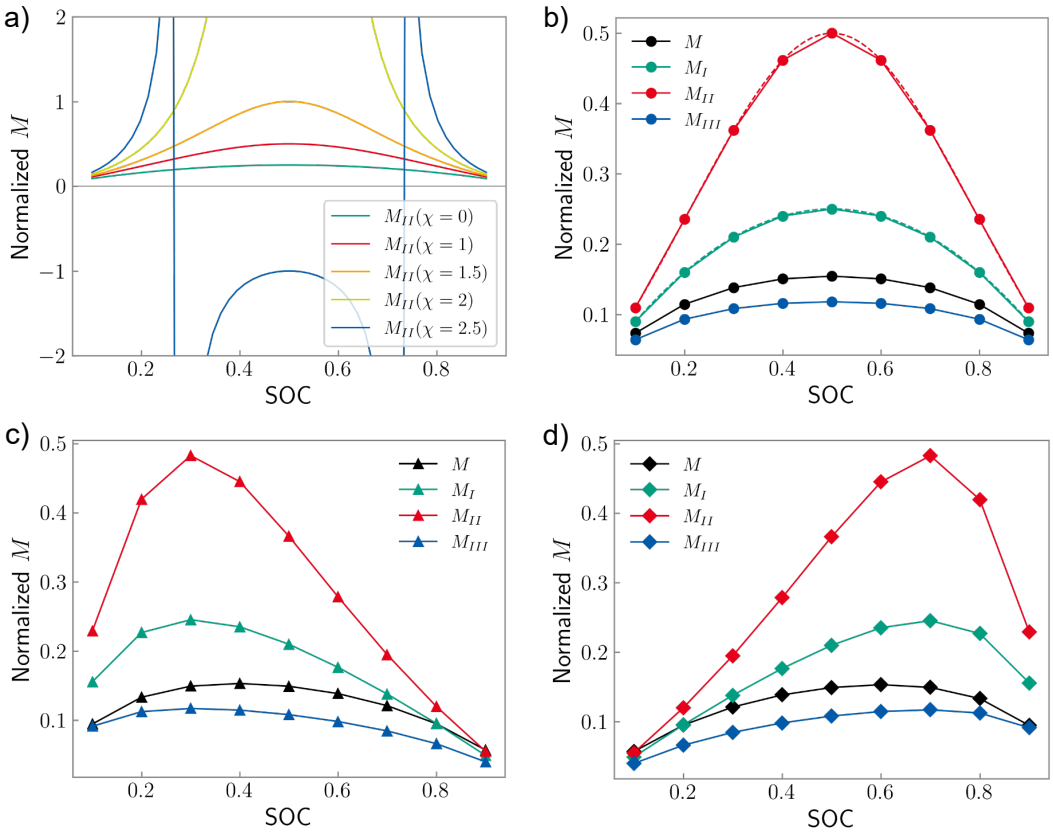

Figure 4.6: The mobility is studied for different variations and depending on the SOC. a) Analytic calculation of the mobility M_{II} for different χ-parameters. Singularities and negative mobility values are introduced for $\chi > 2$. Note that for $\chi = 0$, it states that $M_I = M_{II}$. b) Mobility of a sample containing an edge dislocation. c) With the mobility in the vicinity of an edge dislocation evaluated in the c) tensile region and d) compressive region.

boundaries. The results for diffusion along the dislocation line are shown as concentration plots at $t = 0.009$s in figure 4.7. As already discussed in figure 4.3, in the low SOC state the mobility on the tensile side of the dislocation is related to the concentration enrichment. This results in a pipe of higher diffusivity in the tensile region along the dislocation line, visible as an area with larger concentration in figure 4.7a. This phenomenon is enhanced when $D_{core} = 100D_0$, where a diffusion pipe can already be observed on the tensile side of the edge dislocation, as shown in figure 4.7b. A clear pipe diffusion can be observed when $D_{core} = 1000D_0$. However, in this case, the pipe diffusion is mostly due to the large diffusivity predefined in the tube along the dislocation line and less due to the interaction of the diffusive ions with the tensile stress. To better understand the dislocation induced pipe diffusion, a stress dependent diffusivity [41] instead of a predefined diffusion coefficient can be considered in the model, but this is out of the scope of this work.

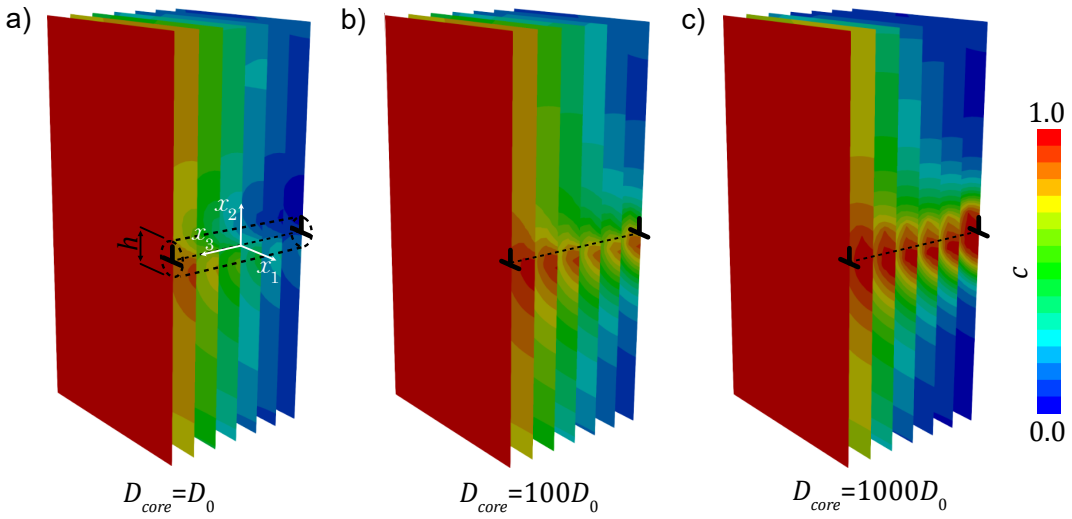

Figure 4.7: Ion diffusion along the dislocation line at $\tilde{t} = 0.009$s with different core diffusion coefficients D_{core}. Faster ion diffusion can be observed on the tensile side of the edge dislocation indicated by the high concentration tube.

5 Driving Forces on Misfit Dislocations in Two-Phase Electrode Particles

In two-phase materials a dislocation will interact with the interface, especially when there is a strong misfit strain at the interface due to lattice mismatch. This leads to more stable positions of the dislocation at the interface oriented with the Burgers vector parallel to the interface, such that the dislocation stress field partially cancels the misfit stress field. The relation of particle sizes and shapes with the stability of misfit dislocations is analyzed in this chapter. First the interaction of a dislocation with the diffusive ions for isotropic phase separation is analyzed depending on the model parameters. On this basis the influence of a dislocation in a mechanical coupled two-phase diffusion model with anisotropic elasticity is studied. It will be discussed that the shear component of the misfit strain causes a driving force on the dislocation. Another driving force on the dislocation comes from the interaction of the dislocation with the surface in the form of image forces. The combination of the driving forces leads to an energy based stability condition which is sensitive to the particle size. Dislocations are stable when the work on the dislocation by the driving forces to introduce a dislocation into the particle is zero or negative. Then the influence of the particle shape on the critical particle size is studied as well as the influence of the interface position in a consecutive section. The chapter is concluded with a discussion on the model parameters. The content of chapter has been partially published in [140].

5.1 Phase Separation in Isotropic Dislocated Solids

The linear elastic chemo-mechanical coupled model for dislocations is depending on various parameters, that can be fitted to experimental data. However, the fit to the experimental data is out of the scope of this work. Instead the according parameters were chosen in a physical sound manner and a discussion on the influence of these parameters

is shown in the following section. The interplay between the dislocation and separation of phases is to a high degree defined by the core parameter $\tilde{h}$ and the the mixing parameter χ, which is studied in the following. The parameter χ is related to ion-ion coupling and a value $\chi > 2.0$ leads to phase separation, where the phases are separated by an interface characterised by the interface parameter κ, as discussed in chapter 3.1. When the definition for the mobility in equation 3.27 is applied, the mobility has singularities for $\chi \geq 2$. To avoid this, the mobility defined in equation 4.3 was applied. More details on the topic are discussed in chapter 4.2.1. Following the discussion in chapter 3.4.4, the interface parameter was chosen as $\kappa = 5.0$ leading to a theoretical stress free interface thickness of $\tilde{s} \approx 5.9$ nm.

In accordance with the previous experiments, The numerical model considers a free standing particle with the sample size $200\,\mathrm{nm} \times 200\,\mathrm{nm}$ and the mesh size of 200×200 and an edge dislocation in the center with the Burgers vector $b = b_0(100)$ and glide plane normal vector $n = (010)$. The material is considered isotropic and the properties for $LiMn_2O_4$ were applied according to chapter 2.5.4. Traction free boundary conditions were applied for the displacement variable. The concentration on the boundary was set to $c = 0.5$ and the initial concentration was set as $c(t = 0) = 0.5$. The resulting concentration profiles were evaluated on a line along the x_2 axis through the dislocation core and shown in figure 5.1. The influence of the dislocation stressfield is already discussed in figures 2.8 and 2.9, where a smaller $\tilde{h}$-parameter leads to larger stress fields and is related to a larger strain energy and thus dislocation self energy. Figure 5.1a shows that the smaller $\tilde{h}$-parameter also leads to a larger enrichment, respectively depletion, around the dislocation core as the concentration field follows the stress field. Thus the enlarged stress field also results in an increased ion redistribution. The ions also carry an intercalation strain which decreases the DIS for smaller $\tilde{h}$ as shown in figure 5.1b. It should be noted that for $\tilde{h} = 1$ nm the concentration maximum and minimum reaches unphysical values of 1 and 0, respectively. For a more realistic behavior a value of $\tilde{h} = 5$ nm was chosen for the experiments.

In the following three simulation sets with different SOC where conducted, where each set consists of a simulation series with variation of the χ-parameter. The SOC was controlled by defining different initial conditions as $c_I(t = 0) = 0.2$, $c_{II}(t = 0) = 0.5$ and $c_{III}(t = 0) = 0.8$. The results are shown in figure 5.2. Concentration distributions for the whole sample are shown for $\mathrm{SOC} = 0.2$, $\mathrm{SOC} = 0.5$ and $\mathrm{SOC} = 0.8$ in figure 5.2a, b and c, respectively for the example of $\chi = 2.5$. Respective line plots along the x_2 direction are shown in figure 5.2d, e and f. The cases $\mathrm{SOC} = 0.2$ and $\mathrm{SOC} = 0.8$ show similar behavior, where the low concentration phase is dominant in the low SOC case and the high concentration phase is dominant in the high SOC case. The complementary high

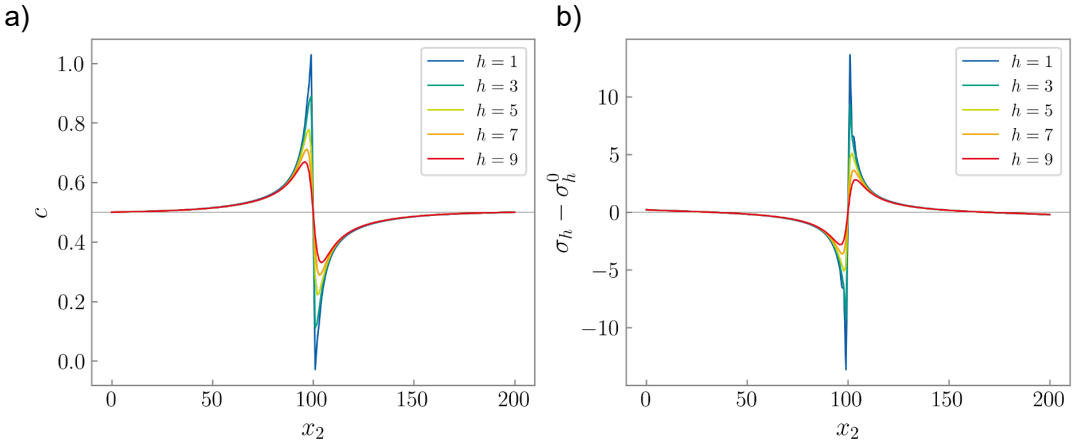

Figure 5.1: a) Concentration field around an edge dislocation for different $\tilde{h}$-parameter. b) DIS around an edge dislocation for different $\tilde{h}$-parameter.

concentration and low concentration phases are formed in the tensile region and the compressive region of the dislocation, respectively. In the case $\mathrm{SOC} = 0.5$ the two phases are evenly distributed. The tensile side of the dislocation favors the high concentration phase and the compressive side favors the low concentration phase. However, on the left and right sides of the particle additional phases are formed. This could be related to the traction free surfaces and mechanical equilibrium of the stresses within the sample. Noteworthy is the non-conformity of the interface thickness in different regions within the sample. The interface is thin close to the free surfaces where the displacement can relax the interface stress field. In the volume, the interfaces are much thicker. The stress field at the interface causes a redistribution of the ions towards a wider interface as discussed in the previous chapter on the spinodal decomposition. Finally the interface at the dislocation core is also thin. Here the dislocation stress field is opposed to the interface stress field causing a stress relaxation and interface widening due to the stress field is prevented. Further the increase of the χ-value causes a stronger concentration separation close to the dislocation core. For $\mathrm{SOC} = 0.2$ and $\mathrm{SOC} = 0.8$ there is a distinct jump between $\chi = 2$ and $\chi = 2.5$ towards the phase separation. At $\mathrm{SOC} = 0.5$ the transition is evenly. Increasing the value to $\chi = 3$ results in a qualitative different concentration distribution. The maximum and minimum concentrations are closer to the values $c = 1$ and $c = 0$, respectively. The phase nucleation on the surface is reverse to the phase nucleated at the dislocation core, such that the concentration distribution close to the surface is strongly

heterogeneous and shows three interfaces along the line plot. Also the concentrations are increased in the high concentration phase and decreased in the low concentration phase relative to the cases of $\chi \leq 2.5$, which is related to the free energy density f^C. Which phase is nucleated on the surface can be related to the surface stresses on the free surfaces due to the dislocation.

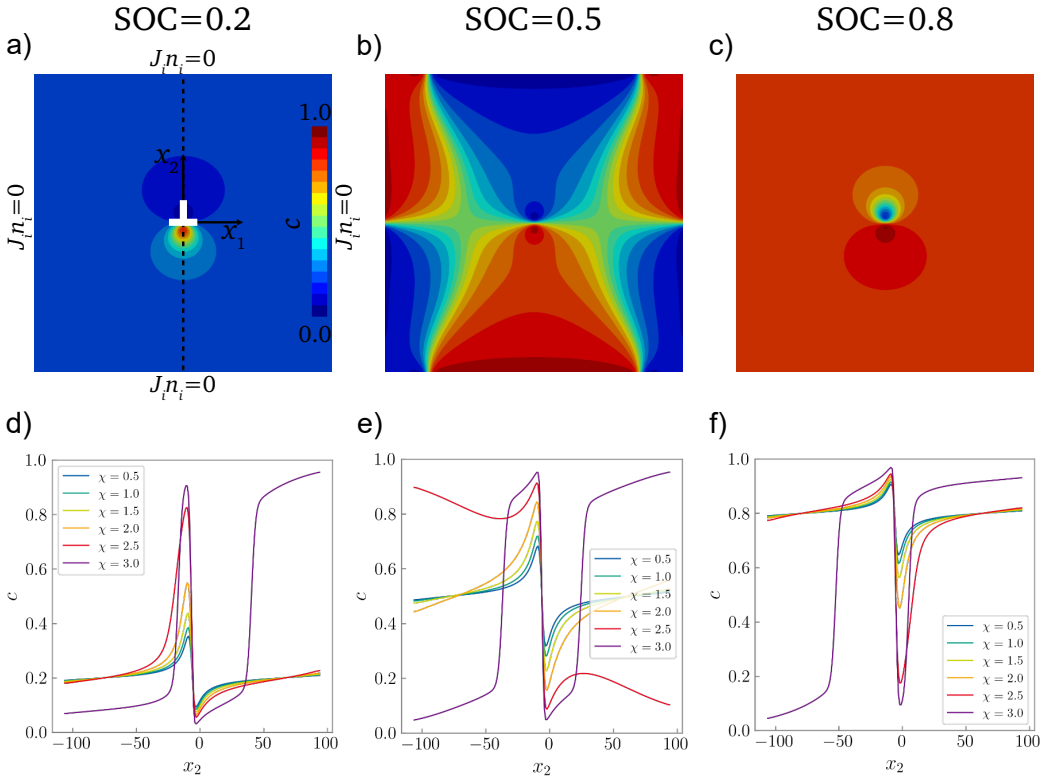

Figure 5.2: Concentration fields for $\chi = 2.5$ at a) $\mathrm{SOC} = 0.2$, b) $\mathrm{SOC} = 0.5$ and c) $\mathrm{SOC} = 0.8$. For $\mathrm{SOC} = 0.2$ and $\mathrm{SOC} = 0.8$ one phase is dominant with the other phase nucleated at the core. At $\mathrm{SOC} = 0.5$ both phases are equally stable and the phases are heterogeneously distributed around the dislocation core. Line plots of the concentration are shown in d) for $\mathrm{SOC} = 0.2$, in e) for $\mathrm{SOC} = 0.5$ and in f) for $\mathrm{SOC} = 0.8$. The lines are plotted along the x_2 axis through the dislocation core as indicated by the dashed line in a).

The last example discusses the dynamic interaction of a dislocation with a moving diffusion

front during the charging process including phase separation. This was already discussed for non-phase separation material in chapter 4.1. As a reference, the charging is calculated for a dislocation free sample as well. The initial and boundary conditions represent potentiostatic charging and are taken from the potentiostatic charging in figure 4.2. Further parameters are set as $\chi = 2.5$ and $\kappa = 5$. The results are summarized in figure 5.3. The dislocation free reference sample is shown in figure 5.3a at $\tilde{t} = 4.2$ s, in figure 5.3b at $\tilde{t} = 10.6$ s and at $\tilde{t} = 15.5$ s. The diffusion front has three stages, marked by the position of the diffusion front beeing in the first half, exactly at the center and in the second half of the sample. It can be compared that relative to the diffusion at the surface, the diffusion in the center is faster in the first half and slower in the second half. In general the interface is dragged towards the center of the particle. The timesteps in the sample with the dislocation correspond to those in the dislocation-free sample, where the diffusion front approaches the dislocation in figure 5.3d, where the diffusion front passes the dislocation in figure 5.3e, and where it surpasses the dislocation in figure 5.3f. When the diffusion front approaches the dislocation, the diffusion front is dragged towards the dislocation. When the diffusion front is at the same height of the dislocation, the interface is flat. Here the interface is thin at the dislocation. This is related to the dislocation self stress opposite to the DIS, as discussed before. When the diffusion front passed the dislocation the interface is pinned at the dislocation. Together with the drag of the interface towards the center of the sample observed in the dislocation-free example, the interface is curved due to the presence of the dislocation.

5.2 Critical Particle Size for Stable Dislocations

In this chapter the misfit dislocations in anisotrop phase separation in $LiFePO_4$ material are analyzed. First the misfit dislocations and their orientation appearing in $LiFePO_4$ are discussed and the parameters for the simulations are defined. From experiments it is known that misfit dislocations in LFP particles can have the Burgers vector in the [100], [010] and [001] directions [29]. Esmizadeh and Haftbaradaran [27] analyzed the minimum particle size for stable misfit dislocations in LFP, which is related to the misfit strain. The maximum misfit strain is for the interface in the (010) plane of $5.03\,\%$. The respective misfit dislocations are with the sense vector in the [001] direction and the Burgers vector of $1.033\,\mathrm{nm}$ in the [100] direction. The study on particles with an aspect ratio of 2 with the long side in the [010] direction shows a predicted particle width (defined as the small diameter) around $47\,\mathrm{nm}$, below which the particle is unlikely to host a misfit dislocation at the phase boundary. Interfaces in other directions result in less

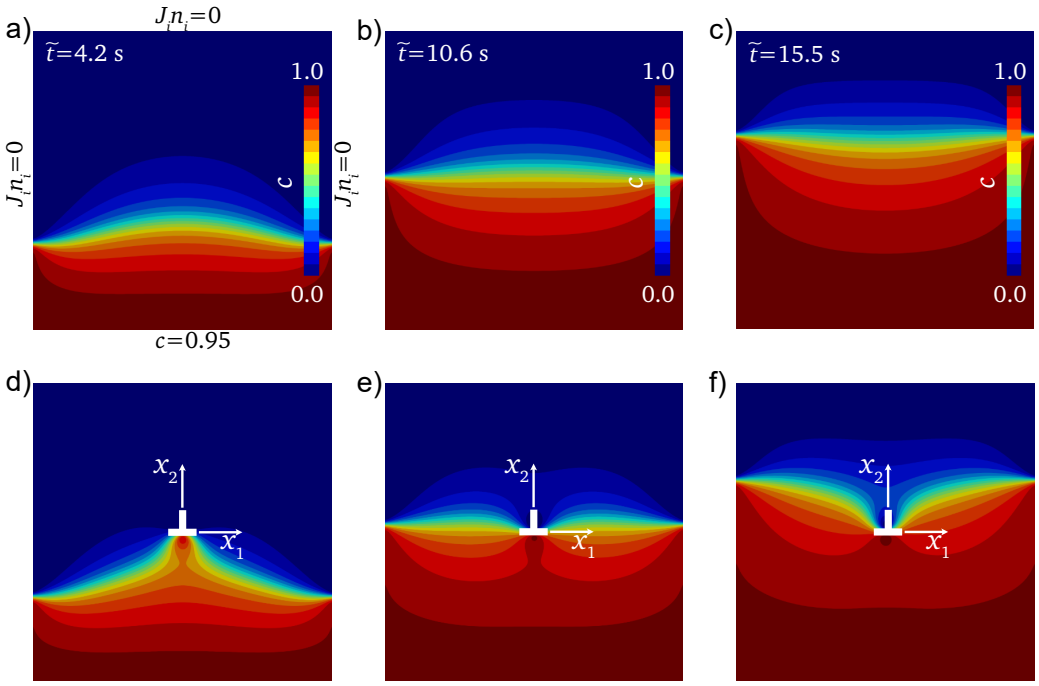

Figure 5.3: Potentiostatic charging of a dislocation-free sample (a-c) and a dislocation containing sample (d-f) at different timesteps. Before the diffusion front passes the dislocation, the high concentration phase is dragged towards the dislocation (d). After the diffusion front passes the dislocation in f), the diffusion front is pinned at the dislocation.

stable directions. For example the critical particle width for dislocations with the sense vector in the [100] direction and Burgers vector in [001] direction was predicted around $200\,\mathrm{nm}$.

Larger particle sizes are associated with lithiation heterogeneities due to limitations in the ion-transport. Nanometer-sized electrode particles on the other hand could evade the development of large misfit strains and thus are a key factor in realising intercalation cathodes [78]. Coinciding, excellent capacity retention during cycling was found for small rod-like LFP particles with the length $50\,\mathrm{nm}$ and width $20\,\mathrm{nm}$ [55]. From above observations it can be concluded that similarly small sized particles will not be influenced by the dislocation line along the [100] direction. Therefore, the focus in this work lies on the analysis of the minimum particle size for stable misfit dislocations with the dislocation sense vector in the [001] direction and the Burgers vector of $1.033\,\mathrm{nm}$ in the [100] direction.

With the Peach-Koehler equation 2.41 the driving force on the dislocation in the $\tilde{x}_1$ direction can be calculated as

$$\tilde{F}_1 = \widetilde{\sigma}_{12}\tilde{b}_1 + \widetilde{\sigma}_{22}\tilde{b}_2. \tag{5.1}$$

As only the component of the Burgers vector b_1 is non-zero for the considered dislocation, it is sufficient to take only the interaction with the shear stress $\widetilde{\sigma}_{12}$ into account. Considering $\tilde{F}_2$ as the driving force on the dislocation for the generation of misfit dislocation would require dislocation climb, which is energetically more expensive than the glide and thus less favourable. Thus $\tilde{F}_1$ is considered as driving force along the minimum energy path for the dislocation moving in or out of the material.

The simulations in this chapter vary in dimension and shape. If not stated otherwise, the following parameters are chosen. A consistent mesh resolution is achieved by defining the size for a single element as 0.25×0.25 nm^2 so that the definition of the mesh resolution is independent on the particle size and shape. Further, one mesh element is reasonably small compared to the core width parameter $\tilde{h} = 2$ nm, as will be discussed within this chapter. The boundary conditions on the free surfaces are defined as traction free for the displacement variable and as flux free for the concentration variable. The initial concentration is defined in the form of a step function as

$$c(t=0) = \begin{cases} 0.032 & \text{for } x_2 > x_2^0 \\ 0.968 & \text{for } x_2 \leq x_2^0 \end{cases}, \tag{5.2}$$

where the concentration values are the equilibrium concentrations of the low concentration and high concentration phase and x_2^0 is the x_2-position of the interface. As a standard in

this chapter the interface position is defined with $x_2^0 = 0$. The setup of a particle with a dislocation is depicted in figure 5.4. A dislocation is placed at $P = (x_1, x_2^0)$ and the x_1-position is iterative varied along the interface. As discussed within this chapter, the end time for the simulations was chosen as $\tilde{t} = 14.2$ s.

The critical particle size is determined by evaluation of the energy required to introduce a misfit dislocation into the material. First the driving forces are numerically computed for the dislocation on its gliding path along the grain boundary into the particle, as shown in figure 5.4. Then the integration of the driving force returns the change of the system energy as

$$\Delta\widetilde{W} = \int_0^{\tilde{x}_0} \widetilde{F}_1 d\tilde{x}_1. \tag{5.3}$$

The driving force computation follows the procedure described in chapter 2.5.2. Here the driving force is calculated from the sum of all nodal configurational forces on the boundaries of the sample. With that the configurational force contains the contributions from all defects within the sample volume, which in this case are the dislocation and the phase boundary. The driving force on the phase boundary is zero in the equilibrium state, so that the residual driving force contains only the contribution from the dislocation. The numerical driving forces is computed for discrete dislocation positions along the gliding plane, which is interpolated with a spline interpolation. Trapezoidal integration is applied to calculate $\Delta\widetilde{W}$.

In the following a suitable mesh resolution and the required time until the equilibrium state is reached is discussed. First the convergence with the mesh resolution is studied. The particles have the edge length of $50\,\mathrm{nm}$ with the dislocation and interface in the center. The computations are done for three different mesh resolutions with element sizes 1.0×1.0 nm^2, 0.5×0.5 nm^2 and 0.25×0.25 nm^2. The simulation was stopped after $\tilde{t} = 14.2$ s. The results for the driving force on the dislocation and the change of the system energy are depicted in figure 5.5a and b. Due to convergence a sufficiently small error for the determination of the critical particle size can be assumed for the mesh consisting of elements of the size 0.25×0.25 nm^2. The determined mesh size of 0.25×0.25 nm^2 per element is then tested for different times and the driving forces on the dislocation and the change of the system energy after $\tilde{t} = 0.014$ s, $\tilde{t} = 14.2$ s and $\tilde{t} = 71.0$ s are depicted in figure 5.5c and d. The change of the system energy ΔW is not changing after $\tilde{t} = 14.2$ s, thus this is regarded as the equilibrium state.

In figure 5.6a and b the eqilibrium concentration distribution of a square two-phase particle with and without dislocation is compared. For that the stress fields due to the misfit strain and the dislocation self stress are considered along with the effect on the concentration

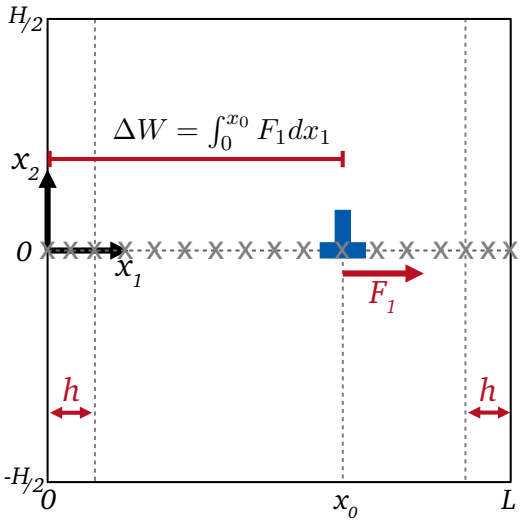

Figure 5.4: Evaluation of the change of the system energy for the generation of dislocations. The dislocation is placed at the position $(x_0, 0)$ within the particle of width L and height H. The path of the dislocation into the particle is reproduced by step-wise variation of the x_1-position (marked by the crosses along the gliding plane). On each position the driving force F_1 is evaluated and then interpolated as a spline to a continuous driving force along the dislocation path. The numerical integration then gives the change of the system energy ΔW. The critical region within the core width h from the free surface is highlighted and can be excluded from the evaluation by defining a cut-off radius $r_c = h$. Then the integral reads as $\Delta W = \int_{r_c}^{x_0} F_1 dx_1$. The two phases are not depicted in the graphic and normalized entities are utilized for simplicity.

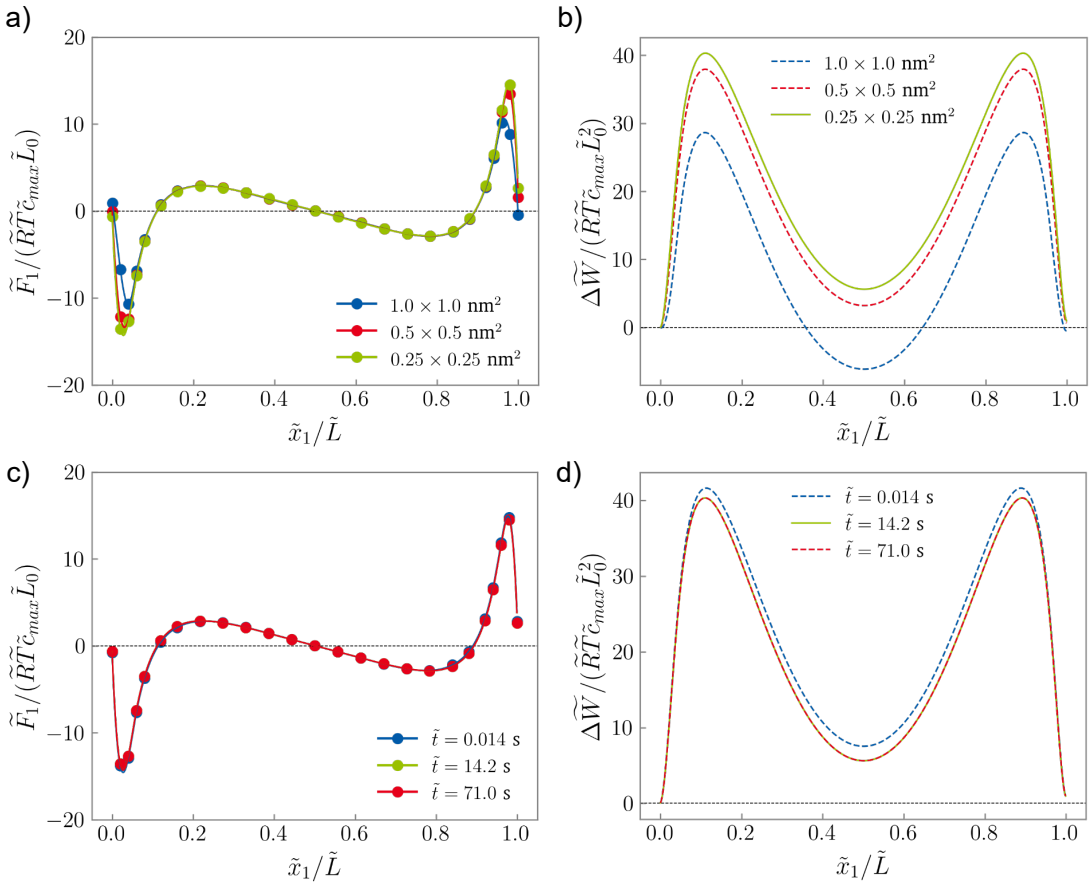

Figure 5.5: Convergence of a) the driving force $\widetilde{F}_1$ on the dislocation and b) the change of the system energy $\Delta\widetilde{W}$ with the mesh resolution indicates a suitable element size for the mesh of $0.25 \times 0.25\ \mathrm{nm}^2$. Then the driving force $\widetilde{F}_1$ on the dislocation in c) and the change of the system energy $\Delta\widetilde{W}$ in d) is computed at different times indicating the end time $\tilde{t} = 14.2\ \mathrm{s}$ as the equilibrium state.

field. An ion redistribution and as a concequence a widening of the interface is observed along the phase boundary, which can be related to the emerging hydrostatic stresses due to the misfit strain following the discussion for interphases in isotropic two-phase materials in chapter 4.1. Similarly, the dislocation stress field opposes the misfit stress and reduces the interface thickness as shown in figure 5.6b. Figure 5.6c and d analyze the time evolution of the shear stress $\widetilde{\sigma}_{12}$ along the $\tilde{x}_1$ direction in the interface and the hydrostatic stress $\widetilde{\sigma}_h$ plotted in the $\tilde{x}_2$ direction through the center of the particle and interface. The two depicted time steps are the first time step calculated at $\tilde{t} = 0.014$ s and a time step in equilibrium at $\tilde{t} = 14.2$ s. The strongest shear stresses emerge at the free surfaces, and the shear stress is zero in the center of the particle. The strongest hydrostatic stresses emerge close to the interface and the hydrostatic stress is zero at the interface. It can be seen that the stresses relax between the first and last timestep, showing the relation between stress evolution and concentration redistribution from the initial step distribution to the smoothened equilibrium distribution. Figure 5.6b also shows the distribution of the nodal configurational force $\tilde{g}_i$ in the dislocation core region. In the mechanically coupled phase transformation problems, the configurational forces are a resultant of both the dislocation self stress and the DIS. Analogue to the stress evolution of the dislocation-free sample the driving force on the dislocation also decreases during the relaxation of the interface.

In the next step the driving forces on a dislocation in a square two-phase particle is analyzed for different sizes of the particle and the analysis of the change of the system energy $\Delta\widetilde{W}$ leads to a stability criterion and a critical particle size for stable dislocations. The analysis of the driving forces and the change of the system energy of the dislocation is shown in figure 5.7. The driving forces along the gliding plane are largest in the surface near region and show three positions where the driving forces are zero. Those positions with zero driving forces mark the equilibrium positions of the misfit dislocations and it can be distinguished between one equilibrium position at the center of the phase boundary and two equilibrium positions in the left and right surface near regions of the phase boundary. Moreover, the equilibrium position in the center has a negative slope of the driving force, while the slope of the equilibrium positions near the surface is positive. As the driving force is defined as the negative gradient of the free energy ($\tilde{F}_i = -\mathrm{d}\tilde{f}/\mathrm{d}\tilde{x}_i$), the negative slope of the driving force curve has the meaning of a positive second order derivative of the free energy. Therefore the position in the center is a stable equilibrium position, while the two other positions are unstable equilibrium positions. For larger particles the relative positions of the outer equilibrium positions shift towards the surface. However, the slope of the driving force does not change regardless of the particle size. This remains until the prohibition of the two-phase coexistence for very small particles [18]. Thus the center of the phase boundary is always a stable equilibrium position for the dislocation.

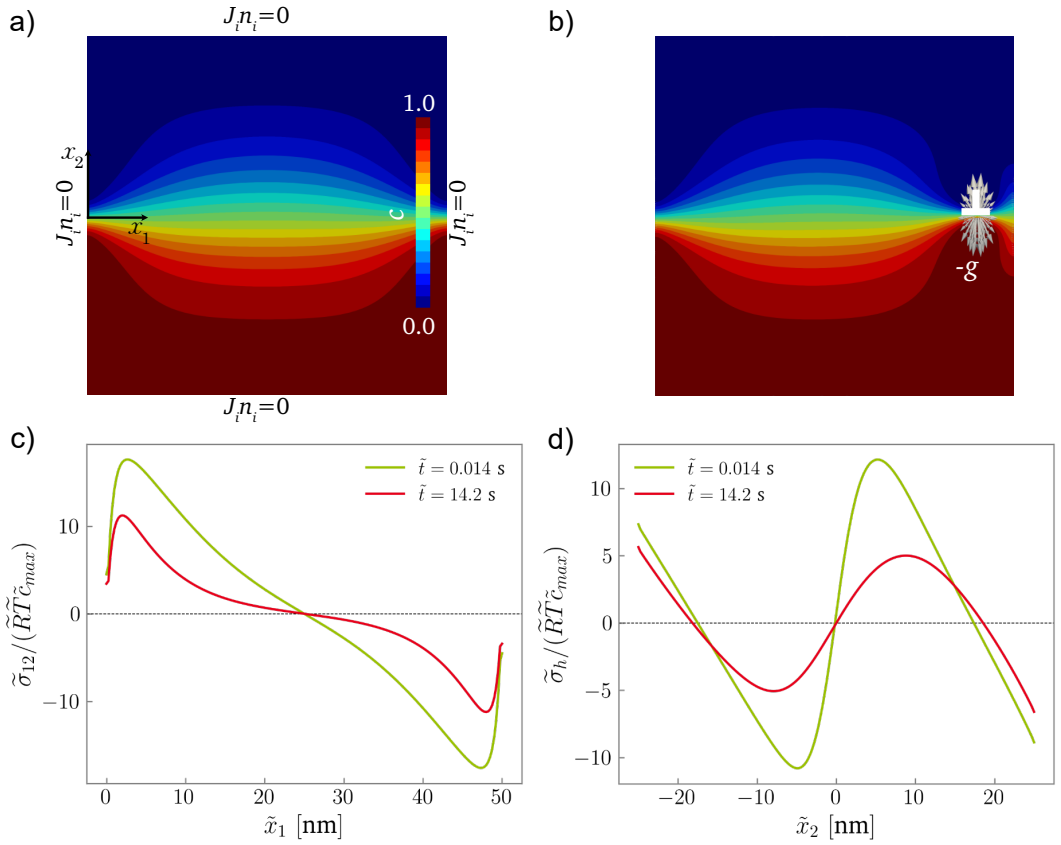

Figure 5.6: Analysis of the interface relaxation due to the misfit strain. a) Equilibrium concentration without misfit dislocation. b) Equilibrium concentration with a misfit dislocation. c) Distribution of the shear stress $\widetilde{\sigma}_{12}$ at $\tilde{x}_2 = 0$ along the $\tilde{x}_1$ direction. d) Distribution of the hydrostatic stress $\widetilde{\sigma}_h$ at $\tilde{x}_1 = 50\,\mathrm{nm}$ along the $\tilde{x}_2$ direction.

The previous discussion does not yet include information if the formation of the misfit dislocation is favoured from an energetically point of view, e.g. if the misfit dislocation is stable within the particle. This is done in the following by calculating the change of the system energy to reveal a size dependent stability criterion. Figure 5.7b shows the analysis of the change of the system energy $\Delta\widetilde{W}$ for different particle sizes. When the misfit dislocation is located in the surface near region, the formation energy is always positive. This is related to an increase of the system energy when the dislocation glides into the particle. The two maxima of the system energy change $\Delta\widetilde{W}_{max}$ coincide with the unstable equilibrium positions from the zero driving force points. The maxima are also equivalent to the energy barrier that has to be overcome to introduce a misfit dislocation into the volume of the particle, which can be normalized as $W_{max} = \Delta\widetilde{W}_{max}/(\widetilde{R}\widetilde{T}\tilde{c}_{max}\tilde{L}_0^2)$. Because of $\Delta\widetilde{W} > 0$ for the formation of dislocations located on the two unstable equilibrium points, the existence of the misfit dislocation is energetically not favoured regardless of the particle size without any work exchange with the surrounding. This leaves the equilibrium position in the center as remaining option to define a stability criterion. Depending on the particle size values for $\Delta\widetilde{W}$ at this position above and below zero are found. In particular for small particles, $\Delta\widetilde{W} > 0$ for all dislocation positions. Thus the dislocation is energetically unstable for small particles. For large particles $\Delta\widetilde{W} < 0$ for the dislocation positions in the center, which means that those dislocations are energetically favoured. The particle size with $\Delta\widetilde{W} = 0$ at the center equilibrium position marks the smallest possible size for energetically favoured dislocations in the particle. This is defined as the critical particle size for the formation of dislocations. For the given parameters the predicted critical particle size is $\tilde{L}_c = 52.5\,\mathrm{nm}$. Further the energy barrier decreases with increasing particle size, so that the introduction of misfit dislocations into particles smaller than the critical particle size is more difficult the smaller the particle is.

5.3 Influence of the Particle Shape

Tailoring the shape of particles is an efficient instrument to improve charging efficiency and capacity preservation over the lifetime of the material [55]. In this sense the shape dependence for the critical particles size for stable misfit dislocations is studied by variation of the aspect ratio. Considered are rectangular particles of width L and height H, where the aspect ratio is defined as $a = \widetilde{H}/\tilde{L}$. The phase boundary and dislocation are located at half the height of the particle. Due to the varying particle shapes the critical particle size is interpreted as a critical particle width and a critical specific surface area which

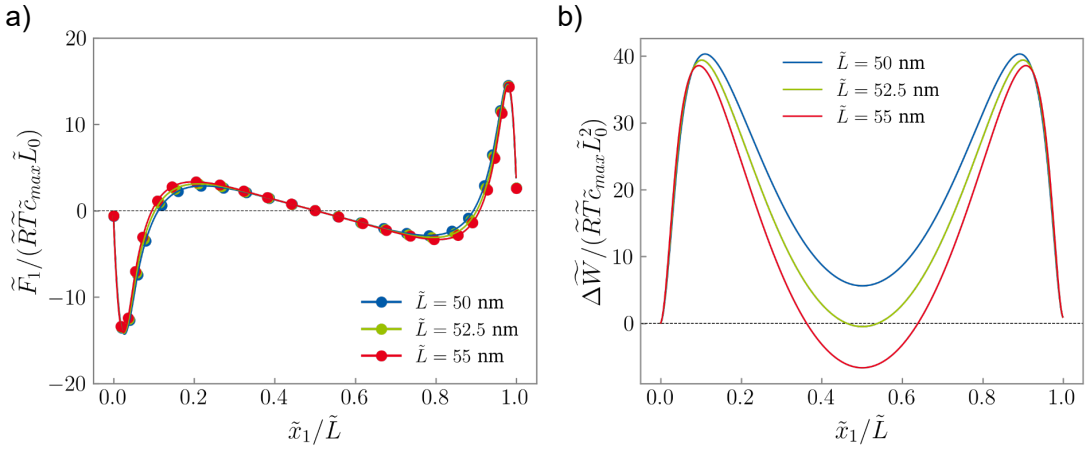

Figure 5.7: Determination of the critical particle size. a) Driving force on the dislocation at different positions on the phase boundary for three different particle sizes. b) Change of the system energy for the formation of the misfit dislocation for different particle sizes. The critical width is predicted as $52.5\,\mathrm{nm}$.

is defined as the total surface per unit volume $\tilde{S}_c = 2\tilde{L}_c(1+a)/(a\tilde{L}_c^2) + 2/\tilde{l}_z$, where $\tilde{l}_z$ is the length of the particle in the out of plane direction. The results for a particle with $\tilde{L} = 50$ nm are summarized in figure 5.8. First the influence of the aspect ratio is studied for a particle with the width $L = 50$nm. In figure 5.8a is shown, that the shear stress $\widetilde{\sigma}_{12}$ increases with increasing aspect ratio, albeit with a saturating effect towards larger aspect ratios. Figure 5.8b shows the increase of the driving forces with increasing aspect ratio. Finally figure 5.8c shows, that $\Delta\widetilde{W}$ decreases for larger aspect ratios creating regions with $\Delta\widetilde{W} < 0$ in the center where dislocations are energetically stable. Therefore the additional height has an energetically stabilizing effect on the misfit dislocation. Figure 5.8d shows the relation of the critical particle width $\tilde{L}_c$ and the aspect ratio. It indicates an exponentially decrease of the critical particle width with respect to the aspect ratio. The critical specific surface area shows a maximum around $1.5\,\mathrm{nm}$ and a decrease for larger aspect ratios. A large specific surface area is beneficial for the rate capability of electrode particles. An aspect ratio of $1.25 < a < 1.5$ would then allow for dislocation free particles with a larger specific surface area.

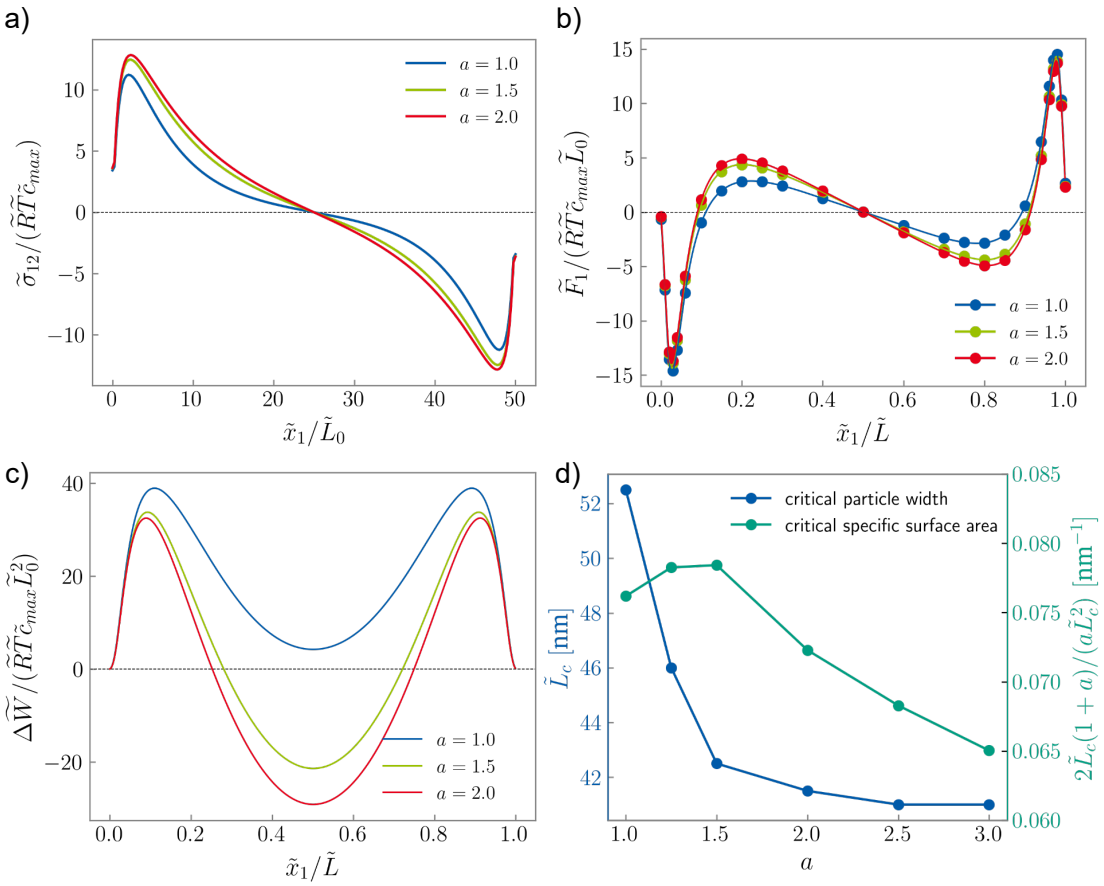

Figure 5.8: Analysis of the influence of the particle aspect ratio $a = \widetilde{H}/\tilde{L}$ on the critical size of dislocation free particles. a) The shear stress $\widetilde{\sigma}_{12}$ at the phase boundary in dislocation-free particles increases with increasing aspect ratio. Accordingly the driving force on the dislocation increases with increasing aspect ratio shown in b), which leads to a stabilization of the dislocation indicated by the change of the system energy shown in c). The shape dependence is summarized in d). The critical particle width $\tilde{L}_c$ decreases with larger aspect ratios and saturates for aspect ratios $a \leq 2.5$. The corresponding specific surface area has a maximum around $a = 1.5$ with a trend to decrease for larger aspect ratios.

5.4 Influence of the Interface Position

The critical particle size for stable dislocations size also depends on the position of the interface within the particle. In this section a study to estimate the critical particle size is conducted varying the position of the interface $\tilde{x}_2^{PB}$ relative to the particle height $\widetilde{H}$ for particles with different aspect ratios $a = 1$ and $a = 2$. The results are shown in figure 5.9a. As already discussed, the critical particle width is smaller when the aspect ratio is larger. The closer the interface is positioned to the upper and lower surfaces, the larger the critical particle width becomes. Exemplary, the critical particle width for $a = 2$ with the interface at at $\tilde{x}_2^{PB} = -0.3\widetilde{H}$ is approximately $18\ \%$ larger than at the minimum in the center. This is related to the reduced shear stress of interfaces close to the free surfaces, as discussed by Esmizadeh and Haftbaradaran [27]. An asymmetry is observed with respect to $\tilde{x}_2^{PB} = 0$. This is related to the different elastic properties of the LFP and FP phase. For $a = 2$ the minimum $\tilde{L}_c$ is at $\tilde{x}_2/\widetilde{H} = 0$, while it is at $\tilde{x}_2/\widetilde{H} = 0.1$ for the aspect ratio $a = 1$. When the interface is very close to the surface, curvature of the interface is observed as shown in figure 5.9b. This happens for $a = 1$ when the distance of the interface is smaller than $\tilde{x}_2/\widetilde{H} \leq 0.2$ and for $a = 2$ when $\tilde{x}_2/\widetilde{H} \leq 0.1$. This means that the assumption of the misfit dislocation gliding along the phase boundary is not satisfied anymore and thus the critical particle width is not analyzed for those cases. The distance to the surface when bending occurs is $13\,\mathrm{nm}$ for both aspect ratios, and seems to be independent on the aspect ratio. In figure 5.9b tilting of the interface is shown, where the interface is pinned on its original position by the dislocation. In figure 5.9c, the interface is curved such that it intersects with the bottom free surface. The analysis shows that it is sufficient to analyze the critical particle width for an interface positioned in the center of the particle, e.g. $\tilde{x}_2^{PB} = 0$. For the large aspect ratio $a = 2$, the minimum critical particle width is found with the interface positioned in the center. This is not the case for $a = 1$, but the deviation in the critical particle width is negligible.

5.5 Discussion

In the chemo-mechanical coupled non-singular continuum theory for dislocations various factors are critical for a qualitative prediction of the critical particle size for stable misfit dislocations in two-phase particles. In the following the influence of a series of parameters is analyzed and discussed. First the interface relaxation between the initial state and the equilibrium state and the difference between utilizing phase-specific elasticity and

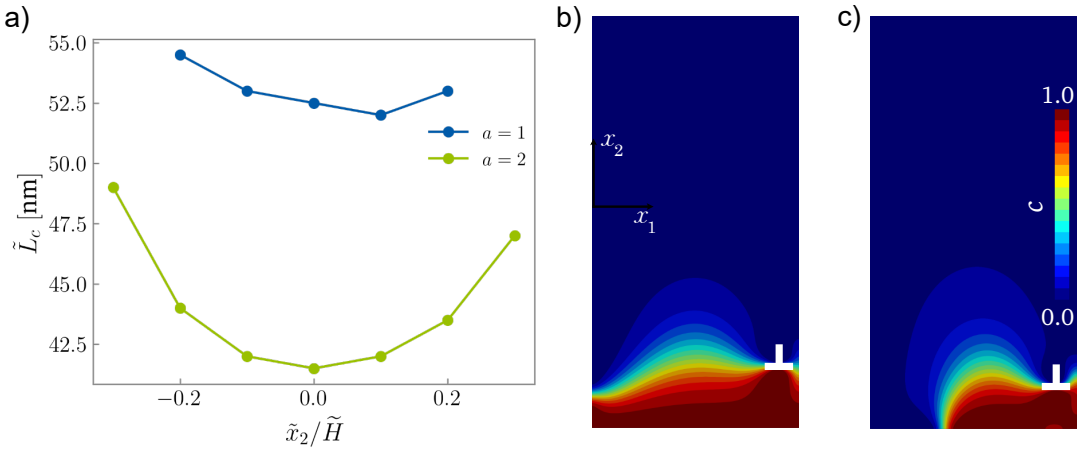

Figure 5.9: The position of the boundary within the particle has an influence on the stability of misfit dislocations. a) The critical particle width is shown for two different particle aspect ratios in relation to the phase boundary position. The stability of misfit dislocations is increased when the phase boundary is through the center of the particle. The results are asymmetric with respect to $\tilde{x}_2^{PB} = 0$, which is related to the different stiffness tensor in the LFP and FP phase. b,c) When the phase boundary position is close to the surface, tilting and curving of the interface is observed.

utilizing homogeneous elasticity is studied. Then the influence of the core parameter $\tilde{h}$ is analyzed. Conclusive is a discussion on the interface model applied in the simulations.

There can be a significance difference between the initial state and the equilibrium state for the driving forces on defects due to relaxation processes (see also the relaxation of the interface in figure 5.6). In the following this influence on the critical particle size is analyzed for the differences between the initial and the equilibrium state. In the work of Esmizadeh and Haftbaradaran [27], the utilization of a sharp interface model was discussed as a model limit because of the lacking stress relaxation and ion redistribution. The applied model in this work allows to study this effect in the sense of time evolution. In the first state the concentration distribution is a step function, with only minimal stress relaxation and concentration redistribution at the interface. The results for a sample with the dimensions 52.5×52.5 nm are shown in figure 5.10a-b. The first computed timestep at $\tilde{t} = 0.014$ s is compared to a later timestep in equilibrium at $\tilde{t} = 14.2$ s analyzing the driving forces on the dislocation and change of the system energy, respectively. As can be expected from the relaxation of the shear stress discussed in figure 5.6c, the transition to the equilibrium state is accompanied with a reduction of the driving forces on the dislocation. In detail the driving forces between the unstable equilibrium position and the center decrease, but the driving forces between the unstable equilibrium position and the surface increase during the relaxation. Interestingly the larger driving forces without relaxation do not lead to a larger critical particle size as can be seen in the reduction of the computed $\Delta\widetilde{W}$ at the center of the particle. On the contrary, the strong driving forces between the two unstable equilibrium positions are pushing the dislocation towards the center of the particle. Consequently the non-equilibrium state is accommodated with a much larger negative change of the system energy for the dislocation generation, thus stabilizing the dislocation for smaller particles than in the equilibrium state. This also means that the utilization of a sharp interface model as in [27] would lead to an underestimation of the critical particle size. Note that the driving force on the phase boundary is non-zero at the first time step $\tilde{t} = 14.2$ s. However, the redistribution of the concentration is along the $\tilde{x}_2$ direction and so the driving force on the phase boundary is in the $\tilde{x}_2$ direction and does not contribute to the analysis of the driving force on the dislocation in the $\tilde{x}_1$ direction.

LFP/FP has a distinct difference in the stiffness tensor between the LFP and the FP phase. However, most of previous phase-field simulations ignored the jump in the elasticity across the interface and simply assumed a homogeneous stiffness tensor [117, 134, 129]. This is a motivation to study the influence of the stiffness tensor on the simulation results and how it affects the predicted critical particle size. As an example a particle size of $52.5\,\mathrm{nm}$ is chosen and computed in two variants defining a homogeneous stiffness tensor for both

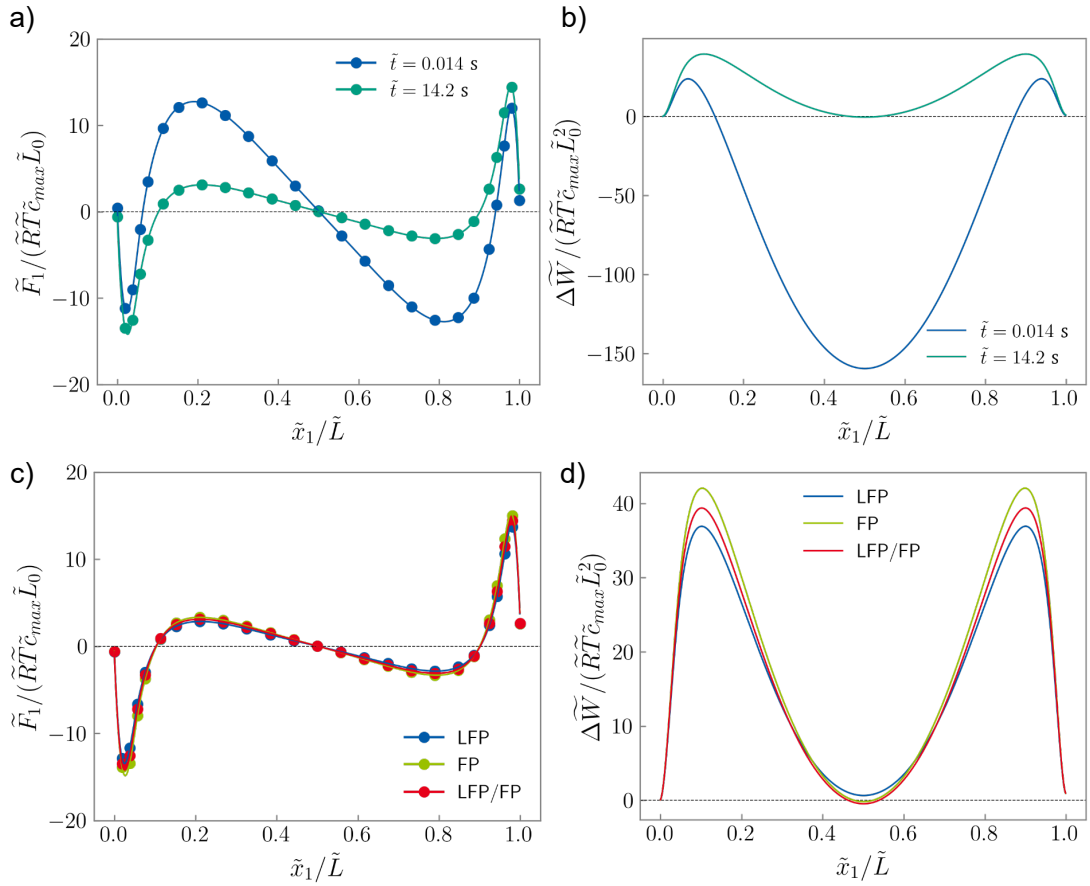

Figure 5.10: Study of the interface model in equilibrium and non equilibrium and in dependence of phase-specific elastic properties. a) Driving force on the dislocation at different times. Along with the relaxation of the interface from the first time step at $\tilde{t} = 0.014$ s to the equilibrium state at $\tilde{t} = 14.4$ s the driving force decreases. This results in a larger critical particle size at the early non-equilibrium state, as shown in the change of the system energy in b). The different influence of the homogeneous stiffness tensor and phase-specific stiffness tensor is shown in c) on the driving force on the dislocation and in d) on the change of the system energy for the formation of the misfit dislocation. The difference in the predicted critical particle size is negligible for the three cases.

phases with either the properties of the FP phase (FP) or the LFP phase (LFP). This is then compared to the result where a phase-specific stiffness tensor was defined (LFP/FP). The results are summarized in figure 5.10c and d. It can be seen that the stiffness tensor has a small influence on the driving forces and the change of the system energy for misfit dislocation formation. In particular a homogeneous stiffness tensor from the LFP phase leads to an underestimation and a homogeneous stiffness tensor from the FP phase leads to an overestimation of the critical particle size, respectively. However, the differences are small compared to other factors as the relaxation of the stress field of the phase boundary and the core parameter $\tilde{h}$, and can be thus neglected. This indicates that results from this work with a phase-specific stiffness tensor can be compared to other results that utilize a homogeneous stiffness tensor.

The dislocation core width is described by the parameter $\tilde{h}$ that determines the relation between the elastic energy and the core energy of the dislocation. It also relates to the stress magnitude in the dislocation core region, as shown in figure 2.8 for isotropic material. In general, a smaller dislocation core width leads to a larger stress field in the core region and a larger elastic energy. The correct core width can be found with an atomistic simulation. This is out of the scope within this work and a discussion on the influence of the dislocation core width on the prediction of the critical particle size is presented here instead. As suggested by Cai et al. [12], a prudent choice for the dislocation core width $\tilde{h}$ is a few Burgers vectors.

The largest driving forces on dislocations are found on the surface, declaring this region crucial to determine the free energy change for the dislocation introduction. In particular the driving forces at the surface is due to the large image forces which are, at those small distances to the surface, related to the stresses in the dislocation core region. This section is dedicated to the characteristics of the chosen description of the dislocation core. In the numerical computations the surface near dislocations are positioned with distances of multiple $h/2$ from the surface. This ensures that one dislocation has the distance of exactly one core width from the free surface which reduces interpolation differences so that the influence of the surface is comparable between different chosen core widths. A series of experiments is conducted varying the core parameter in the range $\tilde{h} \in [1.5, 3.0]$. The results are shown in figure 5.11. The hydrostatic stress shown in figure 5.11a decreases with increasing core width, which results in a decreasing critical particle size $\tilde{L}_c$ with increasing core width as shown in figure 5.11b. The computed driving force on the dislocation and the change of the system energy are analyzed for different core widths in figure 5.11c and d. It can be observed that the driving force close to the particle surface is strongly depending on the core width, especially the points with maximum driving force increase with smaller core width. The driving force on the dislocation between the two

unstable equilibrium positions is almost independent on the core width and the points of zero driving force are shifting slightly towards the center for smaller core width. The analysis of the change in the system energy shows that the increase of the core width leads to a more stable dislocation and a smaller critical particle size. The computed critical particle size for $h = 2$ is $\tilde{L}_c = 52.5$ nm. In particular, a smaller core width leads to a larger increase in the system energy change in the region close to the surface reaching a higher maximum, and thus a larger energy barrier for the formation of a misfit dislocation. Interestingly, the shape of the curve between the points of maximum $\Delta\widetilde{W}$ is invariant to the core width. Therefore the dependence of the critical particle size on the core width is related to the interaction of the dislocation with the surface.

In the energy based dislocation formation criterion, the work required for a dislocation gliding into the particle is proportional to the dislocation self energy. In the dislocation model the dislocation self energy is determined by the dislocation core width, where a larger core energy is related to a smaller core width. Therefore the reduction of the predicted critical particle size with the increase of the dislocation core width can be explained with the reduction of the dislocation self energy. Further the large range of the predicted critical particle sizes suggests the core width to be a crucial parameter for the prediction of the critical particle size and a correct definition of the dislocation core width is crucial. In the benchmark for the driving force on a dislocation in a sheared particle in chapter 2.5.6 the driving force on the dislocation was shown to not be influenced by the choice of the dislocation core parameter. Thus, the difference of the predicted critical particle size for different dislocation core widths should be only caused by the difference in the dislocation core energy. This was also observed in the work of Esmizadeh and Haftbaradaran [27], where the classical singular dislocation theory is applied and a cut-off radius at the order of the Burgers vector is utilized to adjust the dislocation core energy.

In the phase field model proposed in this work the interface is modeled with the Khachaturyan model [54]. The model was chosen over others based on the Voigt/Taylor or Reuss/Sachs homogenization schemes [5]. For these models a generation of extra interface energy was found so that the inhomogeneity force and the stress field at the transition region across the interface is not computed accurately [23, 108]. An interface model with accurate mechanical behavior has to be consistent with the interface equilibrium conditions satisfied with a sharp interface model [116]. The continuity of the stress vector at the interface and the kinematic compatibility is fulfilled by the variational approach proposed by Mosler et al. [88]. This is also known as the mechanical jump conditions at the phase boundary, that is a force balance in the normal direction and the Hadamard condition in the tangential direction of the interface, as discussed in the model proposed by Schneider et al. [107, 106, 108]. The shear stress caused by the misfit strain at the

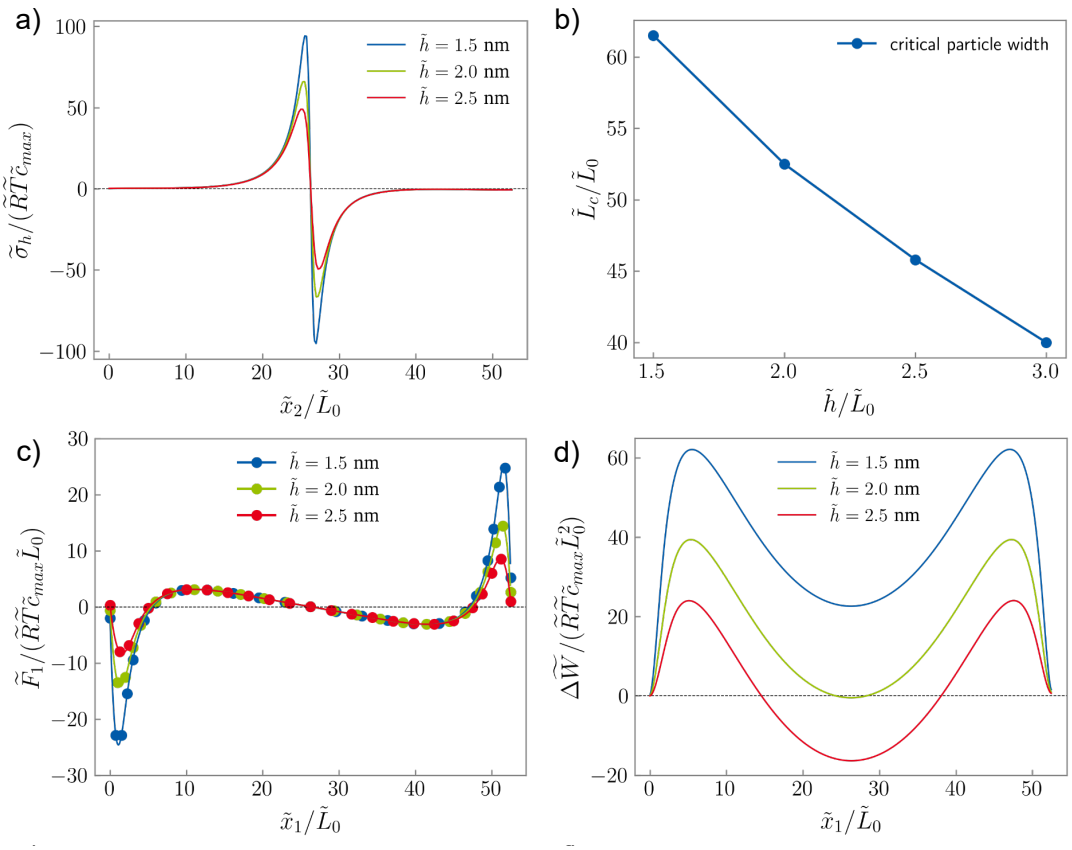

Figure 5.11: Influence of the dislocation core width on the determination of the critical particle size. a) Distribution of the hydrostatic stress across the dislocation core for different dislocation core widths. b) Dependence of the critical particle width on the dislocation core width with and without cut-off radius $\tilde{r}_c = \tilde{h}$. c,d) Driving force $\widetilde{F}_1$ on the misfit dislocation and change of the system energy $\Delta\widetilde{W}$ for different dislocation core widths computed for the particle size $L = 52.5$ nm.

interface was identified to cause a driving force on the dislocation in section 5.2 and is thus a crucial factor in determining the dislocation stability and thus the critical particle size. A correct mechanical jump condition could improve the accuracy of the strain and stress computation in the phase field model. However, the formulation and application of Schneider's model are simplified for isotropic materials [109, 119]. Nevertheless it is promising to extend Schneider's model for orthotropic materials to improve further analysis of the stability of misfit dislocations in LFP particles in the future.

Some limitations of the numerical studies in this work originating from the assumptions within the model remain to be discussed. The driving force on the misfit dislocation was computed assuming a plane strain problem and isotropic surface energy, although the interface energy for LFP particles was found to be highly anisotropic [1]. The assumption of plane strain problems results in an incorrect prediction of the stress in the out-of-plane direction related to the anisotropic inelastic strain gradient across the interface between the LFP and FP phases. Although this stress does not raise a Peach-Koehler force of the dislocation, the anisotropic interface energy is not the same in three-dimensional space so that an influence on the concentration distribution and the stress field in the phase boundary region can be expected. Therefore a three-dimensional simulation with an anisotropic interface energy coefficient may be a more accurate tool for the stability analysis of misfit dislocations. Further the anisotropic diffusivity of LFP particles [79] was simplified to isotropic diffusivity. This last simplification does not influence the predictions in this work since all cases considered the equilibrium state. However, for the analysis of phase transformations, for example in the charging or discharging process, an anisotropic definition of the diffusivity is necessary.

6 Conclusion and Outlook

Conclusion

A chemo-mechanical phase-field model combined with a non-singular continuum dislocation theory was developed, where the dislocation was introduced in the model in the form of an eigenstrain distribution derived from a non-singular continuum dislocation model. The generalized configurational force theory for dislocations in mechanically coupled phase transformation problems was proposed. The model was numerically implemented in the finite element method based on a mixed formulation of the diffusion equation. The model was applied to study the interaction of lithium ions and dislocations in battery materials. In particular, diffusion, mobility, and phase separation were studied in isotropic spinel $LiMn_2O_4$. The configurational mechanics was applied in formulating an energy based formation criterion of misfit dislocations to study the critical particle size for stable dislocations in two-phase anisotropic $LiFePO_4$.

To benchmark the linear elastic continuum dislocation model, the stress fields of an edge and a screw dislocation were numerically computed, showing good agreement with the analytic solution. The driving forces computed within the configurational mechanics were benchmarked by comparison to the Peach-Koehler force. First, the configurational force on a dislocation within a particle subject to shear stress was computed, where the deviation to the Peach-Koehler force was around $1\,\%$. Then for a dislocation within a free standing particle close to a free surface, the resulting driving forces depending on the distance to the free surface were analyzed. The configurational forces were computed numerically with the chemo-mechanical model and the analytical driving force were calculated resulting from the stress field of an image dislocation constructed at the free surface. The results show good agreement in distances from the dislocation surfaces larger than the dislocation core width $\tilde{h}$. The image force in the classical solution has a singularity at the free surface. The non-singular analytical solution and the numerical solution show qualitative agreement with a maximum near the free surface and zero driving forces at the

surface. The driving force component F_1 was integrated along the glide plane to obtain the change of the free energy ΔW upon introduction of the dislocation into the particle showing good qualitative agreement between the different solutions.

The chemo-mechanical model for dislocated solids proposed in this work was validated by a series of benchmarks. The influence of the mechanics on the phase separation was analyzed in a dislocation-free sample, comparing the phase separation computed with the non-coupled and the coupled model. It was found that the stress results in a distinct widening of the interface compared to the classical spinodal decomposition described by the Cahn-Hilliard equation. The equilibrium concentration of ions in the vicinity of an edge dislocation was computed and compared to an analytically calculated concentration distribution in the equilibrium state. The benchmark for the edge dislocation close to a free surface was further extended to cover the chemo-mechanically coupling, where the analytical solution was extended by linear addition of the numerically computed misfit strain on the interface. The numerically computed driving force was significantly smaller than the analytically calculated image force but shows qualitative agreement. The change in the system energy was similar.

The influence of dislocations on diffusion and ion mobility was studied with the chemo-mechanical model for dislocated solids. For the example of a single dislocation in a free standing particle, the influence of the dislocation stress field on the diffusion of lithium ions was analyzed. It was shown that the concentration increased in the tensile region and decreased in the compressive region and the enrichment or depletion of concentration was SOC dependent. Symmetry was observed with respect to SOC $= 0.5$, where a dominant enrichment was found for larger SOC and a dominant depletion for lower SOC. The relative change of the concentration due to the dislocation most substantial at low SOC supporting the experimental observation of a more decisive influence of the dislocation on the diffusion observed at low SOC. The diffusion-induced stress tends to reduce the stress field of the dislocation and was also found to be SOC-dependent with a similar symmetry respective to the SOC with a maximum reduction at SOC $= 0.5$. The maximum absolute DIS was found to be at SOC < 0.5 in the tensile region and at SOC > 0.5 in the compressive region of the edge dislocation. The potentiostatic and galvanostatic charging of a particle with a single dislocation was simulated. An influence of the dislocation on the concentration distribution was found, where the overall and average charging stage was similar to an equivalent dislocation-free particle. The mobility in the vicinity of an edge dislocation was analyzed in terms of homogenization. The mobility around the dislocation core has shown obvious SOC dependence with a maximum at an SOC $= 0.5$, and the tensile and compressive sides of the region near the dislocation core introduced mobility heterogeneity. However, the average mobility was equivalent to a dislocation-free material,

and the existence of the dislocation did not introduce apparent mobility anisotropy in the bulk material. The dislocation array introduced large areas with enhanced tensile and compressive stress, which resulted in a strong SOC heterogeneity in the material. The mobility has contributions from a mixing term. and an elastic term, where ignoring the first leads to an underestimation of the mobility and ignoring the latter leads to an overestimation of the mobility. Three-dimensional simulations of the diffusion along the edge dislocation line were performed where different diffusion coefficients were considered inside the dislocation core region. The result has shown the formation of a fast diffusion path initiated on the tensile side of the edge dislocation core.

The chemo-mechanical model for dislocated solids was then adopted to study dislocations in phase separation problems. First, the interaction between the diffusive ions and a dislocation in a phase separation model was studied in isotropic $LiMn_2O_4$. For that, the influence of the core width on the concentration redistribution and respective diffusion induced stress around a single dislocation was analyzed. The redistribution and the related diffusion-induced stress were found to be stronger for a smaller core width, where the core width $\tilde{h} = 1$ resulted in concentrations close to $c = 0$ and $c = 1$. The phase separation with a dislocation was shown with its dependence on the SOC and the interaction parameter χ. For $\chi \leq 2.5$, the distribution of the high concentration and the low concentration phase followed the tensile and compressive side of the dislocation, respectively. The charging of a particle considering phase separation was shown with and without dislocation. It was found that the dislocation had a pinning effect when the interface is close to the dislocation.

Then the phase separation model was applied to study the stability of misfit dislocations in two-phase LFP particles with anisotropic elasticity. Sufficient parameters were found with a study on the influence of the mesh resolution and the simulation time regarding the equilibrium state. Separately the interface relaxation with and without dislocation was studied. A distinct reduction of the stresses $\widetilde{\sigma}_{12}$ and $\widetilde{\sigma}_h$ between the initial and the equilibrium state was observed. The configurational forces were computed for misfit dislocations at a relaxed interface in equilibrium. First, the resulting driving forces F_1 and the change of the system energy upon introduction of the dislocation into the material were studied in a single square-shaped two-phase particle. Three equilibrium positions with zero driving force on the dislocation were found, where the one in the center of the phase boundary was identified as a stable equilibrium position and the other two near the free surface as unstable equilibrium positions. The unstable equilibrium positions coincided with a maximum system energy change which determined the energy barrier to introduce misfit dislocations. For the assumed circumstances and given model parameters, a minimum particle size for stable misfit dislocations of $\tilde{L}_c = 52.5$ nm was found and

defined as critical particle size. Different particle shapes were studied in the sense of an aspect ratio. It was found that the shear stress $\widetilde{\sigma}_{12}$ increased with the aspect ratio. The driving force F_1 and the change of the system energy were analyzed, which suggests a stabilizing of the dislocation with an increasing aspect ratio. The critical particle width decreased with increasing aspect ratio, where the largest difference was between $a = 1$ and $a = 1.5$ and saturation was found for $a \geq 2.5$. Further particles with an aspect ratio of $a = 1.5$ can be pointed out due to the largest predicted critical specific surface area. Concluding the critical particle size was analyzed in dependence of the position of the interface and the dislocation. In general, a deviation of the interface position from the center of the particle was found to destabilize the misfit dislocation, so that the critical particle size could be found with the interface in the particle center. The deviation for the aspect ratio $a = 1$ was negligible, and an asymmetry due to the difference of the interface position in the positive and negative direction was related to the elasticity of the different phases. On the extreme positions close to the surface, bending and curving of the interface occurred, so that these positions were excluded from the analysis.

Conclusively, the effects of some essential model parameters were discussed. First, the influence of the relaxation of the interface was studied by comparing the first timestep with the equilibrium state. In the first timestep, a larger critical particle size was predicted. Thus interface relaxation resulted in a significantly smaller critical particle size compared to a non-relaxed interface. Ignoring the interface relaxation would lead to a wrong estimation of the critical particle size. The elasticity was implemented by defining the elasticity tensor as a function of the concentration, thereby assigning the elastic properties to the respective phases. The results for this phase-sensitive stiffness tensor were compared to results implementing a constant stiffness tensor, where the properties of FP and LFP were applied in separate examples. It was found that the constant stiffness tensors only lead to small differences in the driving forces and prediction of the critical particle size in comparison to the phase-sensitive stiffness tensor. Finally, the influence of the description of the dislocation core on the results was studied. A decreased core width lead to an increase in the hydrostatic stress field. In the driving forces, the decreased core width resulted in an increase of the driving forces around the maxima close to the surface. From that, a larger critical particle size was predicted for a smaller core width, e.g., the decreasing core width destabilized the misfit dislocation. In summary, the driving forces on the dislocation were most strong close to the surface and were affected the most by the description of the dislocation core. Therefore this region, in combination with the dislocation core model, is most critical for an accurate prediction of the critical particle size.

Outlook

The presented model provides a physically meaningful non-singular stress and strain field of dislocations considering the chemo-mechanical influence depending on the SOC formulated for two dimensions and three dimensions. The here presented work can be continued to further improve the understanding of real dislocations in electrode materials.

The general nature of FEM allows simulating electrode particles in arbitrary shapes, under complex boundary conditions, in three dimensions, and including multiple dislocations up to dislocation networks. The free energy approach allows implementation of the contributions of non-dislocation defects to the free energy so that the interaction of dislocations with other defects, such as inclusions or cracks, can be studied. Another example would be the inclusion of an electrostatic contribution to the free energy to study, for instance, charged dislocation cores.

Within this framework, the interaction of dislocation with impurity atoms can be studied. Conclusions can be drawn on the respective concentration fields and their effect on the elastic energy of dislocations. This would allow predictions on the influence of doping on dislocation stability. The presented model can also be applied to various isotropic and anisotropic cathode materials to better understand concentration distribution and stress development related to dislocations.

The dislocation was found to have no overall influence on the SOC during the charging process compared to a dislocation-free particle. However, it would be interesting to study the influence of the dislocation on the battery performance during cycling. For this, the model can be extended to large stresses and plastic deformation and a model that captures the damage of the material, e.g. [7]. This could shed light on the unknown dynamic relationships between the SOC and dislocation influence during the charging and discharging processes.

Accurate computation of the dislocation displacement and stress fields requires a mesh size in the range of the dislocation core radius, which is a bottleneck toward large-scale simulations. One solution for this can be a locally refined mesh around the dislocation to enlarge the volume without increasing the computation cost. Such a locally refined mesh is most efficient for large volumes and low dislocation densities.

The phase separation model can be improved in accuracy as the jump conditions were simplified [54]. The correct jump conditions were described for isotropic materials in [107, 106, 108]. Extending this model to orthotropic material properties can lead to a more

accurate prediction of the critical particle size. It is straightforward to extend the model with anisotropic diffusivity and interface energy, given that the respective parameters are known from experiments or first-principles calculations.

Local heterogeneous mobility is interesting for dynamic analysis of dislocation movement. The local concentration is needed to calculate how the concentration field can follow the dislocation movement. It would be interesting to analyze the movement of dislocations interacting with the evolution of concentration fields influenced by internal and external stresses during the charging and discharging of battery particles. The configurational mechanics presented in this work is suitable for computing driving forces on dislocations in chemo-mechanically coupled systems. The model can be extended following existing dynamic dislocation phase field models [48, 87] to predict the dislocation movement.

The stability criterion formulated for misfit dislocations can be extended to a nucleation criterion at a real surface of the particle. By the estimation of the required work for the surface nucleation of dislocations and considering extensions for a dynamic dislocation model, including release of elastic energy due to dislocation nucleation and movement, resulting stresses from the DIS during charging and discharging can be translated into non-elastic deformation related to dislocations. In multiple particle systems the stress state and particle orientation can then be applied to predict the stability of dislocations and lead to conclusions on dislocation densities.

Bibliography

[1] A. Abdellahi et al. “Particle-size and morphology dependence of the preferred interface orientation in LiFePO 4 nano-particles”. In: *Journal of Materials Chemistry A* 2.37 (2014), pp. 15437–15447.

[2] E. Agiasofitou and M. Lazar. “Electro-elastic dislocations in piezoelectric materials”. In: *Philos. Mag.* 100.9 (2020), pp. 1059–1101.

[3] E. Agiasofitou and M. Lazar. “Micromechanics of dislocations in solids: J-, M-, and L-integrals and their fundamental relations”. In: *International Journal of Engineering Science* 114 (2017), pp. 16–40.

[4] H. Y. Amanieu et al. “Mechanical property measurements of heterogeneous materials by selective nanoindentation: Application to LiMn2O4 cathode”. In: *Materials Science and Engineering A* 593 (2014), pp. 92–102. DOI: 10.1016/j.msea.2013.11.044.

[5] K. Ammar, B. Appolaire, G. Cailletaud, and S. Forest. “Combining phase field approach and homogenization methods for modelling phase transformation in elastoplastic media”. In: *European Journal of Computational Mechanics/Revue Européenne de Mécanique Numérique* 18.5-6 (2009), pp. 485–523.

[6] Y. Bai, Y. Zhao, W. Liu, and B.-X. Xu. “Two-level modeling of lithium-ion batteries”. In: *Journal of Power Sources* 422 (2019), pp. 92–103.

[7] Y. Bai et al. “A chemo-mechanical grain boundary model and its application to understand the damage of Li-ion battery materials”. In: *Scripta Materialia* 183 (2020), pp. 45–49. DOI: https://doi.org/10.1016/j.scriptamat.2020.03.027.

[8] K. P. Baxevanakis and A. E. Giannakopoulos. “Finite element analysis of discrete edge dislocations: configurational forces and conserved integrals”. In: *Int. J. Solids Struct.* 62 (2015), pp. 52–65.

[9] L. Y. Beaulieu et al. “Colossal reversible volume changes in lithium alloys”. In: *Electrochemical and Solid-State Letters* 4.9 (2001), pp. 7–10. DOI: 10.1149/1.1388178.

[10] J. W. Cahn and S. M. Allen. “A Microscopic Theory for Domain Wall Motion and Its Experimental Verification in Fe-Al Alloy Domain Growth Kinetics”. In: *J Phys (Paris) Colloq* 38 Colloq C-7.12 (1977). DOI: 10.1051/jphyscol:1977709.

[11] J. W. Cahn and J. E. Hilliard. “Free energy of a nonuniform system. I. Interfacial free energy”. In: *The Journal of Chemical Physics* 28.2 (1958), pp. 258–267. DOI: 10.1063/1.1744102.

[12] W. Cai, A. Arsenlis, C. R. Weinberger, and V. V. Bulatov. “A non-singular continuum theory of dislocations”. In: *J. Mech. Phys. Solids* 54.3 (2006), pp. 561–587. DOI: 10.1016/j.jmps.2005.09.005.

[13] W. Cai and W. D. Nix. *Imperfections in crystalline solids*. Cambridge University Press, 2016.

[14] B. Chen, J. Zhou, J. Zhu, and Z. Liu. “Diffusion induced stress and the distribution of dislocations in a nanostructured thin film electrode during lithiation”. In: *RSC advances* 4.109 (2014), pp. 64216–64224.

[15] J. Chen-Min Li. “Physical chemistry of some microstructural phenomena”. In: *Metall. Trans. A* 9.10 (1978), pp. 1353–1380. DOI: 10.1007/bf02661808.

[16] J. Christensen and J. Newman. “A mathematical model of stress generation and fracture in lithium manganese oxide”. In: *Journal of The Electrochemical Society* 153.6 (2006), A1019.

[17] E. Clouet. “The vacancy-edge dislocation interaction in fcc metals: A comparison between atomic simulations and elasticity theory”. In: *Acta Materialia* 54.13 (2006), pp. 3543–3552. DOI: 10.1016/j.actamat.2006.03.043.

[18] D. A. Cogswell and M. Z. Bazant. “Coherency strain and the kinetics of phase separation in LiFePO 4 nanoparticles”. In: *ACS Nano* 6 (3 2012), pp. 2215–2225. DOI: 10.1021/nn204177u.

[19] S. Das et al. “Probing the pseudo-1-D ion diffusion in lithium titanium niobate anode for Li-ion battery”. In: *Phys. Chem. Chem. Phys.* 18.32 (2016), pp. 22323–22330. DOI: 10.1039/c6cp04488c.

[20] L. R. De Jesus et al. “Lithiation across interconnected V 2 O 5 nanoparticle networks”. In: *Journal of Materials Chemistry A* 5.38 (2017), pp. 20141–20152.

[21] R. DeWit. “Theory of Disclinations - 2. Continuous and Discrete Disclinations in Anisotropic Elasticity.” In: *J Res Nat Bur Stand Sect A Phys Chem* 77 A.1 (1973), pp. 49–100. DOI: 10.6028/jres.077a.024.

[22] C. V. Di Leo, E. Rejovitzky, and L. Anand. “Diffusion-deformation theory for amorphous silicon anodes: the role of plastic deformation on electrochemical performance”. In: *Int. J. Solids Struct.* 67-68 (2015), pp. 283–296. DOI: 10.1016/j.ijsolstr.2015.04.028.

[23] A. Durga, P. Wollants, and N. Moelans. “A quantitative phase-field model for two-phase elastically inhomogeneous systems”. In: *Computational Materials Science* 99 (2015), pp. 81–95.

[24] J. D. Eshelby. “Energy relations and the energy-momentum tensor in continuum mechanics”. In: *Inelastic behavior of solids (ed. MF Kanninen)* (1970), pp. 77–115.

[25] J. D. Eshelby. “The force on an elastic singularity”. In: *Philosophical Transactions of the Royal Society of London. Series A, Mathematical and Physical Sciences* 244.877 (1951), pp. 87–112.

[26] S. Esmizadeh and H. Haftbaradaran. “A model for predicting critical size for dislocation formation in phase transforming planar particles of energy storage intercalation materials”. In: *Journal of the Mechanics and Physics of Solids* 133 (2019), p. 103739.

[27] S. Esmizadeh and H. Haftbaradaran. “An energy-based stability analysis of misfit dislocations in two-phase electrode particles: A planar model and implications for LiFePO4”. In: *International Journal of Mechanical Sciences* 183 (2020), p. 105812.

[28] Y. Estrin. “Dislocation theory based constitutive modelling: foundations and applications”. In: *Journal of Materials Processing Technology* 80 (1998), pp. 33–39.

[29] H. Gabrisch, J. Wilcox, and M. M. Doeff. “TEM study of fracturing in spherical and plate-like LiFePO4 particles”. In: *Electrochemical and Solid State Letters* 11.3 (2008), A25.

[30] M. Garbrecht et al. “Dislocation-pipe diffusion in nitride superlattices observed in direct atomic resolution”. In: *Scientific Reports* 7 (2017), p. 46092.

[31] W. E. Gent et al. “Persistent State-of-Charge Heterogeneity in Relaxed, Partially Charged Li1- xNi1/3Co1/3Mn1/3O2 Secondary Particles”. In: *Advanced materials* 28.31 (2016), pp. 6631–6638.

[32] N. M. Ghoniem and L. Z. Sun. “Fast-sum method for the elastic field of three-dimensional dislocation ensembles”. In: *Phys. Rev. B* 60.1 (1999), p. 128.

[33] H. Gomez and T. J. Hughes. “Provably unconditionally stable, second-order time-accurate, mixed variational methods for phase-field models”. In: *Journal of Computational Physics* 230.13 (2011), pp. 5310–5327.

[34] D. Gross, S. Kolling, R. Mueller, and I. Schmidt. “Configurational forces and their application in solid mechanics”. In: *European Journal of Mechanics-A/Solids* 22.5 (2003), pp. 669–692.

[35] D. Gross and T. Seelig. *Fracture Mechanics with an Introduction to Micromechanics*. 2nd ed. Springer, Berlin, Heidelberg, 2011, pp. X, 336. DOI: https://doi.org/10.1007/978-3-642-19240-1.

[36] E. A. Guggenheim. *Mixtures : the theory of the equilibrium properties of some simple classes of mixtures solutions and alloys*. The International series of monographs on physics. Oxford: Clarendon Press, 1952.

[37] M. E. Gurtin. *Configurational forces as basic concepts of continuum physics*. Vol. 137. Springer Science & Business Media, 1999.

[38] M. Y. Gutkin and E. C. Aifantis. “Dislocations and disclinations in gradient elasticity”. In: *physica status solidi (b)* 214.2 (1999), pp. 245–284.

[39] Y. Gwak, J. Moon, and M. Cho. “Multi-scale analysis of an electrochemical model including coupled diffusion, stress, and nonideal solution in a silicon thin film anode”. In: *Journal of Power Sources* 307 (Mar. 2016), pp. 856–865. DOI: 10.1016/j.jpowsour.2016.01.037.

[40] H. Haftbaradaran and J. Qu. “Two-dimensional chemo-elasticity under chemical equilibrium”. In: *International Journal of Solids and Structures* 56 (2015), pp. 126–135. DOI: 10.1016/j.ijsolstr.2014.11.025.

[41] H. Haftbaradaran, J. Song, W. Curtin, and H. Gao. “Continuum and atomistic models of strongly coupled diffusion, stress, and solute concentration”. In: *Journal of Power Sources* 196.1 (2011), pp. 361–370.

[42] S. Han, J. Park, W. Lu, and A. M. Sastry. “Numerical study of grain boundary effect on Li+ effective diffusivity and intercalation-induced stresses in Li-ion battery active materials”. In: *Journal of Power Sources* 240 (2013), pp. 155–167.

[43] J. P. Hirth and J. Lothe. *Theory of dislocations*. 2nd. Krieger Publishing, 1982.

[44] Y. K. Ho and P. L. Pratt. “Dislocation pipe diffusion in sodium chloride crystals”. In: *Radiation Effects* 75.1-4 (1982), pp. 183–192. DOI: 10.1080/00337578308224700.

[45] M. Höfling et al. “Control of polarization in bulk ferroelectrics by mechanical dislocation imprint”. In: *Science* 372.6545 (2021), pp. 961–964. DOI: 10.1126/science.abe3810.

[46] L. Hong, K. Yang, and M. Tang. “A mechanism of defect-enhanced phase transformation kinetics in lithium iron phosphate olivine”. In: *npj Computational Materials* 5.1 (2019), pp. 1–9. DOI: 10.1038/s41524-019-0255-3.

[47] J. Hornstra. “Dislocations, stacking faults and twins in the spinel structure”. In: *Journal of Physics and Chemistry of Solids* 15.3-4 (1960), pp. 311–323.

[48] S. Hu and L. Chen. “Solute segregation and coherent nucleation and growth near a dislocation—a phase-field model integrating defect and phase microstructures”. In: *Acta Materialia* 49.3 (2001), pp. 463–472. DOI: 10.1016/S1359-6454(00)00331-1.

[49] Y. Hu, X. Zhao, and Z. Suo. “Averting cracks caused by insertion reaction in lithium–ion batteries”. In: *Journal of Materials Research* 25.6 (2010), pp. 1007–1010.

[50] J. Y. Huang et al. “In situ observation of the electrochemical lithiation of a single SnO_2 nanowire electrode”. In: *Science* 330.6010 (2010), pp. 1515–1520. DOI: 10.1126/science.1195628.

[51] T. Ichitsubo et al. “What determines the critical size for phase separation in LiFePO 4 in lithium ion batteries?” In: *Journal of Materials Chemistry A* 1.46 (2013), pp. 14532–14537.

[52] O. Jamond, R. Gatti, A. Roos, and B. Devincre. “Consistent formulation for the discrete-continuous model: improving complex dislocation dynamics simulations”. In: *Int. J. Plasticity* 80 (2016), pp. 19–37. DOI: 10.1016/J.IJPLAS.2015.12.011.

[53] S. Jeon et al. “Particle size effects on dislocation density, microstructure, and phase transformation for high-entropy alloy powders”. In: *Materialia* 18 (Aug. 2021). DOI: 10.1016/j.mtla.2021.101161.

[54] A. G. Khachaturyan. “Theory of structural transformation in solids”. In: (1983).

[55] D.-H. Kim and J. Kim. “Synthesis of LiFePO4 nanoparticles in polyol medium and their electrochemical properties”. In: *Electrochemical and Solid State Letters* 9.9 (2006), A439.

[56] Y. Kim. “Point Defects in Layer-Structured Cathode Materials for Lithium-Ion Batteries”. In: *Journal of Physical Chemistry C* 120.8 (2016), pp. 4173–4182. DOI: 10.1021/acs.jpcc.5b09301.

[57] P. Kontis et al. “The effect of chromium and cobalt segregation at dislocations on nickel-based superalloys”. In: *Scripta Materialia* 145 (2018), pp. 76–80.

[58] E. Kossecka. “Mathematical theory of defects. part I. Statics”. In: *Arch. Mech.* 26 (1975), pp. 995–1010.

[59] M. Lazar. “Peach-Koehler forces within the theory of nonlocal elasticity”. In: (2005). DOI: 10.48550/ARXIV.COND-MAT/0501732.

[60] M. Lazar. “The fundamentals of non-singular dislocations in the theory of gradient elasticity: Dislocation loops and straight dislocations”. In: *International Journal of Solids and Structures* 50.2 (2013), pp. 352–362. DOI: 10.1016/J.IJSOLSTR.2012.09.017.

[61] M. Lazar and H. O. K. Kirchner. “Dislocation loops in anisotropic elasticity: displacement field, stress function tensor and interaction energy”. In: *Philos. Mag.* 93.1-3 (2013), pp. 174–185.

[62] M. Lazar and H. O. K. Kirchner. “The Eshelby stress tensor, angular momentum tensor and dilatation flux in gradient elasticity”. In: *International Journal of Solids and Structures* 44.7-8 (2007), pp. 2477–2486.

[63] M. Lazar and G. A. Maugin. “Nonsingular stress and strain fields of dislocations and disclinations in first strain gradient elasticity”. In: *International Journal of Engineering Science* 43.13-14 (2005), pp. 1157–1184. DOI: 10.1016/J.IJENGSCI.2005.01.006.

[64] L. Le Cam. “The central limit theorem around 1935”. In: *Statistical Science* 1.1 (1986), pp. 78–91. DOI: 10.1214/ss/1177013818.

[65] M. Legros, G. Dehm, E. Arzt, and T. J. Balk. “Observation of giant diffusivity along dislocation cores”. In: *Science* 319.5870 (2008), pp. 1646–1649. DOI: 10.1126/science.1151771.

[66] F. Léonard and R. C. Desai. “Spinodal decomposition and dislocation lines in thin films and bulk materials”. In: *Physical Review B - Condensed Matter and Materials Physics* 58.13 (1998), pp. 8277–8288. DOI: 10.1103/PhysRevB.58.8277.

[67] V. I. Levitas and M. Javanbakht. “Interaction between phase transformations and dislocations at the nanoscale. Part 1. General phase field approach”. In: *Journal of the Mechanics and Physics of Solids* 82 (July 2015), pp. 287–319. DOI: 10.1016/j.jmps.2015.05.005.

[68] J. Li, Q. Fang, F. Liu, and Y. Liu. “Analytical modeling of dislocation effect on diffusion induced stress in a cylindrical lithium ion battery electrode”. In: *Journal of Power Sources* 272 (2014), pp. 121–127.

[69] J. Li et al. “Dynamics of particle network in composite battery cathodes”. In: *Science* 376.6592 (2022), pp. 517–521. DOI: 10.1126/science.abm8962.

[70] Q. Li et al. “Dynamic imaging of crystalline defects in lithium-manganese oxide electrodes during electrochemical activation to high voltage”. In: *Nat. Commun.* 10.1 (2019), pp. 1–7. DOI: 10.1038/s41467-019-09408-2.

[71] S. Li and G. Wang. *Introduction to Micromechanics and Nanomechanics*. 2nd. WORLD SCIENTIFIC, 2018. DOI: 10.1142/8644.

[72] W. Li, E. M. Erickson, and A. Manthiram. “High-nickel layered oxide cathodes for lithium-based automotive batteries”. In: *Nature Energy* 5.1 (2020), pp. 26–34. DOI: 10.1038/s41560-019-0513-0.

[73] L. Lilensten et al. “Segregation of Solutes at Dislocations: A New Alloy Design Parameter for Advanced Superalloys”. In: *Superalloys 2020*. Springer, 2020, pp. 41–51.

[74] T. Liu et al. “Origin of structural degradation in Li-rich layered oxide cathode”. In: *Nature* 606 (7913 June 2022), pp. 305–312. DOI: 10.1038/s41586-022-04689-y.

[75] W. Liu, K. Kowal, and G. Farrington. “Mechanism of the Electrochemical Insertion of Lithium into LiMn2O4 Spinels”. In: *Journal of the Electrochemical Society* 145.2 (1998), p. 459.

[76] X. H. Liu et al. “Size-dependent fracture of silicon nanoparticles during lithiation”. In: *ACS nano* 6.2 (2012), pp. 1522–1531.

[77] V. A. Lubarda. “Dislocation Burgers vector and the Peach-Koehler force: A review”. In: *Journal of Materials Research and Technology* 8.1 (2019), pp. 1550–1565. DOI: 10.1016/j.jmrt.2018.08.014.

[78] Y. Luo et al. “Effect of crystallite geometries on electrochemical performance of porous intercalation electrodes by multiscale operando investigation”. In: *Nature materials* (2021), pp. 1–11.

[79] R. Malik, D. Burch, M. Bazant, and G. Ceder. “Particle size dependence of the ionic diffusivity”. In: *Nano letters* 10.10 (2010), pp. 4123–4127.

[80] M. Mao et al. “Atomic resolution observation of conversion-type anode RuO_2 during the first electrochemical lithiation”. In: *Nanotechnology* 26.12 (2015). DOI: 10.1088/0957-4484/26/12/125404.

[81] G. A. Maugin. *Material inhomogeneities in elasticity*. CRC Press, 2020.

[82] T. Maxisch and G. Ceder. “Elastic properties of olivine Li x FePO 4 from first principles”. In: *Physical Review B* 73.17 (2006), p. 174112.

[83] N. Meethong et al. “Strain accommodation during phase transformations in olivine-based cathodes as a materials selection criterion for high-power rechargeable batteries”. In: *Advanced Functional Materials* 17.7 (2007), pp. 1115–1123.

[84] H. Mehrer. *Diffusion in solids*. Springer Berlin Heidelberg New York, 2007. DOI: 10.1007/978-3-540-71488-0.

[85] J. Meiser and H. M. Urbassek. “Dislocations help initiate the ensuremath alpha–ensuremath gamma phase transformation in iron—An atomistic study”. In: *Metals* 9 (1 Jan. 2019). DOI: 10.3390/met9010090.

[86] M. P. Mercer et al. “The influence of point defects on the entropy profiles of Lithium Ion Battery cathodes: a lattice-gas Monte Carlo study”. In: *Electrochimica Acta* 241 (2017), pp. 141–152. DOI: 10.1016/j.electacta.2017.04.115.

[87] J. R. Mianroodi et al. “Atomistic phase field chemomechanical modeling of dislocation-solute-precipitate interaction in Ni–Al–Co”. In: *Acta Materialia* 175 (2019), pp. 250–261. DOI: 10.1016/j.actamat.2019.06.008.

[88] J. Mosler, O. Shchyglo, and H. M. Hojjat. “A novel homogenization method for phase field approaches based on partial rank-one relaxation”. In: *Journal of the Mechanics and Physics of Solids* 68 (2014), pp. 251–266.

[89] R. Mueller, D. Gross, and D. C. Lupascu. “Driving forces on domain walls in ferroelectric materials and interaction with defects”. In: *Computational materials science* 35.1 (2006), pp. 42–52.

[90] R. Mueller, S. Kolling, and D. Gross. “On configurational forces in the context of the finite element method”. In: *International Journal for Numerical Methods in Engineering* 53.7 (2002), pp. 1557–1574.

[91] T. Mura. *Micromechanics of Defects in Solids*. Kluwer, Dordrecht, 1987.

[92] K. Nakayama et al. “Dislocation and oxygen-release driven delithiation in Li 2 MnO 3”. In: *Nature communications* 11.1 (2020), pp. 1–7.

[93] A. Nie et al. “Atomic-scale observation of lithiation reaction front in nanoscale SnO_2 materials”. In: *ACS Nano* 7.7 (2013), pp. 6203–6211. DOI: 10.1021/nn402125e.

[94] J. Niu et al. “In situ observation of random solid solution zone in LiFePO4 electrode”. In: *Nano letters* 14.7 (2014), pp. 4005–4010.

[95] M. Ostoja-Starzewski. “Material spatial randomness: From statistical to representative volume element”. In: *Probabilistic Engineering Mechanics* 21.2 (2006), pp. 112–132. DOI: 10.1016/j.probengmech.2005.07.007.

[96] M. Ostoja-Starzewski. “Towards stochastic continuum thermodynamics”. In: *Journal of Non-Equilibrium Thermodynamics* 27.4 (2002), pp. 335–348. DOI: 10.1515/JNETDY.2002.020.

[97] A. Paladino, L. Rubin, and J. Waugh. “Oxygen ion diffusion in single crystal SrTiO3”. In: *Journal of Physics and Chemistry of Solids* 26.2 (1965), pp. 391–397. DOI: 10.1016/0022-3697(65)90168-X.

[98] S. Park et al. “The effect of Fe as an impurity element for sustainable resynthesis of Li[Ni1/3Co1/3Mn1/3]O2 cathode material from spent lithium-ion batteries”. In: *Electrochimica Acta* 296 (2019), pp. 814–822. DOI: 10.1016/j.electacta.2018.11.001.

[99] J. S. Peach, M. and Koehler. “The Forces Exerted on Dislocations and the Stress Fields Produced by Them”. In: *Phys. Rev.* 80.3 (1950), pp. 436–439. DOI: 10.1103/PhysRev.80.436.

[100] C. J. Permann et al. “MOOSE: Enabling massively parallel multiphysics simulation”. In: *SoftwareX* 11 (2020), p. 100430. DOI: https://doi.org/10.1016/j.softx.2020.100430.

[101] G. Po, M. Lazar, D. Seif, and N. Ghoniem. “Singularity-free dislocation dynamics with strain gradient elasticity”. In: *J. Mech. Phys. Solids* 68 (2014), pp. 161–178.

[102] S. Prussin. “Generation and distribution of dislocations by solute diffusion”. In: *J. Appl. Phys.* 32.10 (1961), pp. 1876–1881. DOI: 10.1063/1.1728256.

[103] C. Reimuth et al. “Chemo-mechanical study of dislocation mediated ion diffusion in lithium-ion battery materials”. In: *Journal of Applied Physics* 130.3 (2021), p. 035103. DOI: 10.1063/5.0049502.

[104] K. F. Riley, M. P. Hobson, and S. J. Bence. *Mathematical methods for physics and engineering: a comprehensive guide*. Cambridge university press, 2006.

[105] R. A. Rodríguez et al. “Structural defects in $LiMn_2O_4$ induced by gamma radiation and its influence on the Jahn-Teller effect”. In: *Solid State Ionics* 324.November 2017 (2018), pp. 77–86. DOI: 10.1016/j.ssi.2018.06.007.

[106] D. Schneider et al. “On the stress calculation within phase-field approaches: a model for finite deformations”. In: *Computational Mechanics* 60.2 (2017), pp. 203–217.

[107] D. Schneider et al. “Phase-field elasticity model based on mechanical jump conditions”. In: *Computational Mechanics* 55.5 (2015), pp. 887–901.

[108] D. Schneider et al. “Small strain multiphase-field model accounting for configurational forces and mechanical jump conditions”. In: *Computational Mechanics* 61.3 (2018), pp. 277–295.

[109] E. Schoof et al. “Multiphase-field modeling of martensitic phase transformation in a dual-phase microstructure”. In: *International Journal of Solids and Structures* 134 (2018), pp. 181–194.

[110] A. Singer et al. “Nucleation of dislocations and their dynamics in layered oxide cathode materials during battery charging”. In: *Nature Energy* 3.8 (2018), pp. 641–647.

[111] P. Stein and B.-X. Xu. “3D Isogeometric Analysis of intercalation-induced stresses in Li-ion battery electrode particles”. In: *Computer Methods in Applied Mechanics and Engineering* 268 (2014), pp. 225–244. DOI: 10.1016/J.CMA.2013.09.011.

[112] P. Stein, Y. Zhao, and B.-X. Xu. “Effects of surface tension and electrochemical reactions in Li-ion battery electrode nanoparticles”. In: *J. Power Sources* (2016). DOI: 10.1016/j.jpowsour.2016.09.085.

[113] P. Stein et al. “The influence of anisotropic surface stresses and bulk stresses on defect thermodynamics in $LiCoO_2$ nanoparticles”. In: *Acta Mater.* 159 (2018), pp. 225–240. DOI: 10.1016/j.actamat.2018.07.046.

[114] Y. Su et al. “Riveting Dislocation Motion: The Inspiring Role of Oxygen Vacancies in the Structural Stability of Ni-Rich Cathode Materials”. In: *ACS Applied Materials & Interfaces* 12.33 (2020), pp. 37208–37217.

[115] G. Sun et al. “On the fragmentation of active material secondary particles in lithium ion battery cathodes induced by charge cycling”. In: *Extreme Mechanics Letters* 9.March (2016), pp. 449–458. DOI: 10.1016/j.eml.2016.03.018.

[116] B. Svendsen, P. Shanthraj, and D. Raabe. “Finite-deformation phase-field chemomechanics for multiphase, multicomponent solids”. In: *Journal of the Mechanics and Physics of Solids* 112 (2018), pp. 619–636.

[117] M. Tang, J. F. Belak, and M. R. Dorr. “Anisotropic phase boundary morphology in nanoscale olivine electrode particles”. In: *The Journal of Physical Chemistry C* 115.11 (2011), pp. 4922–4926.

[118] X. Tang, K. P. D. Lagerlöf, and A. H. Heuer. “Determination of pipe diffusion coefficients in undoped and magnesia-doped sapphire (α-Al2O3): A study based on annihilation of dislocation dipoles”. In: *Journal of the American Ceramic Society* 86.4 (2003), pp. 560–65. DOI: 10.1111/j.1151-2916.2003.tb03341.x.

[119] O. Tschukin, D. Schneider, and B. Nestler. “An elasto-chemical phase-field model for isotropic solids”. In: *European Journal of Mechanics-A/Solids* 73 (2019), pp. 181–191.

[120] A. Ulvestad et al. “Topological defect dynamics in operando battery nanoparticles”. In: *Science* 348.6241 (2015), pp. 1344–1347.

[121] E. Van der Giessen and A. Needleman. “Discrete dislocation plasticity: a simple planar model”. In: *Model. Simul. Mater. Sci. Eng.* 3.5 (1995), p. 689.

[122] L. S. de Vasconcelos, R. Xu, and K. Zhao. “Quantitative spatiotemporal Li profiling using nanoindentation”. In: *Journal of the Mechanics and Physics of Solids* 144 (2020), p. 104102.

[123] A. Vattré et al. “Modelling crystal plasticity by 3D dislocation dynamics and the finite element method: the discrete-continuous model revisited”. In: *J. Mech. Phys. Solids* 63 (2014), pp. 491–505.

[124] K. Vikrant, W. Rheinheimer, and R. E. Garcı"a. “Electrochemical drag effect on grain boundary motion in ionic ceramics”. In: *npj computational materials* 6.1 (2020), pp. 1–7.

[125] A. Villani et al. “A fully coupled diffusional-mechanical formulation: numerical implementation, analytical validation, and effects of plasticity on equilibrium”. In: *Arch. Appl. Mech.* (2014), pp. 1647–1664. DOI: 10.1007/s00419-014-0860-z.

[126] C.-C. Wang. “A microstructure analysis of pressureless sintered LiMn2O4 spinel”. PhD thesis. NSYSU, 2004.

[127] J. Wang et al. “Scalable Synthesis of Defect Abundant Si Nanorods for High-Performance Li-Ion Battery Anodes”. In: *ACS Nano* 9.6 (2015), pp. 6576–6586. DOI: 10.1021/acsnano.5b02565.

[128] P. Wei et al. “Effects of dislocation mechanics on diffusion-induced stresses within a spherical insertion particle electrode”. In: *Journal of Materials Chemistry A* 2.4 (2013), pp. 1128–1136.

[129] L. Wu, V. De Andrade, X. Xiao, and J. Zhang. “Phase Field Modeling of Coupled Phase Separation and Diffusion-Induced Stress in Lithium Iron Phosphate Particles Reconstructed From Synchrotron Nano X-ray Tomography”. In: *Journal of Electrochemical Energy Conversion and Storage* 16.4 (2019).

[130] B. Xiao et al. “Revealing the Atomic Origin of Heterogeneous Li-Ion Diffusion by Probing Na”. In: *Advanced Materials* 31.29 (2019), pp. 1–9. DOI: 10.1002/adma.201805889.

[131] B.-X. Xu, D. Schrade, D. Gross, and R. Mueller. “Phase field simulation of domain structures in cracked ferroelectrics”. In: *International Journal of Fracture* 165.2 (2010), pp. 163–173. DOI: 10.1007/s10704-010-9471-z.

[132] P. Yan et al. “Intragranular cracking as a critical barrier for high-voltage usage of layer-structured cathode for lithium-ion batteries”. In: *Nature communications* 8.1 (2017), pp. 1–9.

[133] X. Zhang, W. Shyy, and A. M. Sastry. “Numerical simulation of intercalation-induced stress in Li-ion battery electrode particles”. In: *J. Electrochem. Soc.* 154.10 (2007), A910. DOI: 10.1149/1.2759840.

[134] Y. Zhao, B.-X. Xu, P. Stein, and D. Gross. “Phase-field study of electrochemical reactions at exterior and interior interfaces in Li-ion battery electrode particles”. In: *Computer methods in applied mechanics and engineering* 312 (2016), pp. 428–446.

[135] Y. Zhao et al. “A review on modeling of electro-chemo-mechanics in lithium-ion batteries”. In: *Journal of Power Sources* 413.December 2018 (2019), pp. 259–283. DOI: 10.1016/j.jpowsour.2018.12.011.

[136] Y. Zhao et al. “Modeling of phase separation across interconnected electrode particles in lithium-ion batteries”. In: *RSC advances* 7.65 (2017), pp. 41254–41264.

[137] L. Zhong et al. “Multiple-stripe lithiation mechanism of individual SnO2 nanowires in a flooding geometry”. In: *Physical Review Letters* 106.24 (2011), pp. 18–21. DOI: 10.1103/PhysRevLett.106.248302.

[138] X. Zhou, Z. Liu, and B.-X. Xu. “Influence of dislocations on domain walls in perovskite ferroelectrics: Phase-field simulation and driving force calculation”. In: *International Journal of Solids and Structures* 238 (2022), p. 111391. DOI: https://doi.org/10.1016/j.ijsolstr.2021.111391.

[139] X. Zhou, C. Reimuth, P. Stein, and B.-X. Xu. “Driving forces on dislocations: finite element analysis in the context of the non-singular dislocation theory”. In: *Archive of Applied Mechanics* 91 (2021), pp. 4499–4516. DOI: 10.1007/s00419-021-02017-w.

[140] X. Zhou, C. Reimuth, and B.-X. Xu. “Phase-field simulation of misfit dislocations in two-phase electrode particles: Driving force calculation and stability analysis”. In: *International Journal of Solids and Structures* 249 (Aug. 2022). DOI: 10.1016/j.ijsolstr.2022.111688.

[141] J. Zhu et al. “Dislocation effect on diffusion-induced stress for lithiation in hollow spherical electrode”. In: *Journal of Solid State Electrochemistry* 20.1 (2016), pp. 37–46.

[142] Y. Zhu et al. “In situ atomic-scale imaging of phase boundary migration in FePO4 microparticles during electrochemical lithiation”. In: *Advanced materials* 25.38 (2013), pp. 5461–5466.

[143] Y. Zuo et al. “Domain wall stability in ferroelectrics with space charges”. In: *Journal of Applied Physics* 115.8 (2014), p. 084110.

List of Publications

Contributing Publications

[1] Christoph Reimuth, Binbin Lin, Yangyiwei Yang, Peter Stein, Xiandong Zhou, and Bai-Xiang Xu , "Chemo-mechanical study of dislocation mediated ion diffusion in lithium-ion battery materials", In: Journal of Applied Physics 130, 035103 (2021), https://doi.org/10.1063/5.0049502.

[2] Xiandong Zhou, Christoph Reimuth, and Bai-Xiang Xu, "Phase-field simulation of misfit dislocations in two-phase electrode particles: Driving force calculation and stability analysis", In: International Journal of Solids and Structures 249 (2022), doi: 10.1016/j.ijsolstr.2022.111688.

[3] Xiandong Zhou, Christoph Reimuth, Peter Stein, and Bai-Xiang Xu. "Driving forces on dislocations: finite element analysis in the context of the non-singular dislocation theory", In: Arch Appl Mech 91, 4499–4516 (2021), https://doi.org/10.1007/s00419-021-02017-w.

Contributions to conferences

[4] Christoph Reimuth, Peter Stein, Bai-Xiang Xu, "Multi-scale-modeling of dislocations in lithium-ion-battery-electrodes", poster presentation, WE Hereaus Seminar (2018).

[5] Christoph Reimuth, Peter Stein, Bai-Xiang Xu, "Analysis of stress-enhanced diffusion in the vicinity of dislocations", oral presentation, Materials Science and Engineering Congress (MSE) (2020).